

POLITECNICO DI MILANO

Facoltà di Ingegneria Industriale

Corso di Laurea Magistrale in

Ingegneria Energetica



**Thermodynamic optimization and annual performance characterization of
concentrated solar power plants employing advanced supercritical CO₂
Brayton cycle configurations.**

Relatore: Prof. Giampaolo Manzolini

Co-relatore: Ing. Marco Binotti

Tesi di Laurea di:

Luca Moretti

Matr. 784237

Anno Accademico 2013 - 2014

Aknowledgments

The international reader will excuse me if I turn to my native language for what I consider the most important part of my work.

Prima di chiunque altro, vorrei ringraziare dal profondo del cuore le persone a cui questo lavoro è dedicato: Ugo e Odilla. Due genitori eccezionali, il cui costante ed incondizionato supporto ha contribuito in maniera determinante al raggiungimento di questo traguardo, e non solo.

Un sentito ringraziamento va al prof. Manzolini, all'Ing. Binotti e all'Ing. Astolfi, per avermi guidato con pazienza e disponibilità attraverso la selva oscura chiamata tesi. Muchisimas gracias también a prof. Muñoz y Ing. Coco, para el apoyo durante el período de estancia en Madrid.

Il premio simpatia va ai colleghi, nonché amici, Pinkerton, Alessia, Ruben, Cpt. MisterMasterEaster (MME) e Andrea: grazie per tutte le risate condivise durante le lezioni più noiose, senza le quali l'Università avrebbe avuto un altro sapore.

Grazie inoltre agli amici storici: Angela, Stecchi, Pizzu, Daniele, Warrins, il cugino Tommaso, Bruno, Costanza, Ilario, Silvia, e tutti gli altri. Avendo condiviso con voi gran parte della mia vita, sono contento di poter fare altrettanto con questa tappa.

Infine, un grazie ed un abbraccio a tutte le persone conosciute durante periodi all'estero: ai Fagians of Madrid, al Capitano per la storia degli Yen coreani, ai mitici coinquilini Peter, James e soprattutto Hiroki, alla saggezza di Letizia, a Sylvia, agli spaniards Javi e Josè, a Huskywatch, al tizio che mi ha regalato il suo bastone durante la discesa da O'Cebreiro, e a tutti gli altri.

Se è vero che sono le esperienze vissute a fare di un uomo quello che è, sono le persone con cui le esperienze si vivono a determinarne la qualità. E questi anni sono stati grandiosi.

Summary

Aknowledgments	3
Summary	4
Index of figures	7
Index of tables	11
Sommario	12
Abstract	14
1 INTRODUCTION.....	16
1.1 BACKGROUND	16
1.2 SOLAR ENERGY	18
1.3 CSP ROLE IN ELECTRIC ENERGY PRODUCTION	19
1.4 WORK OUTLINE	23
2 CSP TECHNOLOGY	25
2.1 COLLECTORS.....	25
2.2 HEAT TRANSFER FLUIDS.....	29
2.3 BRAYTON CYCLE APPLICATION IN POWER BLOCK.....	31
2.4 REFERENCE PLANT	32
3 METHODOLOGY	35
3.1 SOLAR FIELD SIMULATION IN EES.....	35
3.1.1 COLLECTORS	35
3.1.1.1 COLLECTOR DESCRIPTION	36
3.1.1.2 HEAT TRANSFER MODEL DESCRIPTION.....	38
3.1.1.3 EES FUNCTIONS DESCRIPTION	44
3.1.1.4 PARAMETRIC ANALYSIS	54
3.1.2 SOLAR FIELD LAYOUT	59
3.1.3 PIPING DIMENSIONING AND HEAT LOSS / PRESSURE DROP CALCULATION	61
3.2 POWER BLOCK SIMULATION IN THERMOFLEX.....	67
3.3 CONNECTION BETWEEN THERMOFLEX AND EES	70

4	THERMODYNAMIC ANALYSIS OF CYCLE CONFIGURATIONS	73
4.1	SIMPLE REGENERATIVE CYCLE.....	74
4.2	REGENERATIVE RECOMPRESSION CYCLE.....	77
4.3	REGENERATIVE DOUBLE EXPANSION CYCLE	82
4.4	REGENERATIVE RECOMPRESSION DOUBLE EXPANSION CYCLE	86
4.5	REGENERATIVE INTERREFRIGERATED CYCLE	89
4.6	INTERREFRIGERATED DOUBLE EXPANSION	92
4.7	INTERREFRIGERATED RECOMPRESSION	93
4.8	INTERREFRIGERATED DOUBLE EXPANSION RECOMPRESSION	94
4.9	UA VALUE EFFECT ON SIMPLE AND INTERREFRIGERATED CYCLES.....	96
4.10	CONCLUSIONS	98
5	OFF DESIGN STUDY.....	100
5.1	SOLAR FIELD	101
5.2	TURBINE	104
5.2.1	TURBINE DESIGN.....	104
5.2.2	TURBINE OFF DESIGN.....	107
5.2.2.1	CRAIG&COX LOSS MODEL.....	107
5.2.2.2	OFF DESIGN CODE COMPUTATIONAL LOGIC.....	110
5.3	COMPRESSOR	116
5.4	HEAT EXCHANGERS.....	120
5.5	POWER BLOCK SECTION.....	123
6	ANNUAL RESULTS DISCUSSION	126
6.1	PERFORMANCE INDEXES.....	126
6.2	SIMPLE CYCLE VS INTERCOOLED CYCLE	128
6.3	INTERCOOLED CYCLES AT HIGHER T_{MAX}	135
7	CONCLUSIONS.....	140
8	REFERENCES.....	144

Index of figures

Fig. 1-1 : evolution of average temperature profile of Earth during the last century, and CO ₂ concentration increase in our atmosphere in the last sixty years. [1]	17
Fig. 1-2 : worldwide CO ₂ emission sources relative importance [2]	18
Fig. 1-3 : geographical distribution of annual irradiation reaching ground in the form of direct radiation [7]	20
Fig. 1-4 : international super-grid imagined by DESERTEC Initiative [5]	21
Fig. 1-5 : comparison of final electricity cost between different solar technologies [9]22	
Fig. 2-1 : overview of the four main configurations for CSP technology [12]	26
Fig. 2-2 : linear Fresnel collector [40].....	27
Fig. 2-3 : parabolic dish collector [41]	28
Fig. 2-4 : reference plant scheme (Thermoflex flowchart) [45].....	33
Fig. 3-1: parabolic trough collector [24].....	36
Fig. 3-2: receiver scheme. The absorber tube is protected by a glass envelope [23]....	37
Fig. 3-3: energy balance on the receiver cross section and equivalent thermal resistances scheme[23].....	38
Fig. 3-4 : solar field schematic	43
Fig. 3-5 : temperature profiles along collector length (T _{in} = 250°C, T _{out} =550°C)	54
Fig. 3-6: relative error between results obtained from the EES code written for the current work and from the code written by Alessia Robbiati [29]	55
Fig. 3-7: collector thermal efficiency and heat losses as a function of HTF bulk temperature (EDNI=850 W/m ² , m _{HTF} =0,78 kg/s)	56
Fig. 3-8: global efficiency of the collector as a function of its inlet temperature, for different DNI values (T _{out} =600°C).....	56
Fig. 3-9: thermal efficiency profile as a function of HTF bulk temperature at different wind speeds.....	57
Fig. 3-10: pressure drop in SF and total number of rows as a function the number of ET100 connected in series in each row	58
Fig. 3-11 : two and three pipes layout.....	59
Fig. 3-12: solar field layout. The HTF is conveyed by the third pipe in the cold headers, distributed in the rows constituting the 8 symmetric sections of the SF, and collected back in the hot headers.....	60
Fig. 3-13: cold header T junction	62
Fig. 3-14: unbalance at the intersections between outlet pressure from rows and pressure of the main stream in the hot header	63

Fig. 3-15: pressure profiles at the intersections between outlet pressure from rows and pressure of the main stream in the hot header after diameter adaptation	64
Fig. 3-16 : cross section of insulated pipe	65
Fig. 3-17 : example of Thermoflex flow chart, showing all the components employed in the power block simulation.....	68
Fig. 3-18: design simulation flow chart	71
Fig. 4-1 : simple cycle T-s diagram and PB scheme.....	74
Fig. 4-2 : cycle efficiency as a function of p_{min} and β (T_{max} and p_{max} fixed)	75
Fig. 4-3 : recompression cycle T-s diagram and PB scheme	77
Fig. 4-4: recompression cycle efficiency as function of split factor for different minimum pressures ($T_{max}=550C$ $p_{max}=100bar$).....	78
Fig. 4-5: regenerator T-Q diagrams ($p_{min}=30bars$ case above, $p_{min}=70 bars$ case below)	80
Fig. 4-6 : LTR exergy efficiency as a function of split factor ($p_{max}=110bar$; $p_{min}=40bar$; $T_{max}=550^{\circ}C$).....	81
Fig. 4-7 : double expansion regenerative cycle T-s diagram and PB scheme.....	82
Fig. 4-8 : double expansion cycle efficiency as a function of p_{min} for different combinations of p_{max} and T_{max} (intermediate pressure=100bar).....	83
Fig. 4-9 : exergy analysis comparison between double expansion cycles at different p_{min}	84
Fig. 4-10 : regenerator T-Q diagrams ($p_{min}=30bar$ case on the left, $p_{min}=70bar$ case on the right).....	85
Fig. 4-11 : recompression double expansion regenerative cycle T-s diagram and PB scheme	86
Fig. 4-12 : recompression double expansion cycle efficiency as function of split factor, for different minimum pressures ($p_{max}=150bar$; $T_{max}=550C$).....	86
Fig. 4-13 : envelope of split factor 0 points from curves in Fig. 4-12 : recompression double expansion cycle efficiency as function of split factor, for different minimum pressures ($p_{max}=150bar$; $T_{max}=550C$)	88
Fig. 4-14 : LTR (above) and HTR (below) T-Q diagrams ($p_{min}=70bar$; $p_{int}=110bar$; $p_{max}=140bar$; $T_{max}=550C$)	89
Fig. 4-15 : regenerative interrefrigerated cycle T-s diagram.....	90
Fig. 4-16 : interrefrigerated vs. simple cycle performance comparison	91
Fig. 4-17 : regenerator T-Q diagram comparison (simple cycle on the right, intercooled cycle on the left)	91
Fig. 4-18 : exergy analysis comparison between simple and intercooled cycles	92
Fig. 4-19 : effect of Intercooling addition to double expansion cycle ($T_{max}=550C$; $p_{max}=135bar$)	93

Fig. 4-20 : regenerative interrefrigerated recompressed cycle scheme and T-s diagram	93
Fig. 4-21 : cycle efficiency as a function of split factor for different p _{min} values	94
Fig. 4-22 : interrefrigerated double expansion cycle with recompression BOP scheme and T-s diagram	95
Fig. 4-23 : cycle efficiency as a function of split factor for different p _{min} values (p _{max} = 140bar ; T _{max} = 550°C)	95
Fig. 4-24 : simple cycle efficiency as a function of regenerator UA (p _{max} =100bar; T _{max} =550°C; p _{min} =30bar).....	97
Fig. 4-25 : intercooled cycle efficiency as a function of regenerator UA (p _{max} =100bar; T _{max} =550°C; p _{min} =30bar).....	97
Fig. 4-26: efficiency difference between intercooled and simple cycles as a function of regenerator UA	98
Fig. 4-27: comparison between maximum efficiencies at T _{max} =500°C and p _{max} =100bar with different cycle configurations	99
Fig. 5-1 : coordinate system to which the position of the sun is referred [43]	102
Fig. 5-2 : end losses in parabolic trough collector [12]	103
Fig. 5-3: global efficiency of single stage turbine as a function of its rotation speed (T _{in} =550°C, p _{in} =94,47 bar, p _{out} =40 bar, nominal mass flow=680,2 kg/s)	105
Fig. 5-4 : example of AXTUR output table	106
Fig. 5-5: meridian section of single stage turbine.....	106
Fig. 5-6 : loss sources in axial turbine [33]	107
Fig. 5-7 : off design code flow chart.....	111
Fig. 5-8 : efficiency and expansion ratio as a function of mass flow (T _{in} = 550 °C, p _{in} = 100 bar, m _{nom} =600kg/s).....	113
Fig. 5-9: dimensional curves for turbine at different inlet pressures (T _{in} =550 °C)	114
Fig. 5-10 : dimensionless form of curves from Fig. 5-9. The corrected mass flow is standardized on the nominal value	115
Fig. 5-11 : Baljè chart for compressors, and example of specific speed vs specific diameter matching. Blue and red lines represent the dimensioning of the simple cycle compressor at two different rotation speed (respectively 10000 rpm and 30000 rpm) [35]	116
Fig. 5-12 : predicted compressor performance map and measured functioning points (Sandia) [36]	118
Fig. 5-13 : dimensionless performance curve of compressor versus experimental points from Sandia facility [39]	119
Fig. 5-14 : dimensional performance curves for simple cycle compressor (T _{in} = 47 °C, p _{in} = 40 bar)	120

Fig. 5-15 : PB off-design Excel solution sheet and corresponding cycle T-s.....	124
Fig. 6-1 : off design performance of simple and intercooled cycles as a function of effective DNI.....	128
Fig. 6-2 : turbine inlet temperature and cycle pressure ratio as a function of EDNI in the case of simple cycle	129
Fig. 6-3 : global efficiency of simple cycle turbine and compressor as a function of EDNI	130
Fig. 6-4 : efficiency of intercooled cycle turbine and compressors as a function of EDNI	130
Fig. 6-5 : gross and net electric efficiency of simple and interrefrigerated cycles as a function of EDNI	131
Fig. 6-6 : monthly energy production for simple and intercooled cycles.....	132
Fig. 6-7 : energy production percent difference between simple and intercooled cycles	132
Fig. 6-8 : irradiance and power output profiles for a winter (above) and summer (below) characteristic day	133
Fig. 6-9: off design performance intercooled cycles at different T_{max} as a function of effective DNI.....	136
Fig. 6-10 : solar-to-electric efficiency of intercooled cycles at different T_{max} in winter (above) and summer (below) characteristic days	137
Fig. 6-11 : montly solar-to-electric efficiency of intercooled cycles at different T_{max}	138

Index of tables

Table 2-1: design performance of reference plant	34
Table 2-2 : annual performance of reference plant.....	34
Table 3-1: geometrical parameters of ET100 [24]	36
Table 3-2 : interface subscripts.....	39
Table 3-3 : heat flux terms in cross sectional energy balance [23].....	40
Table 3-4 : gas constants	47
Table 3-5 : Zhukauskas' coefficients	50
Table 3-6 : values of the optical parameters implemented in EES code.....	52
Table 3-7 : maximum admissible stress as a function of temperature for stainless steel P265GH.....	65
Table 5-1 : performance comparison between single and two stages turbine ($T_{in}=550^{\circ}\text{C}$, $p_{in}=94,93$ bar, $p_{out}=40$ bar, nominal mass flow=680,2 kg/s, rotation speed=10000 rpm).....	104
Table 5-2 : m coefficient value as a function of Re for Hilpert's correlation.....	121
Table 6-1 : annual simulation results for intercooled and simple cycles	133
Table 6-2: annual performance of intercooled cycles at different T_{max}	138

Sommario

Il solare a concentrazione (CSP) ricopre nel settore della produzione di energia elettrica da fonte rinnovabile un ruolo privilegiato, in virtù della sua facile integrazione con sistemi di accumulo termico. L'elevato costo finale dell'energia prodotta con questa tecnologia costituisce però un limite alla sua implementazione.

Il lavoro svolto si ripropone di investigare l'applicazione di cicli Brayton supercritici a CO₂ nella fase di conversione dell'energia termica in elettrica in impianti CSP diretti, con campo lineare. L'adozione di cicli a gas nella sezione di potenza al posto di quelli convenzionalmente usati basati su cicli a vapore Rankine, garantirebbe significativi vantaggi in termini di riduzione delle dimensioni e del costo delle turbomacchine, e di velocità di risposta nei transitori.

Gli strumenti sviluppati per simulare il funzionamento degli impianti sono molteplici. L'analisi effettuata copre sia la fase di design degli impianti, che il confronto tra le prestazioni annuali delle migliori configurazioni studiate. L'approccio di studio seguito non è mai stato adottato in letteratura, in particolar modo per quanto riguarda l'utilizzo innovativo degli strumenti di simulazione. Il campo solare è stato programmato, sia in fase di design che in off design, ricorrendo ad Engineering Equation Solver (EES). Il codice elaborato parte dal lavoro effettuato dall'NREL nella simulazione di collettori singoli, per arrivare alla simulazione di un campo solare completo, incluso il sistema di tubazioni. Per quanto riguarda la sezione di potenza, si è ricorso al software Thermoflex in fase di design, mentre il suo off design è stato programmato in Visual Basic. L'interazione tra le diverse simulazioni è stata garantita nella forma di uno scambio dinamico di informazioni (Dynamic Data Exchange, DDE), anch'esso programmato in Visual Basic: il codice scritto, facendo uso di comandi appositi, permette di mettere in comunicazione dinamica i diversi programmi utilizzati, capacità che di base non avrebbero.

L'analisi svolta è articolata in due fasi. Durante la prima fase si sono esplorate le performances di numerose configurazioni di ciclo Brayton, andando a studiare l'effetto di ricompressione, doppia espansione, interrefrigerazione, e

loro combinazioni sulla termodinamica del ciclo. Ogni configurazione è stata ottimizzata in termini di rendimento elettrico, identificando i valori dei parametri operativi principali che, rispettando i vincoli imposti dalla necessità di garantire la resistenza meccanica dei collettori, ottimizzassero l'efficienza elettrica del ciclo. I risultati ottenuti per le varie configurazioni sono poi stati confrontati, per determinare quelle più promettenti: il ciclo semplice rigenerativo e il ciclo interrefrigerato rigenerativo hanno dimostrato di garantire il miglior compromesso tra prestazioni e configurazione impiantistica ad un basso livello di complessità.

Nella seconda fase, le due soluzioni ottimali sono state caratterizzate in dettaglio, dimensionandone i vari componenti (turbina, compressore, rigeneratore). Il loro funzionamento in off design è stato inoltre calcolato, consentendo di determinare la risposta dell'impianto nel suo complesso alla variazione delle condizioni ambientali, come la radiazione solare. In particolare, per le turbine si è sviluppato un codice dedicato, capace di predire la performance di off design di una turbina partendo dalla sua geometria. Sulla base dei risultati ottenuti, si è infine proceduto a calcolare la performance annuale degli impianti.

Le prestazioni nominali dei due impianti di cui il design è stato caratterizzato in dettaglio (caso ottimo per ciclo semplice e ciclo interrefrigerato), indicano un'efficienza elettrica nominale del power block rispettivamente di 28.1% e 31%, a fronte di una prestazione termica nel campo solare penalizzante rispetto ai tradizionali cicli indiretti, per via delle più alte temperature medie dell'HTF.

Le simulazioni annuali hanno indicato come il ciclo interrefrigerato rigenerativo garantisca un'efficienza di conversione solar-to-electric superiore al ciclo semplice, arrivando al 14.21% contro il 12.52%. L'effetto di un incremento nella temperatura massima del ciclo interrefrigerato è infine stato analizzato, concludendo che senza un intervento sul campo solare per limitare le perdite termiche dovute alle alte temperature, questo intervento peggiora la performance dell'impianto.

Abstract

Concentrated Solar Power (CSP) covers a promising role in the sector of energy production from renewable sources, since it can easily be integrated with thermal storage systems. The high final cost of the energy produced though constitutes a limit to the implementation of this technology.

The current work studies the application of supercritical CO₂ Brayton cycles during the energy conversion process in the power section of linear collector CSP plants. The adoption of gas cycles instead of the traditional steam cycles, would guarantee great advantages in terms of reduction in size and cost of the turbomachines, as well as fastness in response to transient conditions.

The instruments developed in order to simulate the functioning of the plants are more than one. The analysis covers both the design of the plants, and the assessment of the annual performance of the best configurations studied. The methodology followed has never been adopted in literature, and the use done of the simulation softwares is particularly innovative. The solar field was programmed, both for its design and off-design, in Engineering Equation Solver (EES). The code written is based on the work done by NREL on the simulation of single collectors, and simulates a complete solar field, including the piping system. As for the power section, the software Thermoflex was used during the plant design, whereas its off design was programmed in Visual Basic. The interaction between the various simulations was attained in the form of a Dynamic Data Exchange (DDE), programmed as well in Visual Basic: the code written, by means of specific commands, opens a dynamic communication channel between the softwares, which are then free to exchange results.

The analysis carried out is divided in two steps. In the first step the performances of a large number of Brayton cycle configurations was explored, investigating the effect of recompression, double expansion, intercooling, and their combinations on the thermodynamic of the cycle. Each configuration was then optimized in terms of electric efficiency, identifying the values of operative parameters that, within the boundaries imposed by the collectors mechanical resistance, maximize the electric efficiency of the cycles. The results obtained for the various configurations were then compared, in order to

assess which grants the best performances: simple cycle and intercooled cycle proved to attain the best combination of good performance and simpler cycle configuration.

The following step was characterizing the two optimal solutions in detail, proceeding with a sizing of each one of the components (turbine, compressor, regenerator). Their off-design functioning was characterized as well, and the behavior of the plant off-design as a function of different irradiance conditions was assessed. In particular, a code was developed in order to predict the off-design performance of the turbines, based on their geometry. Starting from these results, the annual performance of the plants was finally determined.

The nominal performance of the two plants which design was characterized in detail (optimal case of simple cycle and intercooled cycle), indicate a nominal electric efficiency of the power block respectively of 28.1% and 31%, and a thermal performance of the solar field which penalizes the two plants with respect to the traditional indirect cycles, because of the higher average temperature of the HTF in the solar field.

Annual simulations indicate how intercooled regenerative cycle attains a higher solar to electric efficiency with respect to the simple regenerative cycle, reaching 14.21% versus 12.52% of the latter. The effect of an increment in the maximum temperature of the cycle was finally assessed, concluding that without an intervention on the solar field in order to limit heat losses due to the high average temperatures, the raise in T_{\max} lowers the overall performance of the plant.

1 INTRODUCTION

1.1 BACKGROUND

The interest in alternative and clean energy production systems is growing more and more as consequence of the increasing concern on the environmental safeguard. Engineers are nowadays asked to develop alternative solutions to the usage of fossil fuels, in order to contain greenhouse gas emissions, and in particular of CO₂, which are the considered the main cause for global warming. A further increase in the temperature of our planet might have a disastrous and largely unpredictable effect on the environment, and since the vast majority of the international scientific community agrees on the direct connection between the rise of CO₂ concentration in our atmosphere and the increase in Earth's surface temperature, immediate actions should be taken in order to prevent or at least slow down the phenomena.

Greenhouse effect is a process through which part of the infrared radiation emitted by Earth is trapped by the atmosphere and reflected back on Earth. Solar radiation hits Earth constantly, and the portion of it in the wavelength range of visible light bypasses the atmosphere and warms Earth surface. In turn, this causes our planet, which behaves like a black body, to re-emit part of this energy in the form of low frequency radiation, due to its low surface temperature. Greenhouse gases are characterized by an absorption spectrum that covers infrared frequencies: instead of being transmitted back to space, the re-radiation is absorbed by these gases present in the atmosphere, and eventually re-emitted once again in all directions, and thus partly back to Earth. The increase in the amount of solar radiation held back within the atmosphere leads in turn to a raise in the average temperature of our environment.

The Intergovernmental Panel on Climate Change (IPCC) published last year a document [1] collecting evidences from a wide range of scientific fields, meant to banish all doubts about the reality of climate change, and its anthropogenic cause. The average surface temperature of earth has been consistently increasing in the last 150 years, as shown in Fig. 1-1, and the sudden ramp we have been observing since right after World War II matches the contextual hike

of CO₂ concentration in our atmosphere, consequence of the rapidly increasing industrial activity that followed the conflict [1].

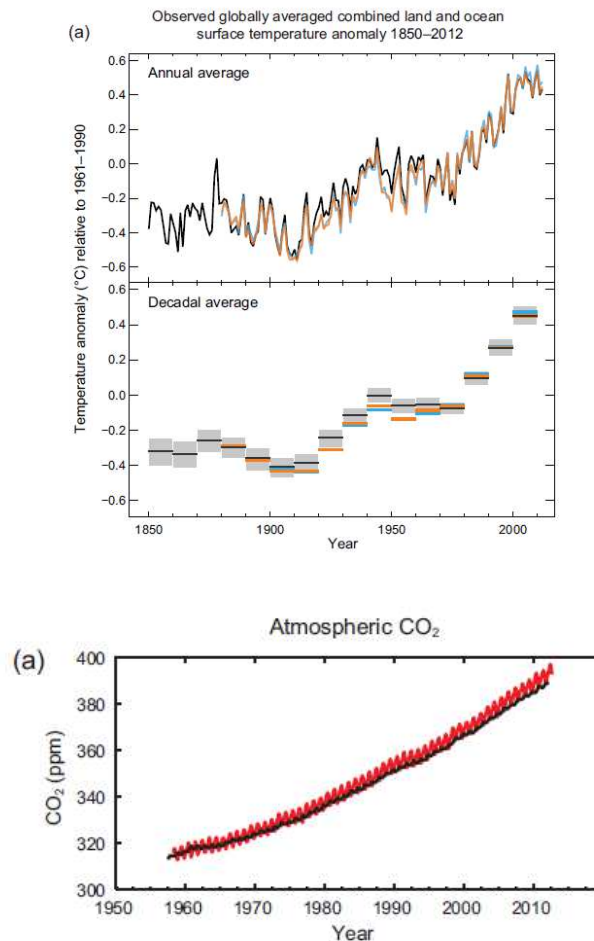


Fig. 1-1 : evolution of average temperature profile of Earth during the last century, and CO₂ concentration increase in our atmosphere in the last sixty years. [1]

In

Fig. 1-2, the relative importance of CO₂ global emission sources is summarized, as listed by the US Environmental Protection Agency (EPA) [2]. It can be seen how the energy production sector represents the main cause of CO₂ emission, due to the intensive usage of fossil fuels in thermal electric power plants. In order to rapidly and effectively cut down CO₂ emissions, alternative ways to produce electric energy must be identified and pursued.

Renewable energies could represent, along with nuclear power, a way to reduce the dependency on fossil fuels. If humankind was to develop an efficient and cost-competitive way to utilize the incredible amount of energy available in nature, we might not only reduce the environmental threat discussed above, but also put the basis for a sustainable system of energy production, which in a future perspective might come to be independent from the availability of exhaustible primary sources.

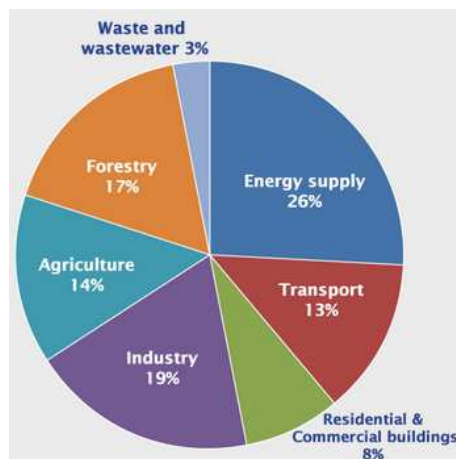


Fig. 1-2 : worldwide CO₂ emission sources relative importance [2]

1.2 SOLAR ENERGY

Among the other renewable energies, solar energy presents the advantage of exploiting a natural resource, sunlight, which is available everywhere in the world. The total amount of energy delivered to our planet in the form of sun radiation is massive: harnessing the energy reaching less than the 0.5% of Earth deserts' surface would be enough to meet the energy demand of the entire world [5] estimated to be in 2012 slightly below 13.000 Mtoe [50]. Typical values for the irradiance power reaching the surface of our planet is of about 1 kW/m² [4], but this value is strongly affected by the latitude of the considered location, being much larger in the areas surrounding the tropics.

The interaction of solar radiation with the molecules composing the atmosphere affects the propagation of photons: a portion of the radiation is

scattered and takes the name of *diffused radiation*, as opposed to the part that maintains its original direction and constitutes the *direct radiation*. The ratio between the two is strongly dependent on weather conditions: during a cloudy day for example, basically the whole amount of incoming radiation is diffused.

Conversion of solar energy to electric energy can be achieved in two ways:

- Through the photoelectric effect, the emission of electrons induced in a material by its exposition to a source of radiation (photovoltaic panels, or PV)
- Using the solar radiation as a thermal input, heating up a fluid and converting, through a thermodynamic cycle, the thermal energy in mechanical energy (concentrated solar power, or CSP)

Photovoltaic panels take advantage indistinctly of both direct and indirect radiation, since the physical effect on which their functioning is based just requires photons to reach the surface of the semi-conductor constituting the panel, without any preferential direction.

As for CSP, the solar radiation needs to be focused using mirrors, in order to concentrate a sufficient amount of energy on the receiver. The focusing process is necessary to attain elevated heat fluxes on limited surfaces. This is important not only to contain the total surfaces and thus costs, but also to limit the relative importance of heat losses with respect to the thermal input, and to reach in turn higher temperatures. In order to be focused though, the incoming solar radiation has to be oriented in the form of parallel rays: CSP can thus exploit only the direct portion of radiation.

1.3 CSP ROLE IN ELECTRIC ENERGY PRODUCTION

The great feature that makes CSP an extremely promising technology on the way to attain an improved utilization of renewables in the global energy production, is that, since radiation harnessing and energy conversion are two separate processes, it can be integrated easily and cost-effectively with a thermal storage system. The storage allows to level the energy production throughout the day, and potentially continue it also when the radiation input is

not available (during the night, or in cloudy days). Example of this extremely interesting potentiality is Gemasolar power plant, in Sevilla, Spain. The plant has a nominal electric capacity of 19.9 MW, and it manages to guarantee electrical production for a total of 6500 hours per year [6].

The capability of modulating the energy production is a feature of major importance not only in the view of a better annual performance for the technology, but also considering a possible synergy between CSP and other renewable technologies. One of the biggest issues related to a substantial increase in the electric energy production share covered by renewables is that the output coming, for example, from PV or wind turbines cannot be controlled, being dependent on the availability of an intrinsically unpredictable source. In order to guarantee the balance between instantaneous demand and supply, it would then be necessary to rely on expensive battery arrays, or count on traditional power plants to backup the production when needed. Because of its characteristics, CSP could be the production buffer that the set of renewable power plants needs to even out its global output. Two are the main disadvantages of CSP technology: suitable locations, and final cost of electricity.

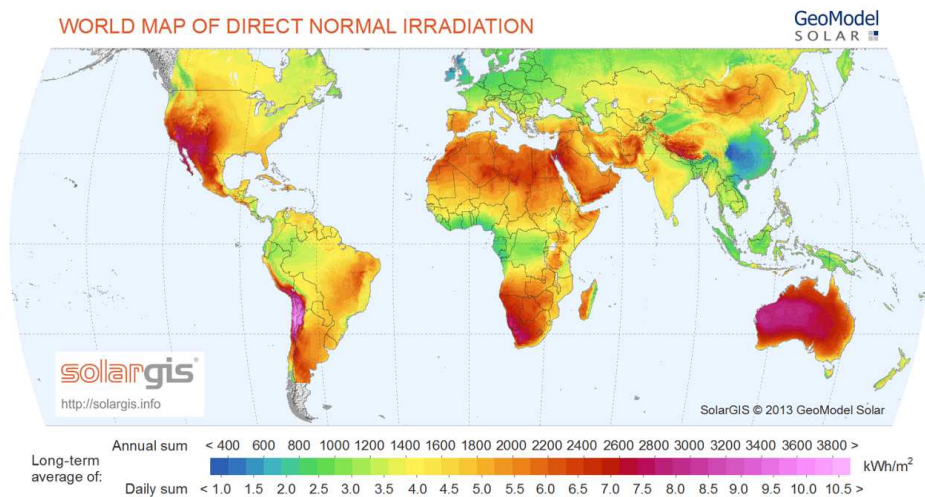


Fig. 1-3 : geographical distribution of annual irradiation reaching ground in the form of direct radiation [7]

As already mentioned, CSP plants can only exploit direct radiation to attain electric energy production. Referring to Fig. 1-3, it can be seen how the regions in which the annual amount of energy delivered to the ground in the form of

direct radiation is more abundant are concentrated at specific latitudes, that not necessarily correspond to where the final energy consumption actually takes place [7].

Nevertheless, both in the case of US and Europe it is possible to imagine a delocalization of the energy production. States like California, Nevada and Arizona could be the ideal sites where CSP technology could be implemented, and the energy produced could be transferred by means of electric lines to the rest of the country. Proof of the interest placed in this idea is the recent construction of Mojave Solar Project, a 280 MW gross parabolic trough plant located 100 miles north of Los Angeles. The plant is scheduled to start producing in 2014, and will prevent the emission of 350.000 tons of CO₂ per year [8].



Fig. 1-4 : international super-grid imagined by DESERTEC Initiative [5]

As for Europe, the whole group of north-african states as well as Spain and the south of Italy, are suitable to host the installation of CSP plants. DESERTEC Foundation is a global network connecting scientist, economists and companies, whose purpose is to promote a shift towards a sustainable energy production system [5]. One of the main potentialities they indicate as a feasible way to achieve this final objective, is the exploitation of the huge amount of solar energy radiating on Earth's deserts every day. In order to do so, they are

working on the implementation of an electric grid connecting north Africa and Europe, as well as promoting the creation of commercial partnerships between African states like Morocco and Tunisia, and the European Union. The idea is to create a macro-grid that manages to exploit renewable natural resources where they are most available, and that is able to transport the produced energy to all countries participating in the network (Fig. 1-4).

The second big issue that CSP has to confront with is its cost. Nowadays, the final LCOE (Levelized Cost Of Electricity) of the electric energy produced by CSP plants remains much higher than what seen in the case of other renewables. Fig. 1-5 shows a comparison between the current final cost of energy in the case of PV, concentrated PV and CSP. It can be seen how CSP has the highest LCOE, with a value that decreases with the size of the storage system, but remains superior to 14 c€/kWh [9].

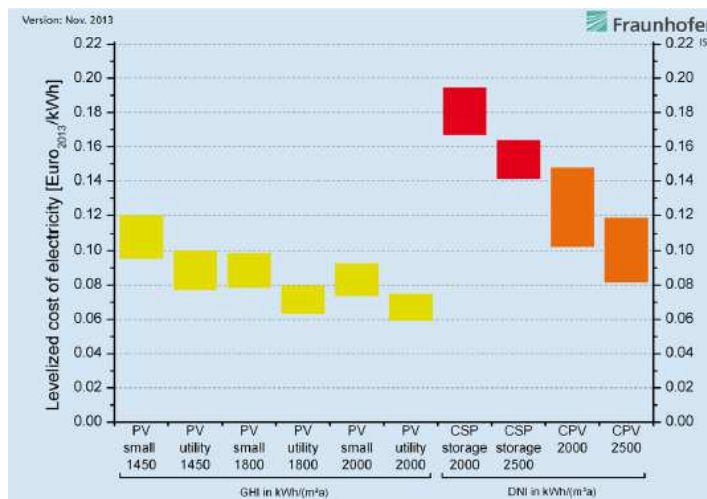


Fig. 1-5 : comparison of final electricity cost between different solar technologies [9]

Compared to PV though, CSP still presents an extremely large margin for improvement, and sensible cost reduction can be achieved for most of the components of a CSP plant. Furthermore, as already mentioned, the dispatchability offered by the integration with storage systems (which was not considered in the mentioned study) has to be taken into account during the economic analysis: the extravalue of this capability can be estimated to be between 5 and 12 c€/kWh [10], substantially decreasing the gap between the LCOE of the two technologies.

1.4 WORK OUTLINE

The objective of the current work is to investigate innovative configurations for CSP plants that can guarantee high conversion efficiencies reducing at the same time the cost of the power section. Specifically, advanced configuration of high efficiency supercritical CO₂ Brayton cycles are considered to attain the power conversion. Brayton cycles present substantial advantages compared to the Rankine cycles traditionally employed in CSP plants, both in terms of lower total cost of the plant components and in faster response to transient conditions.

The employment of supercritical CO₂ as working fluid both in the power block and solar field is studied, carrying out design and off design simulations of the two sections of the power plant, and assessing their coupled performance. The simulations are carried out using different softwares:

- a model for the solar field was developed in EES. The code calculates the performance of the solar field both in design and off-design conditions;
- power block design is simulated using Thermoflex, a commercial software capable of solving the balance of power of complex energy systems;
- power block off design simulation was programmed in Visual Basic on the results obtained during the off design study on the plant components, and carried out using Excel.

A way to integrate the heterogeneous computations had to be elaborated. The link between the simulations is attained in the form of a Dynamic Data Exchange: through a code programmed in Visual Basic, the different programs have been connected in order to be able to exchange results and iterate the calculations until convergence is reached. This methodology has never been followed before in literature.

A large number of potential configurations for the power section thermodynamic cycle is investigated, performing a thermodynamic optimization on the design performance of the power plant to identify the best

combination of operative parameters. The best choices in terms of electric efficiency are then studied in detail, proceeding with a design sizing of the components, as well as their off design characterization. In particular, to assess the off design performance of the turbines, a code predicting the off design of a dimensioned turbine was elaborated, on the basis of the work done in [32].

The results from the off design simulations were finally used to calculate the annual performance of the plants, obtaining their total energy yield and annual efficiency and identifying the best solution in terms of annual solar-to-electric efficiency.

2 CSP TECHNOLOGY

2.1 COLLECTORS

The fundamental principle at the basis of CSP is the focusing of the direct radiation on a receiver, in which the HTF flows. The thermal energy harvested will then be converted to electric energy in the power block, by means of a conventional thermodynamic cycle.

A classification of the different configurations of CSP can be based on the concentrator and the receiver types. Focusing systems can be divided into two groups:

- point focus systems (solar towers, solar dishes): the solar radiation is focused onto a specific point;

- linear focus (parabolic trough, Fresnel): the solar radiation is focused along a line.

Point focusers can generally allow for higher concentration ratio (CR). CR is defined as the ratio between the surface of the reflectors and the surface on which the radiation is focused:

$$CR = \frac{A_{mirrors}}{A_{collector}} \quad (2-1)$$

Higher concentration ratios will imply higher thermal fluxes entering the HTF, and thus more compact collectors, with reduced heat losses and capable of reaching higher temperatures. Linear receivers normally achieve CR from 30 to 80. In the case of solar towers the concentration ratio can be as high as 1000, and this value can be even higher for solar dishes [12].

A second distinction (alternative to the commonly used categorization in continuous and discrete systems based on how the reflecting parabola is shaped) can be done on the basis of receiver's mobility: systems in which the receiver moves together with the mirrors during the sun tracking are parabolic trough and dishes; the receiver is on the other hand fixed in linear Fresnel and central tower solar fields.

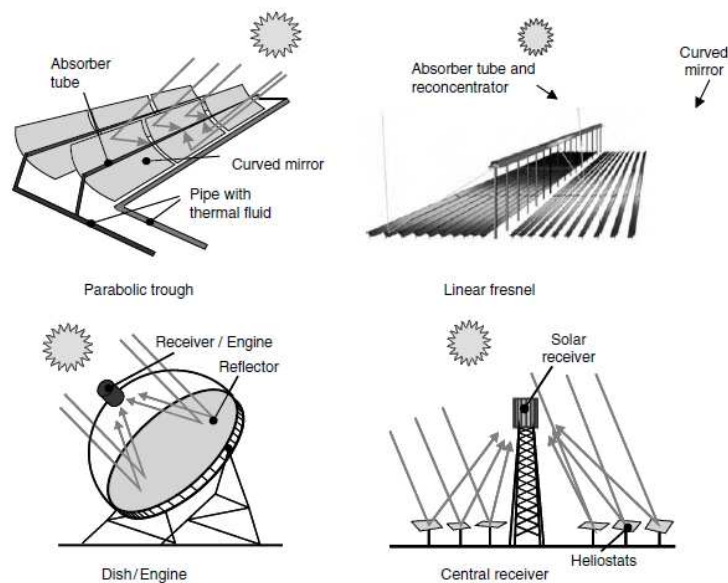


Fig. 2-1 : overview of the four main configurations for CSP technology [12]

Parabolic trough is nowadays the most mature technology, and it has been implemented in several power plants operating all over the world. SEGS complex, in California, US, is a large group of solar power plants, with a total electric power of 354 MW. The first plant was inaugurated in 1984, and over the years the complex has been expanded up to the current size [13]. All of its solar fields employ parabolic troughs. Long rows of parabolic mirrors focus the sun rays over a receiver tube, held in the focal position by brackets connected to the structure sustaining the mirrors. This structure ensures the movement of both mirrors and receiver throughout the day, tracing the position of the sun and maintaining the aperture plane normal to the incoming rays.

Linear Fresnel work in a similar way, but instead of having a single curved mirror the reflecting surface is constituted of multiple ground-based flat mirrors. The mirrors are free to rotate along their axis, and they can be positioned in order to approximate a parabolic surface. The receiver tube is supported by a fixed structure, and does not participate in the tracking process. The simpler structure of the collector with respect to the parabolic trough presents many advantages: first of all, it greatly reduces the cost associated with the manufacturing of the mirrors, as well as the amount of material required for their supports, making Fresnel collectors much cheaper;

furthermore, the energy consumption associated with the tracking is also reduced; finally, the fact that the mirrors are positioned on ground level allows for a more compact solar field layout, eliminating shadowing effects between adjacent loops. On the other hand though, the focusing achieved by this technology is less accurate than parabolic trough, because the curve surface of the reflector is approximated using flat mirrors. This in turn leads to lower collector global efficiencies. In order to increase the amount of radiation reaching the collector, a secondary mirror can be positioned above the collector itself, to intercept the rays that missed it and refocus them towards the receiver (Fig. 2-2).

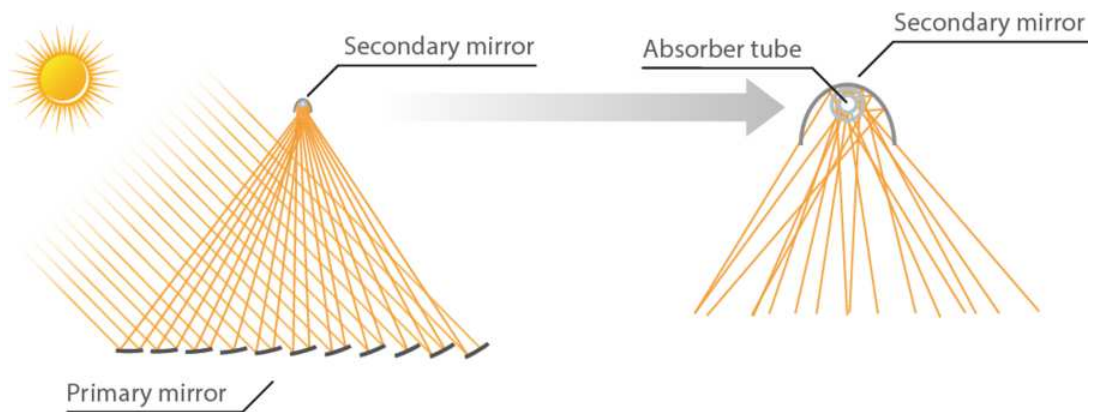


Fig. 2-2 : linear Fresnel collector [40]

A commercial application of linear Fresnel collector can be found in the power plant Puerto Errando 2 (PE2), constructed by Novatec Solar near Murcia, in Spain. The plant has an electric nominal capacity of 30 MW, and produces saturated steam at 270°C directly in the receiver tubes [14].

In power tower solar fields, the receiver is positioned on top of a high tower, placed in the center of the heliostat field. These are flat (or slightly curved) mirrors, which can track the position of the sun by moving with respect to two different axes. The concentration ratio of this technology is not limited by constraints in the size of the mirrors, as it normally is in linear collectors, and the maximum achievable temperatures are substantially higher, with positive impacts on the thermal to electric conversion efficiency. An additional example of plant that employs this technology, beyond the already mentioned

Gemasolar, is the recently opened Ivanpah Solar Power facility, in California. This large power plant reaches a nominal capacity of 392 MW, and deploys 173.500 heliostats for a total solar field surface of 3.500 acres [15].

The last typology of collector is the parabolic dish. These stand-alone collectors achieve a direct conversion of the incoming radiation in electric energy, employing a conversion unit (Stirling engine, microturbine) positioned directly in their focal point. As in the case of the heliostats, the dishes are free to move with respect to two axes in order to follow the sun position. This technology achieves the best solar-to-electric conversion efficiencies among CSP configurations: in 2008, Stirling Energy Systems set the new world record to be 31.25%. The efforts to proceed with a commercial deployment though have so far been unsuccessful, to the point that Stirling Energy System was forced to declare bankrupt in 2012, and their demonstrative power plant Maricopa Solar, with a nominal capacity of 1.5MW, has been dismantled.

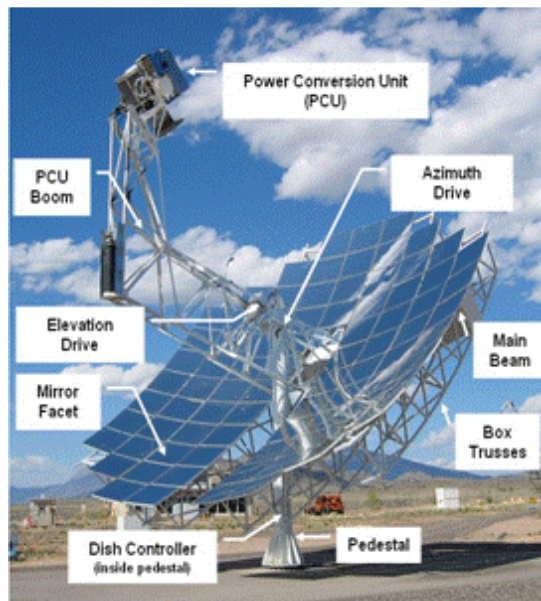


Fig. 2-3 : parabolic dish collector [41]

2.2 HEAT TRANSFER FLUIDS

The performance of a CSP plant is strictly connected with the selection of the fluid employed in the receivers in order to collect and transport the heat to the power section. The choice of the HTF has to be made on the basis of many different considerations:

- 1) thermodynamic properties;
- 2) effectiveness in the heat transfer process;
- 3) cost of the HTF;
- 4) environmental issues connected with its employment.

Furthermore, we have to discern between plants that directly employ the HTF in the power section as the working fluid, versus indirect cycles where an heat exchanger decouple the solar field and the power block working fluids.

The first fluids to be employed in CSP indirect plants have been synthetic oils. These fluids are normally selected as HTF in many applications for their high thermal capacity and good heat exchange properties, but present some issues that undermine their suitability for CSP. First of all, their inflammability and toxicity make them hazardous substances to work with, and pose serious safety issues in their implementation as HTF. Secondly, their cost is quite high, and in the perspective of integration with a thermal storage system the amount of fluid required would call for cheaper solutions. Finally, their thermal stability is guaranteed up to relatively low temperatures: the most resistant oils can withstand temperatures up to 400°C [16]. This limit affects the quality of the energy conversion which is proportional to its maximum temperature as described in Carnot theorem:

$$\eta_{max} = 1 - \frac{T_{amb}}{T_{max}} \quad (2-2)$$

In order to solve these issues, and to improve the performance of CSP by overtaking the temperature constraint, an innovative solution currently under study is the adoption of molten salts as HTF in the solar field. Eutectic mixtures of sodium and potassium nitrate are the most promising for the application, because of their low freezing point temperature (as low as 210°C). Molten salts can be heated up to 600°C before degradation occurs [17]. Furthermore, they

are neither flammable nor toxic, and their cost is lower compared to synthetic oils. Their usage in linear collectors though is complicated by the fact that the HTF has to be constantly maintained in the liquid form, and cannot reach temperatures below the freezing point. When the radiation is not available, a backup heating system has thus to provide the thermal input necessary to avoid solidification in the piping system. Furthermore, unlike oils, molten salts can corrode the piping metal: this not only poses a threat to the long term mechanical integrity of the system, but could also lead to a progressive change in the thermodynamic behavior of the HTF, because of the effect that the chemical compounds originally present in the steel and diluted in the molten mixture can produce. On the topic, the author conducted a research while working at the Center for Clean Energy Engineering (University of Connecticut, Storrs, CT, USA), leading to the publication of a poster proposing a model for the corrosion mechanism [18].

Direct cycles employ the same fluid both in the solar field and in the power block. The elimination of an intermediate heat exchanger reduces irreversibility generation, simplifies plant configuration, and the coincidence of the maximum temperature achievable by the solar field and the effective temperature can lead to thermodynamic advantages. Being that all CSP plants constructed so far employ steam as working fluid in the power section, the research has been focused on collectors working with pressurized water, capable of producing saturated or superheated steam to be sent to the turbine. This technology takes the name of Direct Steam Generation (DSG), and has already been deployed in demonstrative and commercial plants. An example is Kanchanaburi Solar Plant, built in Thailand by the German company Solarlite. The plant has a nominal electric capacity of 5MW, and employs parabolic trough collectors divided in two sections: 12 recirculating loops produce saturated steam evaporating the water coming from the condenser; the steam is then superheated in a second smaller section, where 7 additional loops heat it up to 330°C [19].

Working with a two-phase flow in the receiver pipes poses challenging issues in the control of the homogeneity of the heat exchange on the cross section, which may cause dangerous thermal gradients in the walls of the pipe due to flow stratification compromising its mechanical resistance. Furthermore, the

lower film coefficient associated with a gaseous flow will increase the difference between the bulk temperature of the HTF flow and the metal walls, increasing thermal losses and raising the requirements on the material for the pipes. The operation of a DSG field will then be more complicated, and maximum achievable temperatures will necessarily have to be lower compared with what seen for liquid HTFs.

Gaseous HTF have not been employed so far in CSP plants, because of their lower thermal capacity and heat exchange properties. As will be discussed though, the utilization of supercritical gases as both HTF and working fluid in direct CSP plants might be an interesting perspective, in the optic of an improvement of the conversion efficiency as well as a reduction in the power section cost.

2.3 BRAYTON CYCLE APPLICATION IN POWER BLOCK

An innovative alternative to the employment of Rankine cycles to achieve the power conversion might be represented by supercritical Brayton cycles. High efficiency Brayton cycles employing supercritical CO₂ as working fluid, have been investigated by many authors since the '60s [20-22]. The great advantage that the selection of this particular fluid ensures comes from the fact that exploiting the low critical temperature of CO₂ (32 °C), the heat rejection and compression processes can be performed in proximity to Andrew's saturation curve. The working fluid will then behave as a real gas, leading to two major positive effects:

- its density will largely increase at the compressor inlet; being that compression work is proportional to specific volume, the fact that the gas is behaving like a liquid fluid will greatly decrease the specific work needed to achieve the compression, and thus increase the work output of the cycle;
- its thermal capacity will increase as CO₂ is cooled down to temperatures close to ambient condition, flattening the temperature profile inside the rejection heat exchanger, therefore lowering the irreversibility generated by the process

The latter effect will also affect the heat exchange in the regenerators, causing an unbalance between the streams specific heat in the high and low pressure side. If the mass flow is the same on the two sides then, the two thermal capacities will greatly differ, increasing irreversibility generation in the component. In order to attain the maximum benefit from the mentioned effects then, and limit the performance loss due to regenerators unbalance, a series of cycle configurations have been proposed and studied by Angelino in his work [21], with particular attention to the comparison with the reference performance of corresponding traditional steam cycles.

In the case of CSP, the adoption of $s\text{CO}_2$ Brayton cycles in the power section could gain interesting advantages. First of all, the performance of these cycles is competitive with what attained by Rankine cycles in the range of low and moderate maximum temperatures (450-600°C), where traditional Brayton cycles would have to be ruled out. Secondly, switching to a gas cycle would have a great impact on the complexity, and thus the final cost, of the turbine: gas turbines require fewer stages, since the change in volumetric flow and the specific enthalpy difference across the machine are both largely inferior with respect to a steam turbine. Finally, gas cycles can respond much faster to transitory conditions, implying faster start up times when the plant is turned on in the morning, and faster adaptation to the off design functioning point determined by the fluctuating value of DNI throughout the day.

For these reasons, the annual performance of different direct $s\text{CO}_2$ Brayton cycles configuration coupled with a parabolic trough solar field is investigated in the current work. The analysis covers both plant design analysis, with a performance-wise optimization of operative parameters, and the consequent off-design characterization, leading to an annual energy yield.

2.4 REFERENCE PLANT

The technology selected for the solar field of the current work are parabolic trough collectors, being the most mature technology among linear collectors. In order to compare the results with a reference case representative of the technology state of the art, the work done in [45] was considered. The paper

investigates, among the other solutions, an indirect CSP plants employing parabolic troughs in the solar field, working with synthetic oil (Therminol VP-1) as HTF. The collectors implemented in the work reflect the components employed in the power plant Andasol II, in Spain. The maximum temperature reached by the oil in the solar field is 391°C. As for the power section, steam temperature at the turbine inlet is set to 371°C. The maximum temperature of the cycle is then limited, with respect to our case, both by the adoption of an indirect cycle and by the choice of the HTF, which is not stable above 400°C. The analysis is carried out simulating both solar field and power block in Thermoflex, which includes in its components library linear collector solar fields working with liquid (synthetic oils, molten salts) and two phases (water/steam) HTFs. The annual performance of the plants characterized within this work will be compared with the described reference, to assess advantages and disadvantages of the innovative configurations explored with respect to the traditional technological solutions currently employed in existing power plants.

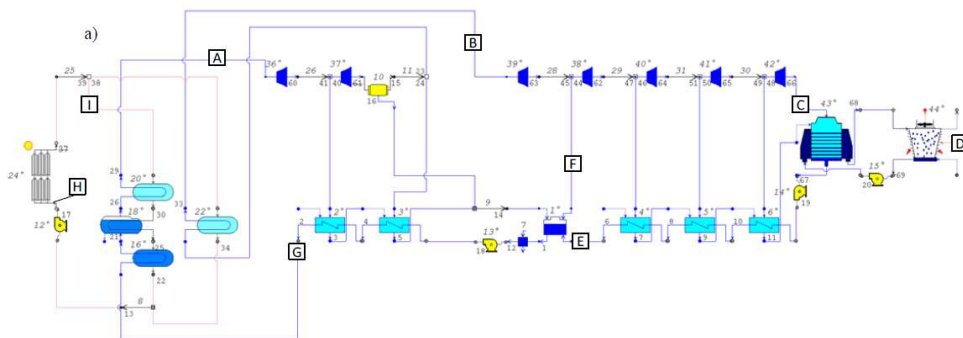


Fig. 2-4 : reference plant scheme (Thermoflex flowchart) [45]

Fig. 2-4 shows the plant schematic, whereas Table 2-1 sums up its design performance. The performance indexes used are explained in the following:

- η_{optical} is the optical efficiency, that compares the radiation on the absorber tube with the DNI;
- η_{thermal} considers the collector thermal losses;
- η_{piping} evaluates the impact of piping thermal losses;

- $\eta_{\text{net PB}}$ is the thermal to electric efficiency conversion of the power block;
- η_{aux} considers the consumption due to the auxiliaries that ensure the circulation of the HTF in the solar field;
- η_{overall} is the product of all the efficiencies listed.

Table 2-1: design performance of reference plant

Net Power Output [MW]	50
η_{optical} [%]	71.24
η_{thermal} [%]	95.22
η_{piping} [%]	99.17
$\eta_{\text{net PB}}$ [%]	36.74
η_{aux} [%]	95.23
η_{overall} [%]	23.53

The annual performance, expressed using the same performance indexes introduced for the plant design, is summed up in Table 2-2. These results will be the term of comparison for the annual performance of the direct plants developed in the current work.

Table 2-2 : annual performance of reference plant

η_{optical} [%]	52.75
η_{thermal} [%]	92.73
η_{piping} [%]	98.64
$\eta_{\text{net PB}}$ [%]	34.45
η_{aux} [%]	96.57
η_{overall} [%]	16.05

3 METHODOLOGY

In order to simulate the operation of the whole solar plant, two software were used: Thermoflex for the power block, and Engineering Equation Solver (EES) for the solar field. The two independent simulations were then linked through Excel, programming in Visual Basic via an interprocess communication method called Dynamic Data Exchange (DDE). This was necessary because, although the components library of Thermoflex is very large, a model for a solar field working with supercritical CO₂ is not currently available. In the next paragraphs a detailed description of the two simulation models as well as of the structure of the interaction between the software is provided.

3.1 SOLAR FIELD SIMULATION IN EES

3.1.1 COLLECTORS

The heat transfer model written in EES to simulate the solar field collectors is a modification of the one developed at the National Renewable Energies Laboratory (NREL) [23]. The original code, developed by R. Forristal, simulates a thermodynamic model that explores the operation of a parabolic trough collector as a function of irradiance, HTF inlet conditions, and wind speed. The results obtained by Forristal have been validated with experimental results from the field, demonstrating the validity of the thermal-fluid dynamics model adopted [23].

The correlations originally used in the code considered incompressible heat transfer fluids (HTF). A first modification was then necessary, adapting the correlations to the sCO₂ case, which cannot be assumed to be incompressible. The code for a single collector was then integrated within a more general code, simulating the functioning of an actual solar field composed by an arbitrary number loops in which multiple collectors are connected in series. The code also includes the simulation of the piping system connecting the loops to each other, and the solar field to the power section. The piping was dimensioned in detail, and characterized evaluating both heat losses and pressure drops along the pipes.

3.1.1.1 COLLECTOR DESCRIPTION

A picture of a typical parabolic trough collector (PTC) is shown in Fig. 3-1. Mirrors are shaped in the form of a parabola, in order to focus the sun rays on the receiver tube. The reflectors are put in place by a support structure that also ensures their movement throughout the day: a control unit operates on the support, following the position of the sun and maintaining the aperture plane perpendicular to the incoming rays.

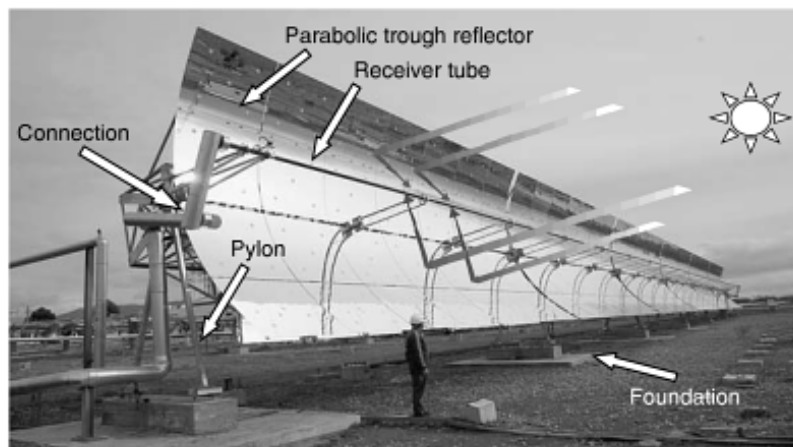


Fig. 3-1: parabolic trough collector [24]

The PTC selected for our project is an Euro Trough (ET) 100. This collector is especially designed for large power plants applications [24]. In Table 3-1: geometrical parameters of ET100 [24] the geometric dimensions of the collector are listed.

Table 3-1: geometrical parameters of ET100 [24]

Overall length of a single collector [m]	98.5
Number of parabolic trough modules per collector	8
Gross length of every module [m]	12.27
Parabola width	5.76
Number of ball joints between adjacent collectors	4
Net collector aperture per collector (m ²)	548.35

3.1.1.2 HEAT TRANSFER MODEL DESCRIPTION

The EES code simulates the operating conditions of the collectors by solving an energy balance between the different heat fluxes involved. These fluxes represent the conductive, convective and radiative heat transfer process between the collector and the environment. A schematic of this interaction is presented in Fig. 3-3.

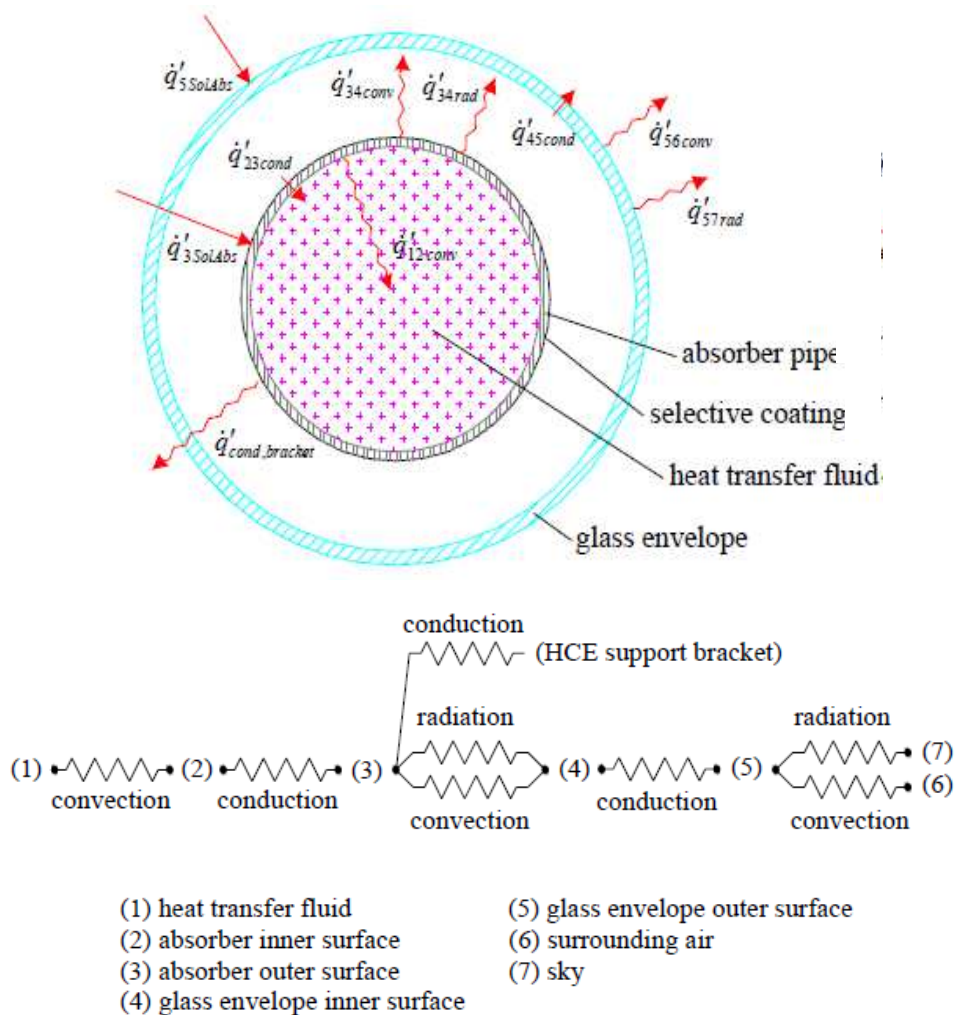


Fig. 3-3: energy balance on the receiver cross section and equivalent thermal resistances scheme[23]

The incoming solar radiation is partly absorbed by the glass envelope. The low reflectivity of glass limits the fraction of radiation that is reflected back, but in order to reduce even further this loss the surface of the glass envelope can be treated. The rest of the radiation is transmitted through the glass and reaches the absorber pipe, where it is captured thanks to the selective coating with high absorptivity coefficient applied on the receiver. Part of this energy is then transferred across the metal wall and into the HTF, while the remaining part is lost to the environment both as convective and radiative fluxes. Also the brackets sustaining the receiver cause an additional heat loss, behaving as fins and conducting part of the thermal energy.

Subscripts on the heat flux terms refer to the surfaces that have to be considered as geometrical boundaries of the heat transfer process (as listed in Table 3-2), whereas the apexes indicate that we are considering heat fluxes per unit length of the collector. A detailed list of the terms indicated in Fig. 3-3 is also presented in Table 3-3.

Table 3-2 : interface subscripts

1	HTF
2	Inner absorber pipe wall
3	Outer absorber pipe wall
4	Inner glass envelope wall
5	Outer glass envelope wall
6	Ambient
7	Sky

Heat Flux (W/m)*	Heat Transfer Mode	Heat Transfer Path	
		From	To
\dot{q}'_{12conv}	convection	inner absorber pipe surface	heat transfer fluid
\dot{q}'_{23cond}	conduction	outer absorber pipe surface	inner absorber pipe surface
$\dot{q}'_{3SolAbs}$	solar irradiation absorption	incident solar irradiation	outer absorber pipe surface
\dot{q}'_{34conv}	convection	outer absorber pipe surface	inner glass envelope surface
\dot{q}'_{34rad}	radiation	outer absorber pipe surface	inner glass envelope surface
\dot{q}'_{45cond}	conduction	inner glass envelope surface	outer glass envelope surface
$\dot{q}'_{5SolAbs}$	solar irradiation absorption	incident solar irradiation	outer glass envelope surface
\dot{q}'_{56conv}	convection	outer glass envelope surface	ambient
\dot{q}'_{57rad}	radiation	outer glass envelope surface	sky
\dot{q}'_{36conv}	convection	outer absorber pipe surface	ambient
\dot{q}'_{37rad}	radiation	outer absorber pipe surface	sky
$\dot{q}'_{cond,bracket}$	conduction	outer absorber pipe surface	HCE support bracket
$\dot{q}'_{HeatLoss}$	convection and radiation	heat collecting element	ambient and sky

* Per unit aperture length.

Table 3-3 : heat flux terms in cross sectional energy balance [23]

The two terms representing the absorbed solar radiation ($q_{3SolAbs}$ and $q_{5SolAbs}$) can be determined from the value of DNI and the optical parameters of the concentrating mirror and the absorber. All the other fluxes are function of the surfaces temperatures. Writing an energy balance for each one of the interfaces in the collector, using the functions of the temperatures expressing the various heat fluxes, we can obtain an equation system that, once solved, provides us with the temperature values. Specifically, the four interfaces considered to write the system energy balances are (i) the inner side of the absorber pipe and the HTF, (ii) the annulus and the outside of the absorber pipe, (iii) the inner side of the glass envelope and the annulus, and (iv) the outside of the glass envelope and the environment. The energy that comes into each interface has to balance the energy that exits.

$$\left\{ \begin{array}{l} q'_{12,conv} = q'_{23,cond} \\ q'_{3,SolAbs} = q'_{23,cond} + q'_{34,conv} + q'_{34,rad} + q'_{cond,bracket} \\ q'_{34,conv} + q'_{34,rad} = q'_{45,cond} \\ q'_{5,SolAbs} + q'_{45,cond} = q'_{56,conv} + q'_{57,rad} \end{array} \right. \quad (3-1)$$

T_6 and T_7 are inputs of the problem, representing the ambient conditions in which the collector is operating. Thus, once assuming a temperature for the HTF (T_1), a set of 4 equations and 4 variable (temperatures from 2 to 5) can be obtained, and the solution of the system can be univocally determined.

Considering a portion of the collector in which the HTF inlet conditions are specified, there are two approaches to determine its outlet temperature and pressure:

1. **One-dimensional approach:** the cross sectional heat balance is solved for the inlet section, where T_1 and p_1 are already known. The outlet conditions are then calculated assuming a constant behavior along the length of the portion, neglecting the changes induced by the evolution of the temperature profiles on heat fluxes and pressure drop.
2. **Two-dimensional approach:** the collector is discretized along the receiver length and the cross sectional heat balance is solved for the middle section of each longitudinal portion. Temperature and pressure of the HTF in this section are obtained as average of the inlet and outlet values. The outlet conditions of each portion are obtained with a longitudinal energy balance.

The one dimensional approach has proved to be accurate only for short collectors, in which the change in temperature and pressure of the HTF is modest [23]. In this work, the two-dimensional approach is adopted: it is an implicit method, and does not allow the decoupling of the solution of the cross sectional heat balance and the calculation of the outlet conditions, but it is more accurate.

In order to solve the cross sectional energy balance then, inlet and outlet conditions have to be related somehow. This can be done operating a longitudinal energy balance on the HTF. Considering constant the conductive

fluxes in the axial direction through inlet and outlet sections, the only terms involved in the balance are internal and kinetic energy transport through these sections, and thermal energy flux entering the HTF from the walls of the absorber. The resulting energy balance is in the form of:

$$q'_{in,HTF} \cdot L = \dot{m} \cdot \left[\left(h_{out} + \frac{1}{2} v_{out}^2 \right) - \left(h_{in} + \frac{1}{2} v_{in}^2 \right) \right] \quad (3-2)$$

equivalent to say that the heat input in the HTF is equal to the change in its total energy (potential energy variations are neglected). The heat flux entering the fluid can be determined from the convective heat transfer between the inner wall of the absorber pipe and the HTF:

$$q'_{in,HTF} = q'_{12,conv} \quad (3-3)$$

As for the enthalpies and velocities, they are a function of temperature and pressure of the section. The function library available in EES for compressible fluids has been used to calculate CO₂ properties (density, viscosity, enthalpy). The velocity in a section can then be calculated as:

$$v = \frac{\dot{m}}{\rho(T,p) \cdot A} \quad (3-4)$$

Since two properties are required to characterize the thermodynamic state of the fluid at the exit, another equation is necessary. Inlet and outlet pressures can be related estimating the pressure drop due to friction in a horizontal cylindrical pipe:

$$p_{out} = p_{in} - \Delta p \quad (3-5)$$

$$\Delta p = f_{ave} \cdot \left(\frac{L}{D} \right) \cdot \rho_{ave} \cdot \left(\frac{v_{ave}^2}{2} \right) \quad (3-6)$$

Where f is the Darcy friction factor, determined using Colebrook relation:

$$\frac{1}{\sqrt{f_{ave}}} = -2 \log_{10} \left(\frac{\varepsilon}{3,71 \cdot D} + \frac{2,51}{Re_{D,ave} \cdot \sqrt{f_{ave}}} \right) \quad (3-7)$$

ε is the roughness of the pipe, and $Re_{D,ave}$ is the Reynolds number on the middle section, and is calculated as:

$$Re_{D,ave} = \frac{\rho_{ave} \cdot D \cdot v_{ave}}{\mu_{ave}} \quad (3-8)$$

Where μ_{ave} is the average dynamic viscosity of the fluid.

Solving the system constituted by equations from (3-1) to (3-8), the outlet conditions of the HTF can be determined. The solution process is carried out automatically by EES. This procedure can be followed for each one of the modules of the PTC, starting from the inlet of the collector and considering as input for the following module the outlet of the preceding one.

In our case, the final temperature condition of the HTF is known, since a constant inlet temperature for the turbine downstream the SF is set. If inlet condition of the HTF and length of the collector are both fixed, the outlet temperature control can be operated modulating the value of mass flow delivered into the row: increasing the mass flow in a collector will reduce the exit temperature of the stream from that collector, since the thermal capacity of the HTF stream is going to be higher, and more energy will be necessary to raise its temperature. In alternative, maintaining the inlet condition of the HTF and the irradiance, longer rows will guarantee higher outlet temperatures.

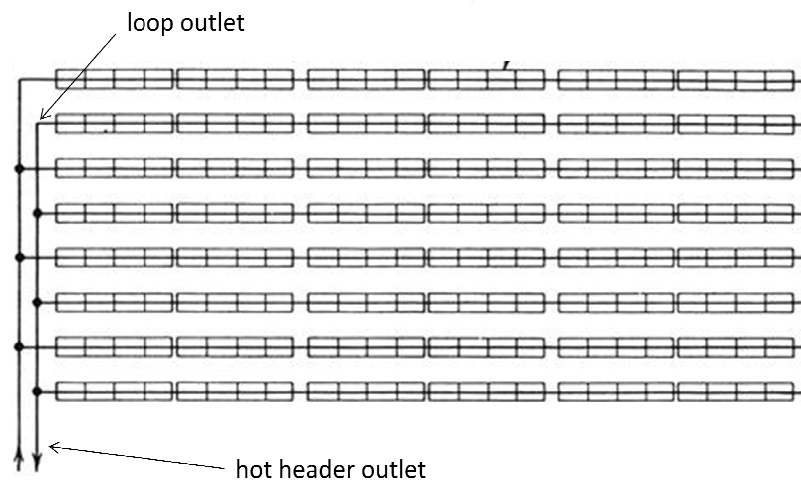


Fig. 3-4 : solar field schematic

If the whole solar field is considered, instead of a single collector, the final temperature condition will be set at the outlet of the hot piping, that is where the flux goes back in the power block and enters the turbine (Fig. 3-4). This

temperature will be determined by the mixing processes in the hot header collecting the fluxes coming from all the loops, and by the entity of heat loss along the header.

The relation between energy fluxes and temperatures of the surfaces was implemented in EES in the form of functions. In the next paragraph a description of each one of the functions is provided, focusing on the correlations used and the assumptions made. Temperature subscripts refer to Table 3-2 : interface subscripts.

3.1.1.3 EES FUNCTIONS DESCRIPTION

Convective heat transfer between HTF and absorber

To model the convection between the inner wall of the absorber tube and the CO₂, Newton's law has been used:

$$q'_{12,conv} = h_1 \pi D_2 (T_2 - T_1) \quad (3-9)$$

$$h_1 = Nu_{D2} \frac{k_1}{D_2} \quad (3-10)$$

Where:

h_1 = convective heat transfer coefficient [W/m²-K]

D_2 = absorber pipe inner diameter [m]

Nu_{D2} = Nusselt number calculated using D_2

k_1 = thermal conductivity of HTF

To calculate the Nusselt number, a modified Gnielinsky correlation was used:

$$Nu_{D2} = \frac{\frac{f_2}{8} Re_{D2} Pr_1}{1,07 + 12,7 \sqrt{\frac{f_2}{8}}} (Pr_1^{\frac{2}{3}} - 1) \quad (3-11)$$

Where:

f_2 = friction factor at the inner surface of the absorber tube

Pr_1 =HTF Prandtl number evaluated at T_1

The correlation is valid for $0.5 < Pr_1 < 2000$ and $2300 < Re_{D_2} < 5E06$, covering turbulent and transitional flow conditions. Warnings were set in order to ensure that the correlation limits are fulfilled. This correlation was preferred to the one implemented in the original version of the Forristal code on the base of its good agreement with experimental results obtained by the group of professor J. Muñoz in the experimental facility built in Almeria, Spain [26].

The friction factor is again calculated using Colebrook relation [eq. (3-7)].

Conductive heat transfer through absorber pipe wall

The absorption of the incoming solar radiation is assumed to take place only on the external surface of the pipe, where the selective coating is applied. This is of course an approximation, but allows neglecting a power generation term in the solution of the conduction problem through the metal.

Fourier's law equation for conductive heat transfer without distributed energy source in cylindrical coordinates has thus been implemented:

$$q_{23,cond} = \frac{2\pi k_{23}(T_3 - T_2)}{\ln\left(\frac{D_3}{D_2}\right)} \quad (3-12)$$

where:

k_{23} = thermal conductivity of absorber pipe wall evaluated at $T_{23} = \frac{T_2 + T_3}{2}$ [W/m-K]

D_3 = absorber pipe outer diameter [m]

D_2 = absorber pipe inner diameter [m]

The thermal conductivity depends on the material selected for the pipe and its average temperature. In our case (austenitic stainless steel), the following linear correlation was used [23]:

$$k_{23} = 0.013 \cdot T_{23} + 15 \quad \left[\frac{W}{mK}\right] \quad (T_{23} \text{ in } ^\circ C) \quad (3-13)$$

Radiative Heat transfer from the absorber to the glass envelope

Both a convective and radiative heat transfer occurs between the glass envelope and the absorber. The radiation was modeled using the following relation:

$$q_{34,rad} = \frac{\sigma \pi D_3 (T_3^4 - T_4^4)}{\frac{1}{\varepsilon_3} + \frac{(1 - \varepsilon_4) D_3}{\varepsilon_4 D_4}} \quad (3-14)$$

where:

σ = Stefan-Boltzmann constant [W/m²K⁴]

D_3 = absorber pipe outer diameter [m]

D_4 = glass envelope inner diameter [m]

ε_3 = emissivity of absorber pipe coating

ε_4 = emissivity of glass envelope

The emissivity of the glass is considered to be constant and equal to 0.86, whereas the emissivity of the selective coating is a function of the average absorber wall temperature as follows [25]:

$$\varepsilon_3 = 2,64 \cdot 10^{-7} T_{23}^2 + 1,25 \cdot 10^{-5} T_{23} + 0,054 \quad (3-15)$$

Convective Heat transfer from the absorber to the glass envelope

The mechanism of convection in the annulus between the glass envelope and the absorber is free molecular convection, since the annulus is maintained under vacuum conditions (i.e. few Pascal). The correlation used to describe this phenomena is the following:

$$q'_{34,conv} = \pi D_3 h_{34} (T_3 - T_4) \quad (3-16)$$

with:

$$h_{34} = \frac{k_{std}}{\frac{D_3}{2 \ln\left(\frac{D_4}{D_3}\right)} + b \lambda \left(\frac{D_3}{D_4} + 1\right)} \quad (3-17)$$

$$b = \frac{(2-a)(9\gamma-5)}{2a(\gamma+1)} \quad (3-18)$$

$$\lambda = \frac{2.331 \cdot 10^{-20} T_{34}}{P_a \delta^2} \quad (T_{34} \text{ in K}) \quad (3-19)$$

where:

D_3 = outer diameter of absorber tube [m]

D_4 = inner diameter of glass envelope [m]

h_{34} = convection heat transfer coefficient for annulus gas at $T_{34} = \frac{T_3 + T_4}{2}$ [W/m²-K]

k_{std} = thermal conductance of annulus gas at standard conditions [W/m-K]

b = interaction coefficient

λ = mean free path between molecules collision [cm]

a = accommodation coefficient

γ = ratio of specific heats of annulus gas

P_a = annulus gas pressure [mmHg]

δ = molecular diameter of annulus gas [cm]

Among the three gases proposed by Forristal in his work, the annulus gas considered is hydrogen, and the annulus pressure imposed is of 10^{-4} mmHg, leading to the following values for the gas constants:

δ [cm]	2.4E-8
b [-]	1.582
λ [cm]	196.3
k_{std} [W/m-K]	0.1769

Table 3-4 : gas constants

The annulus is assumed to maintain its condition of low vacuum, excluding the case of a damage to the glass envelope with consequent loss of insulation for the absorber.

Conductive heat transfer in glass envelope wall

This is the same situation as the conduction through the wall of the absorber. Again, the absorption of the radiation is assumed to take place on the outside surface of the glass:

$$q_{45,cond} = \frac{2\pi k_{45}(T_5 - T_4)}{\ln\left(\frac{D_5}{D_4}\right)} \quad (3-20)$$

The thermal conductance of the glass is assumed to be constant and equal to 1.04 W/m-K [23].

Convective heat transfer from glass envelope to atmosphere

The mechanism of convection in this case is strictly related to the wind speed: when the wind speed is very low or zero, natural convection occurs, whereas when the wind speed is relevant forced external convection has to be considered. In both cases, Newton's law of cooling is applied:

$$q'_{56,conv} = \pi D_5 h_{56} (T_5 - T_6) \quad (3-21)$$

$$h_{56} = Nu_{D5} \frac{k_{56}}{D_5} \quad (3-22)$$

where

h_{56} = convection heat transfer between glass envelope and environment [W/m²-K]

k_{56} = thermal conductance of air at $T_{56} = \frac{T_5 + T_6}{2}$ [W/m-K]

D_5 = outer diameter of glass envelope

The distinction between the two cases is in the correlations used to calculate the Nusselt number:

Natural convection (no wind case)

In this case, the correlation developed by Churchill and Chu is implemented:

$$\overline{Nu}_{D5} = \left\{ 0.60 + \frac{0.387 Ra_{D5}^{\frac{1}{4}}}{\left[1 + \left(\frac{0.559}{Pr_{56}} \right)^{\frac{9}{16}} \right]^{\frac{8}{27}}} \right\}^2 \quad (3-23)$$

$$Ra_{D5} = \frac{g\beta(T_5 - T_6)D_5^3}{\alpha_{56}v_{56}} \quad (3-24)$$

$$\beta = \frac{1}{T_{56}} \quad (3-25)$$

$$Pr_1 = \frac{v_{56}}{\alpha_{56}} \quad (3-26)$$

where:

Ra_{D5} = Rayleigh number for air based on glass envelope outer diameter

g = gravitational acceleration (9.81 [m/s²])

α_{56} = thermal diffusivity for air at $T_{56} = \frac{T_5 + T_6}{2}$ [m²/s]

β = volumetric thermal expansion coefficient (ideal gas) [1/K]

Pr_{56} = Prandtl number for air at T_{56}

v_{56} = kinematic viscosity for air at T_{56} [m²/s]

The correlation assumes a long isothermal cylinder, and its range of validity is $10^5 < Ra_{D5} < 10^{12}$.

Forced convection (wind case)

If wind is blowing, forced convection will take place between the glass envelope and the environment. The Nusselt number is then calculated using Zhukauskas' correlation. Again, the assumption is isothermal cylinder, and the wind is assumed to be normal to the envelope at all time.

$$\overline{Nu}_{D5} = C Re_{D5}^m Pr_6^n \left(\frac{Pr_6}{Pr_5} \right)^{\frac{1}{4}} \quad (3-27)$$

The coefficients C and m assume the following values in function of the Re_{D5} :

Re_{D5}	C	m
1-40	0.75	0.4
40-1000	0.51	0.5
1000-200000	0.26	0.6
200000-1000000	0.076	0.7

Table 3-5 : Zhukauskas' coefficients

The exponent for the Prandtl number n depends on the value of the Prandtl itself, as follows:

$$\begin{aligned} n &= 0.37, \text{ for } Pr \leq 10 \\ n &= 0.36, \text{ for } Pr > 10 \end{aligned} \quad (3-28)$$

The range of validity for the correlation is $0.7 < Pr_6 < 500$, and $1 < Re_{D5} < 10^6$. Fluid properties are evaluated at T_6 .

Radiative heat transfer from glass envelope to environment

This term only considers the radiation heat loss from the glass envelope, since the portion of solar radiation absorbed by the envelope is considered separately as it will be explained later. The reciprocal irradiation between the envelope and the surroundings is modeled considering the sky as a black body at an equivalent temperature equal to the ambient temperature minus 8 °C.

$$q'_{57,rad} = \sigma D_5 \pi \varepsilon_5 (T_5^4 - T_7^4) \quad (3-29)$$

where:

σ = Stefan-Boltzmann constant (5.67E-08 [W/m²-K⁴])

D_5 = glass envelope outer diameter [m]

ε_5 = glass envelope emissivity

Solar radiation absorption:

Compared to the original Forristal code, the modeling of the optical system was changed.

First of all the effect of the existing angle between the incoming sun rays and the aperture plane of the collector (that is the plane on which the two edges of the parabolic mirrors lay), was modeled outside EES, allowing, when mapping the operation of the plant in order to explore its annual performance, to consider as variable only the effective DNI (EDNI), that is the product of the actual DNI with correction factors accounting for effects caused by the relative position of the sun and the collector. The description of the effective DNI calculation will be undertaken in chapter 5.

Once the value of EDNI is known, the incoming radiation per unit length can be calculated, referred to the considered collector. Not all of its length though is useful to the absorption of radiation, since it has to be considered also that part of it is constituted by the connection between the modules (as can be seen in Fig. 3-2: receiver scheme. The absorber tube is protected by a glass envelope [23]), and does not participate to the absorption process. To this purpose, two different lengths for the PTC modules were defined: the physical length of the module, and the effective length of the absorber, respectively of 12.29 m and 11.9 m. The incoming radiation per unit length, in order for it to be homogeneous with the heat fluxes listed so far, was then calculated as:

$$q'_i = EDNI \cdot \frac{Width_{parabola} \cdot L_{absorber}}{L_{module}} \quad (3-30)$$

From the value incident radiation on the collector per unit length, the values of $q_{3SolAbs}$ and $q_{5SolAbs}$ can be calculated considering the optical properties of the reflectors and the materials. Specifically:

$$q'_{5,SolAbs} = q'_i \cdot \gamma \cdot \rho_{mirrors} \cdot \alpha_{45} \quad (3-31)$$

$$q'_{3,SolAbs} = q'_i \cdot \gamma \cdot \rho_{mirrors} \cdot \tau_{45} \cdot \alpha_{23} \quad (3-32)$$

where:

$\rho_{mirrors}$ = reflectivity of PTC mirrors
 γ = intercept factor
 α_{45} = absorptance of glass envelope
 τ_{45} = transmittance of glass envelope
 α_{23} = absorptance of selective coating

The intercept factor is introduced to consider that not all the rays reflected by the mirrors are actually conveyed on the receiver, because of focusing errors that include geometrical errors (specularity error, mirror slope error, receiver position error), collector tracking error, as well as the effect of the finite dimension of the sun [27]. The value assumed for the calculation was taken from the experimental measurements reported in [28]. Mirrors are assumed to be clean, so no fouling coefficient is used.

Optical parameters assumed are listed in Table 3-6.

$\rho_{mirrors}$	0.943
α_{45}	0.02
τ_{45}	0.945
α_{23}	0.94
γ	0.975

Table 3-6 : values of the optical parameters implemented in EES code

Fixing the parameters listed above is the same as establishing a nominal optical efficiency for the collector: Nominal optical efficiency is the peak optical efficiency when the sun beam is perfectly normal to the aperture plane. This optical efficiency can be defined as:

$$\eta_{opt,nom} = \frac{q'_{3,SolAbs}}{q'_i} \quad (3-33)$$

Comparing eq. (3-32) and (3-33) we can see how the nominal optical efficiency in our case is given by:

$$\eta_{opt,nom} = \gamma \cdot \rho_{mirrors} \cdot \tau_{45} \cdot \alpha_{23} \quad (3-34)$$

and, with the assumptions made, results equal to 81,72%.

As already pointed out, the process of absorption of the solar radiation is supposed, both for the envelope and the absorber, to take place on the external surface, and it is not considered (as it actually is) as a distributed power generation throughout their walls.

Heat loss through support Brackets

Part of the radiation absorbed by the receiver, is conducted by the support brackets: these are the metal bars that maintain the collector in the focal position. The behavior of these brackets can be modeled as infinite length fins. The value of temperature where the bracket connects to the absorber tube is estimated to be 10 °C less than the value on the external surface of the absorber (T_3). The heat loss is then calculated according to the following equation:

$$q'_{cond,bracket} = \sqrt{\bar{h}_b P_b k_b A_{cs,b}} \frac{(T_{base} - T_6)}{L_{HCE}} \quad (3-35)$$

where:

\bar{h}_b = average convection coefficient along bracket [W/m²-K]

P_b = perimeter of bracket [m]

k_b = conduction coefficient of bracket [W/m-K]

$A_{cs,b}$ = minimum cross sectional area of bracket [m²]

T_{base} = temperature at the base of the bracket

L_{HCE} = collector length [m]

The convection coefficient is calculated using the same correlations indicated in the case of the convective heat exchange between the glass envelope and the environment. The effective diameter of the bracket is assumed to be 2 inches. The average temperature used in the correlation was set to be equal to $(T_{base} + T_6)/3$: this value has been determined by Forristal based on the good agreement of the computation results with the experimental data.

3.1.1.4 PARAMETRIC ANALYSIS

To validate the developed EES model and analyze the effect of assumed parameters on the performance of the collector, some parametric studies were run, considering the influence of HTF temperature, EDNI, wind speed and collector length on the thermal and global efficiency of the PTC.

First of all, temperature profiles obtained from the simulation of a fixed length collector when a determined mass flow is passing through it were compared with the same simulation (at the same radiation and wind conditions) computed using the version of Forristal's code written by Alessia Robbiati in her thesis [29]. The temperature profiles obtained are shown in Fig. 3-6: relative error between results 5, whereas the relative error with respect to the reference results is shown in Fig. 3-6. The increasing difference between temperature values is due to the propagation of the errors induced by having slightly different databases for the thermodynamic properties of CO₂ (EES uses an internal database different from REFPROP), and from small differences in the choice of the correlations to be used (for example in the case of internal convection). The relative error remains though very small.

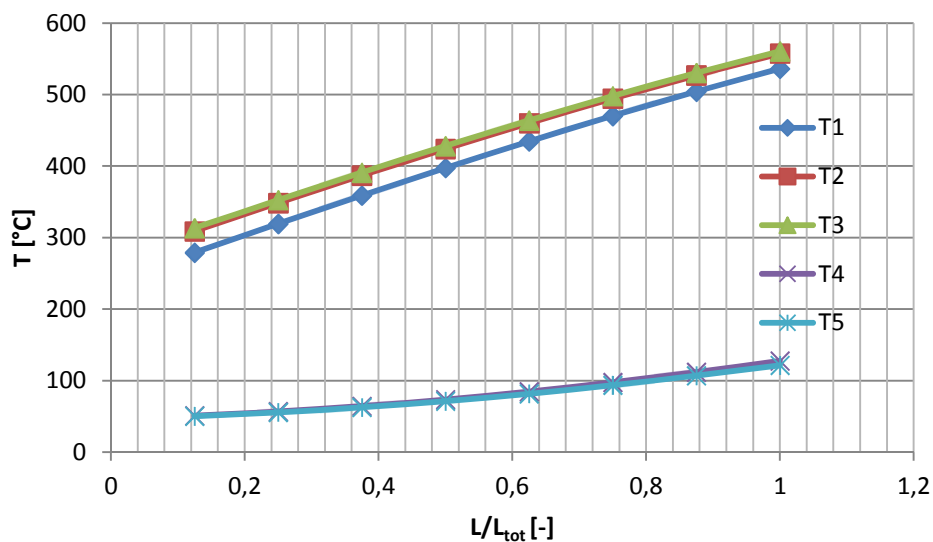


Fig. 3-5 : temperature profiles along collector length ($T_{in}= 250^{\circ}\text{C}$, $T_{out}=550^{\circ}\text{C}$)

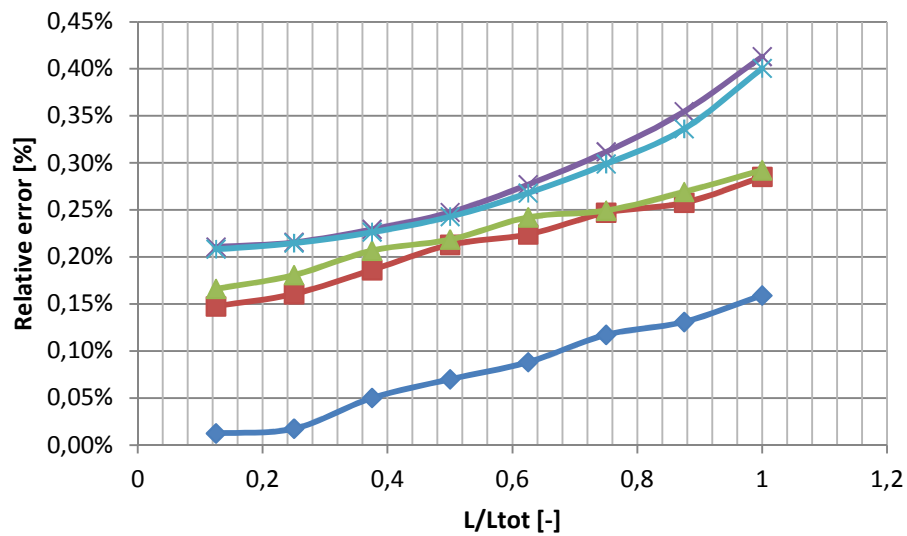


Fig. 3-6: relative error between results obtained from the EES code written for the current work and from the code written by Alessia Robbiati [29]

The thermal efficiency of an ET100 collector having inlet conditions of 250 °C and 100 bars and a desired outlet condition of 550 °C, was then mapped along its length, or equivalently at increasing average temperature of the HTF. Fig. 3-7 shows how, as the carbon dioxide bulk temperature increases, the thermal losses also increase with a consequent reduction of the collector thermal efficiency.

Thermal efficiency is defined as:

$$\eta_{th} = \frac{q'_{in,HTF}}{q'_i} = 1 - \frac{q'_{loss}}{q'_i} \quad (3-36)$$

where:

$$q'_{loss} = q'_{34,conv} + q'_{34,rad} + q'_{cond,bracket} \quad (3-37)$$

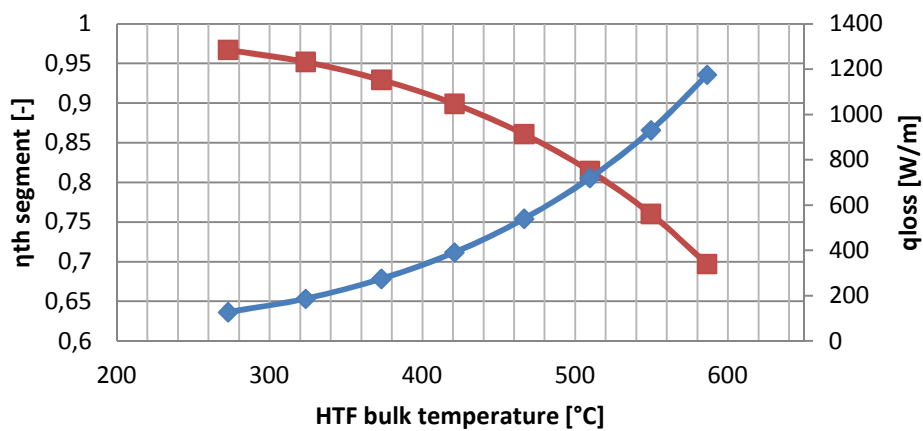


Fig. 3-7: collector thermal efficiency and heat losses as a function of HTF bulk temperature (EDNI=850 W/m², m_{HTF}=0,78 kg/s)

The physical explanation for this is that a higher value of the receiver external surface temperature implies higher radiative and convective fluxes towards the surroundings. The value of DNI has only a minor effect on the heat losses, for which the major dependency is on the HTF temperature. Having a higher input at the same HTF bulk temperature then improves the thermal efficiency of the collector, as the heat gained by the fluid becomes more relevant compared to the heat unexploited. This behavior is shown in Fig. 3-8, where η_{global} is the product of thermal and optical efficiency of the collector:

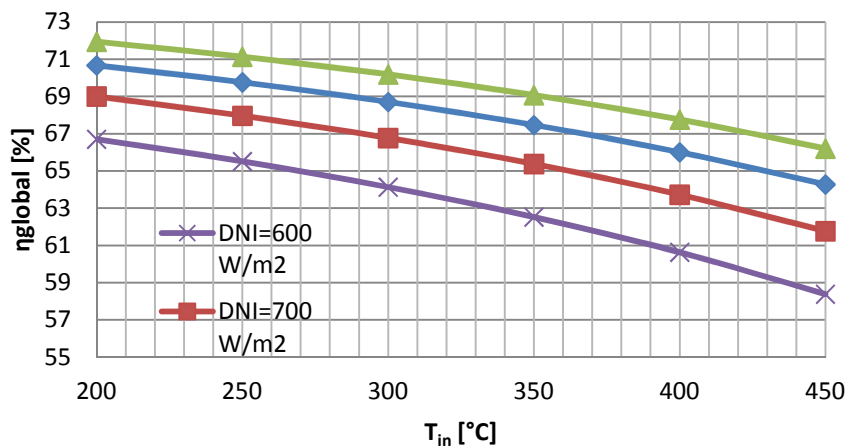


Fig. 3-8: global efficiency of the collector as a function of its inlet temperature, for different DNI values (T_{out}=600°C)

Another important parameter in the evaluation of the collector performance is the wind speed, which affects the value of convective heat transfer coefficient on the surface of the glass envelope and, in turn, of the heat loss to the environment. Increasing wind speed implies then lower collector efficiencies, as it can be seen in Fig. 3-9.

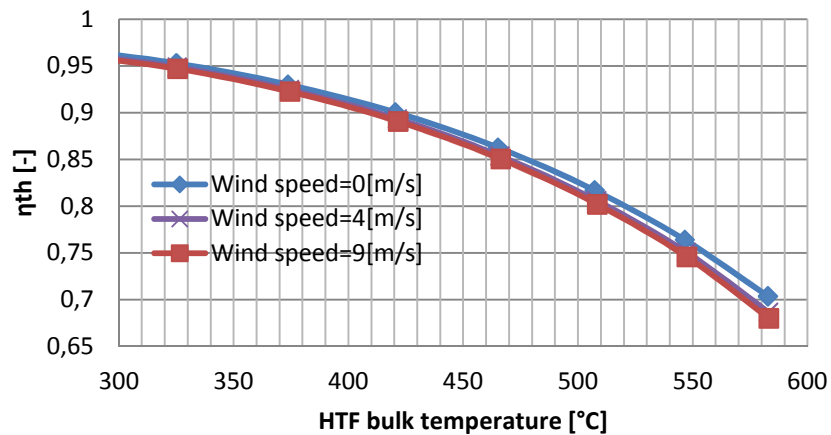


Fig. 3-9: thermal efficiency profile as a function of HTF bulk temperature at different wind speeds

Increasing wind speeds affect less and less the heat loss, as the surface temperature of the envelope gradually approaches the ambient temperature.

The length of a single ET100 is constant. In order to reduce the number of rows in the solar field, and thus its longitudinal dimension, maintaining the same nominal thermal capacity, an option would be to connect in series multiple collectors, increasing the length of each row: this would raise the total heat input associated with the row, reducing the total number of rows necessary to fulfill the thermal capacity requirement on the SF.

If inlet and desired outlet conditions are fixed, a longer row will affect the mass flow that is necessary to impose in it in order to guarantee those conditions: since the heat input will raise with the length, to maintain the specific enthalpy difference between inlet and outlet the mass flow will have to increase as well. In turn, this will imply higher HTF speed, and consequently larger friction factors. Pressure losses will also be raised by the fact that the HTF has to pass through a longer path. A study was thus performed to select how many ET100

collectors to connect in series in each row: in Fig. 3-10: pressure drop in SF and total number of rows as a function the trade-off between number of rows and total pressure drop can be visualized.

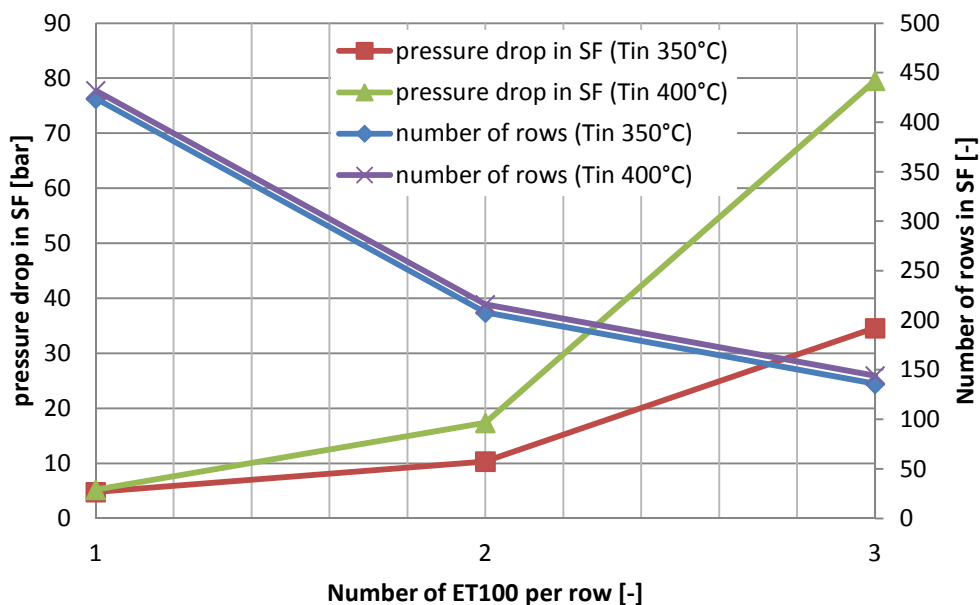


Fig. 3-10: pressure drop in SF and total number of rows as a function the number of ET100 connected in series in each row

Given the high temperatures at the inlet of the loop, a consequence of the necessary high degree of regeneration imposed in the power block to improve the efficiency, the temperature difference that the HTF has to undertake across each row is limited. If the length of the row is high then, to guarantee the desired outlet temperature the increase in mass flow will be extremely relevant, causing the pressure losses to rise very quickly. The higher the inlet temperature is, the more evident this behavior will be.

Since the pressure ratio of the considered power cycles is already limited by the resistance limits of the collectors, which allow a maximum pressure at the inlet of the SF of about 105 bars, and since already with two collectors per row have a large increase in the global pressure drop, the choice made was to limit the length of the rows to a single ET100, accepting to have a longer and more expensive piping system. A complete analysis would have to investigate the

impact of the collector length on the final energy cost, in order to evaluate the effect of the trade off on the most significant parameter.

3.1.2 SOLAR FIELD LAYOUT

During the design of the solar field, a constant nominal thermal power delivered in the HTF by the solar field was imposed, equal to what selected by the group of Prof. Muñoz during their study on DSG plants [30]. The nominal thermal capacity of the solar field is then fixed to 127MW_{th} . Since the selected length of the rows is modest, as well as the consequent mass flow in each one of them, the thermal input per row is going to be low, and a large number of them will be needed to fulfill the requirement. It is then necessary to come up with a solar field layout that properly distributes the rows around the power block, and limits the length of the headers distributing the HTF coming from the power block to the field. The adopted configuration is shown in Fig. 3-12. Different colors correspond to different sections of the piping, as listed in the caption.

A choice had to be made between two possible headers layout: two or three pipes. The distinction between the two options is shown in Fig. 3-11. In a two pipes system the flow in the cold and hot headers is countercurrent: the HTF enters the cold header at the outlet from the power block and is directly distributed in the rows. In this layout the distance that the fraction of HTF flow sent to each row has to go through is different. This will cause the pressure drops in each stream to be different as well, and valves will have to be used in order to balance the pressures at the mixing points.

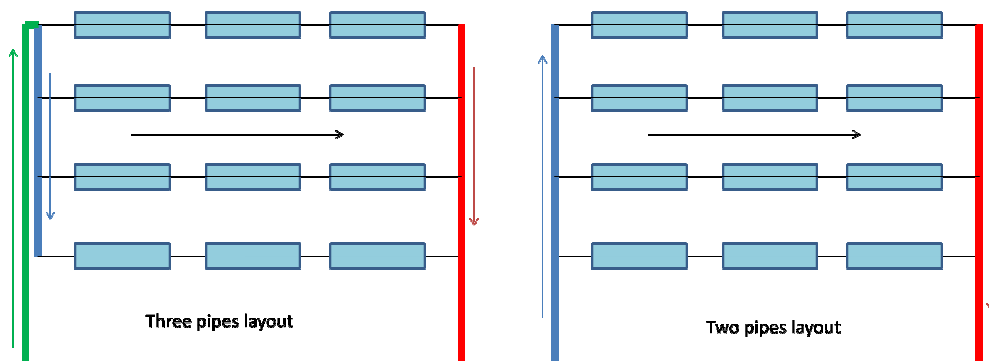


Fig. 3-11 : two and three pipes layout

To avoid this problem, a three pipes configuration was selected: the HTF is first led to the end of the solar field, and then enters the cold header. After being heated up in the rows, the HTF is finally collected by the hot header, and led back to the power section.

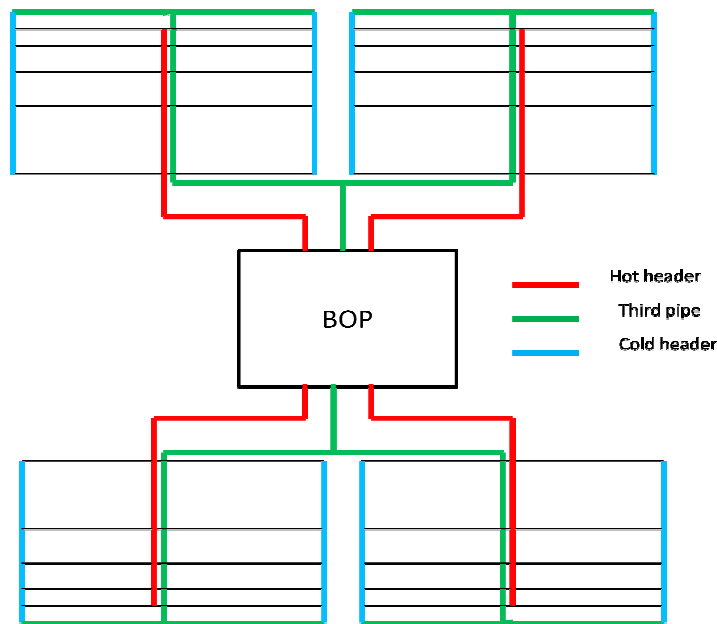


Fig. 3-12: solar field layout. The HTF is conveyed by the third pipe in the cold headers, distributed in the rows constituting the 8 symmetric sections of the SF, and collected back in the hot headers.

The third pipe balances the pressure losses across the different paths that the HTF follows: independently from which row the HTF is destined to, the total length it has to undergo is the same. This helps not to have an uneven flow distribution in the rows, and limits the need for control valves in the solar field. On the other hand, the presence of a third pipe represents an additional cost.

Eight symmetrical sections can thus be identified in the solar field: it can be simulated the operation of one of them, and assume that they all behave in the same way.

Based on the results obtained by Alessia Robbiati [29], the behavior of the intermediate rows in each section can be approximated to be linear, with respect to outlet enthalpy and pressure. Only the first and last rows were then simulated, avoiding the need for an ad hoc simulation in each one of the rows,

and the values of outlet enthalpy and pressures were then estimated for the intermediate rows with a linear interpolation.

3.1.3 PIPING DIMENSIONING AND HEAT LOSS / PRESSURE DROP CALCULATION

To compute pressure drops along the piping, a procedure analogous to the one described for the solar field collectors has been implemented. Darcy friction factor has been calculated in the middle section of the piping segment considered, using Colebrook correlation, eq. (3-7). The total pressure drop was then obtained from eq. (3-6). As for the heat losses, the tubes were assumed to be insulated, and the temperature for the outer surface of the insulation coating was set to be 40 °C, dimensioning the thickness of the external coating accordingly.

The first step towards the determination of the three diameters characterizing the pipes (inner diameter and external diameter of the pipe, and diameter of the coating), is to start from the influence of the internal diameter of the pipe on the velocity of the flow. A desired average speed was then imposed in each section considered: knowing the value of mass flow and the average density of the HTF, the diameter was calculated as:

$$D_{in,pipe} = \sqrt{\frac{4\dot{m}_{HTF}}{\pi\rho_{ave}v_{ave,ddesired}}} \quad (3-38)$$

Average density is function of average temperature and pressure, and is thus depending on the diameter itself (that affects the heat loss and pressure drop value across the pipe), and of course the HTF inlet conditions. The sizing of each segment of piping has therefore to be performed contextually to the solution of the solar field.

The third pipe was divided into segments, and for each one of them a diameter was calculated. The speed imposed in the third pipe is 10 m/s. This value is higher than what selected for the cold header, since the mass flow in the third pipe is double.

Hot and cold headers were treated differently. Since the mass flow is not constant in both of them, as in each intersection with a row a portion of the

flux is deviated or introduced, to guarantee reasonable speeds along the whole length of the header the inner diameter was changed after each junction. The concept is illustrated in Fig. 3-13 in the case of the cold header.

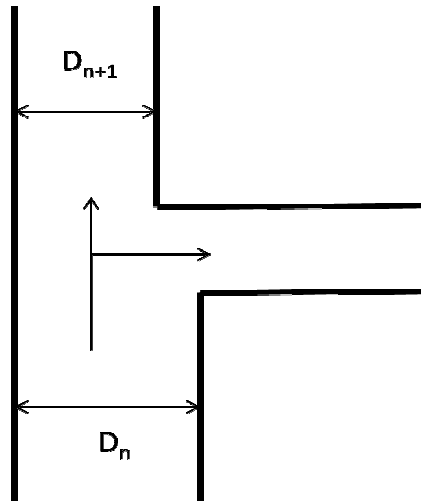


Fig. 3-13: cold header T junction

Along the cold header a procedure analogous to the one followed for the third pipe was implemented in each segment connecting two consecutive loops. The imposed flow speed is equal to 8 m/s, on the base of the optimization study performed by Robbiati [29]. In dimensioning the hot header though, an additional factor had to be taken in consideration.

As already said, the behavior of intermediate rows was linearly approximated between the pressure and enthalpy outlet conditions in the first and the last row. Pressures of the streams exiting each row and flowing into the hot header are then a linear function along the header length. These pressures need to be balanced with the pressure of the main stream flowing in the header: otherwise pressure unbalance leads to readjusting the flow in the row in order to adapt the outlet pressure. This would cause the rows to work with uneven flows, and the assumption of linear behavior would not be justified anymore. Furthermore, the outlet temperatures would be difficult to control, and the final temperature at the inlet of the turbine might differ from the desired value.

The unbalance caused by a constant speed in the hot header is shown in Fig. 3-14.

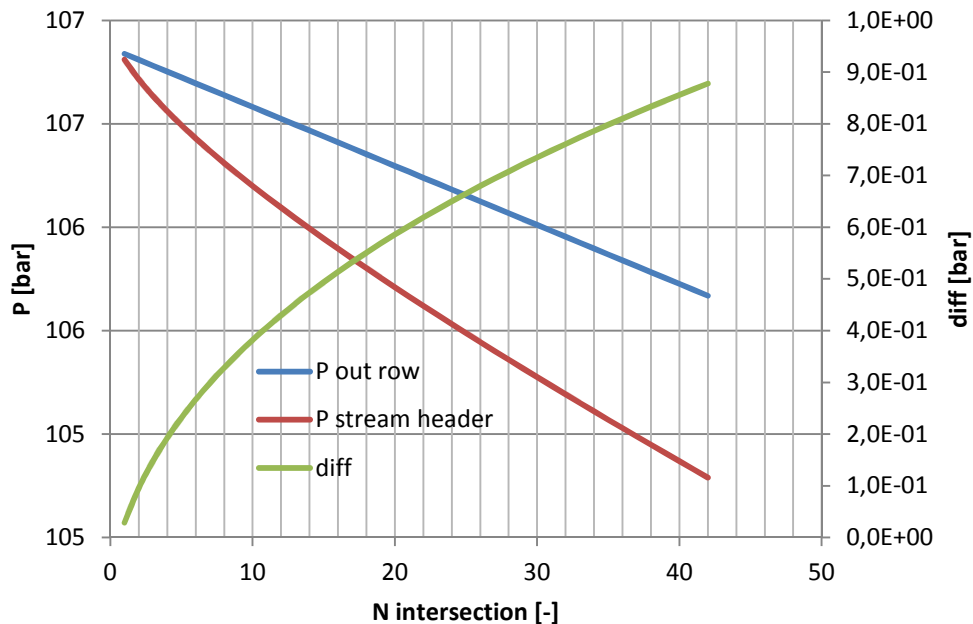


Fig. 3-14: unbalance at the intersections between outlet pressure from rows and pressure of the main stream in the hot header

The red line represents the pressure value of the main stream flowing in the header, whereas the blue line shows the linear approximation for the outlet pressures of the rows. The pressure difference between flows at the T junctions builds up to about 90 kPa: what would happen then is that a larger current would tend to flow in the latest rows, until the outlet pressure of the row drops enough to reach the pressure of the main stream.

The solution to this problem was to adapt the sizing of the hot header diameters in order to minimize pressure differences between the streams. This was done by introducing a variable exponent in equation (3-38), in the form of:

$$D_{hothead\ segment} = \left(\frac{4\dot{m}_{HTF}}{\pi\rho_{ave}v_{ave,desired}} \right)^n \quad (3-39)$$

In order to calculate the value of n , the same pressure was imposed for the last row exit and the main stream arriving to the last T junction. The effect of this modification is shown in Fig. 3-15: pressure .

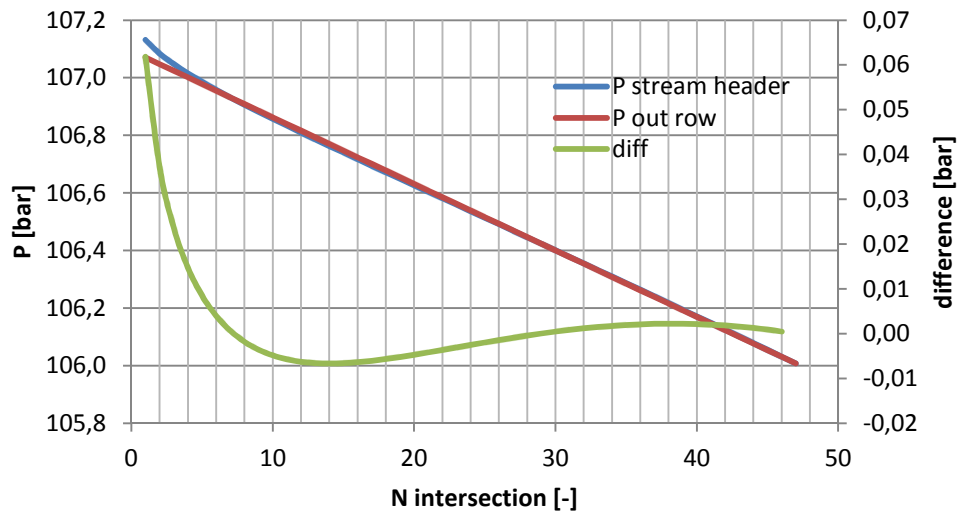


Fig. 3-15: pressure profiles at the intersections between outlet pressure from rows and pressure of the main stream in the hot header after diameter adaptation

Pressure differences at the T junctions between the rows and the hot header are now restricted to acceptable values, and the risk of uneven mass flow distribution is limited.

Contextually to the determination of the inner diameters of the piping, both thickness of the pipes and of the insulating coating have to be calculated, in order to properly take into account thermal losses that will affect the temperature profile along the piping and thus the values of average temperature and pressure employed in the calculation of pressure drops. A scheme of the cross section of the pipes is shown in Fig. 3-16.

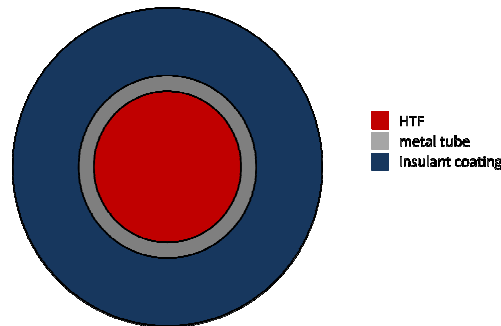


Fig. 3-16 : cross section of insulated pipe

The calculation of the thickness of the pipes is carried out in order to guarantee the mechanical resistance of the pressurized tube. Considering the difference between average inner pressure and ambient pressures, and the maximum stress to which the material constituting the pipes can resist (σ_{adm}), the thickness t can be calculated as [47]:

$$t = \frac{(p_{ave} - p_{amb}) \cdot D_{in}}{2 \cdot \frac{\sigma_{adm}}{1.5} - 1.6 \cdot (p_{ave} - p_{amb})} \quad (3-40)$$

The coefficient 1.5 that divides the maximum allowable stress is a safety factor to prevent mechanical failures in the event of an unpredicted load exceeding what considered during the dimensioning.

The material selected for the cold header and third pipe is stainless steel P265GH. Its maximum allowable stress is a function of its temperature, as indicated in Table 3-7 [48].

Table 3-7 : maximum admissible stress as a function of temperature for stainless steel P265GH

T [°C]	100	150	200	250	300	350	400	450
σ_{adm} [MPa]	226	213	192	171	154	141	134	128

The data has been interpolated in the form of a polynomial function.

$$\sigma_{adm} = -1.621 \cdot 10^{-8} \cdot T^4 + 2.020 \cdot 10^{-5} \cdot T^3 - 8.309 \cdot 10^{-3} \cdot T^2 + 9.842 \cdot 10^{-1} \cdot T + 1.922 \cdot 10^2 \quad (3-41)$$

As for the hot header, in which temperatures increase up to 550°C, stainless steel P91 was selected, and the σ_{adm} was set to 134 MPa [48].

Once inner and outer diameter of the pipe are known, the last diameter to be calculated is the external diameter of the coating, that has to guarantee a outer surface temperature of 40 °C. The calculation is done reducing the heat exchange problem in the form of equivalent thermal resistances. The total thermal resistance is obtained as the series of conductive resistance through the pipe wall, conductive resistance through the insulating coating and convective resistance between the external surface of the coating and the environment.

$$R_{tot} = \frac{1}{\pi D_{out,coating} h_{out}} + \frac{\ln\left(\frac{D_{out,coating}}{D_{out,pipe}}\right)}{2\pi k_{coating}} + \frac{\ln\left(\frac{D_{out,pipe}}{D_{in,pipe}}\right)}{2\pi k_{metal}} \quad (3-42)$$

The external film coefficient h_{out} is set to be 10 W/m²-K and includes both convective and radiative heat exchange towards the environment. As for the thermal conductivity of metal and coating, they are set to be respectively 45 W/m-K and 0.1 W/m-K.

The total thermal resistance is a function of the external diameter of the coating. Its value will determine the heat loss towards the environment, which will also depend on the average bulk temperature of the flow and the ambient temperature as indicated in eq. (3-43)

$$\dot{Q}_{loss} = \frac{(T_{ave,flow} - T_{amb}) \cdot L}{R_{tot}} \quad (3-43)$$

In turn, the heat loss will allow the calculation of the external coating temperature:

$$T_{out,coating} = T_{amb} + \frac{\dot{Q}_{loss}}{\pi \cdot D_{out,coating} \cdot h_{out} \cdot L} \quad (3-44)$$

Solving the system constituted by eq (3-42) (3-43) and (3-44), and imposing the desired value of $T_{out,coating}$, both heat loss entity and consequent coating diameter will be determined.

3.2 POWER BLOCK SIMULATION IN THERMOFLEX

Thermoflex is a commercial simulation software with a graphical interface that allows the user to design complex energy systems, taking advantage of a large components library. The software then solves the system energy and mass balance, giving as results detailed information on the components performances and the overall efficiency of the system, as well as the stream thermodynamic state in each point of the system. Components can be independently set to work either in on-design or off-design condition: in the first case the desired thermodynamic performance of the component can be specified; once the component has been dimensioned, it can be switched to work in off design, fixing its geometry and determining its performance as the working conditions change.

In the power block design phase, just a few typologies of component have been used, and are listed below:

- Refrigerant Specification (virtual component)
- Refrigerant Turbine/Compressor
- General Heat Exchanger
- Refrigerant Source/Sink
- Heat Sink

The flow chart of the power block in the case of regenerative double expansion cycle is shown in Fig. 3-17.

The different modes in which components can be set to work, in addition with the definition of simple scripts and control loops, allowed a large freedom in the definition of the power block functioning. A brief description of what the components represent and how they were handled is offered in the paragraph.

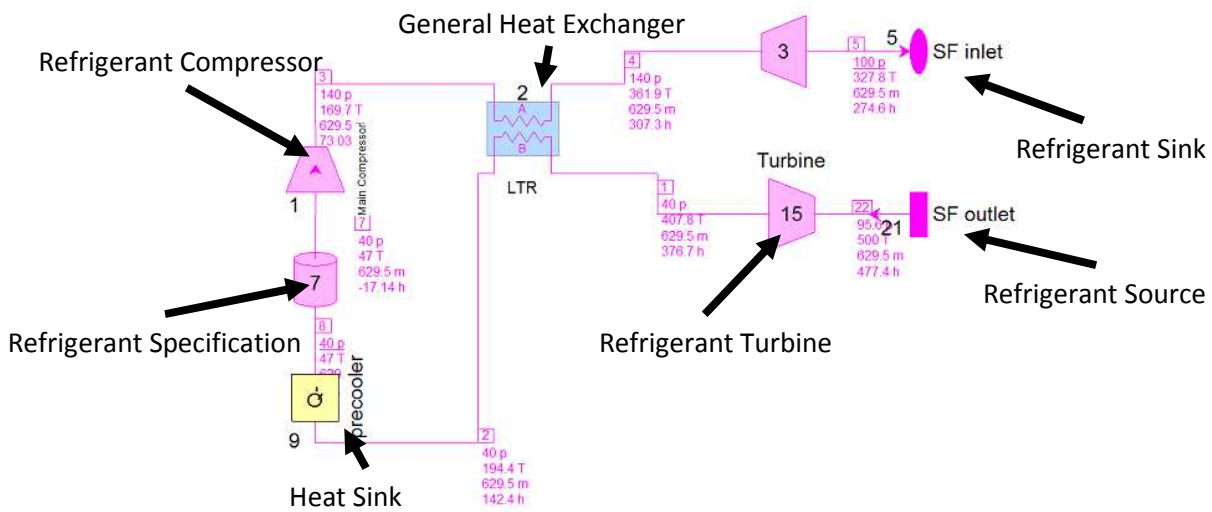


Fig. 3-17 : example of Thermoflex flow chart, showing all the components employed in the power block simulation

Refrigerant Specification: is the virtual component in which the characteristic of the working fluid is set. Carbon dioxide is considered in Thermoflex as a refrigerant (it has a large range of application in cooling systems as coolant). CO₂ properties are calculated when needed according to REFPROP database, available in Thermoflex.

Refrigerant Turbines and Compressors: the Thermodynamic Mode characterization of the turbomachines available in Thermoflex is based on the definition of two parameters: isentropic efficiency and compression/expansion ratio:

$$\eta_{isentropic,compressor} = \frac{\Delta h_{is}}{\Delta h} \quad ; \quad \eta_{isentropic,turbine} = \frac{\Delta h}{\Delta h_{is}}$$

$$\beta_{compressor} = \frac{p_{out}}{p_{in}} \quad ; \quad \beta_{turbine} = \frac{p_{in}}{p_{out}}$$

General Heat Exchangers (HX): multiple options are available in the design of the component, either just selecting the efficacy of the HX, or imposing one or more outlet temperatures. In addition, control loops can be set to have increased control when fixing limits or requirements on the component, in order to guarantee a specific temperatures pinch point, or design UA. The

General HX component was used, with different settings, to simulate the regenerators and the precooler in the power block:

- Regenerators: during the design simulation of the plant, regenerators have been set to work at constant effectiveness. This is a parameter relating the maximum heat that can be transfer from one flow to the other (in the case of an infinite length HX), and the actual heat that is exchanged:

$$\varepsilon_{HX} = \frac{Q_{exchanged}}{Q_{infinite\ length}} \quad (3-45)$$

where $Q_{infinite\ length}$ can be calculated as:

$$Q_{infinite\ length} = \min \left(\dot{m}_{cold} [h_{out} - h(T_{in,hot}; p_{out,cold})]_{cold}; \dot{m}_{hot} [h_{in} - h(T_{in,cold}; p_{out,hot})]_{hot} \right) \quad (3-46)$$

the regenerators effectiveness has been set equal to 90%.

- Precooler: the design simulation of the precooler, even if made using the same component, was complicated by the need to impose both a fixed outlet temperature for the CO₂ side (Compressor Inlet Temperature), and a design pinch point. The heat exchanger was set to maintain the CIT, and the pinch point was fixed with the aid of a control loop, using air mass flow as independent variable to regulate it.

The design simulations of the heat exchangers provides as one of the outputs the UA value. This value will be used in the Excel code once evaluating the off design of a specific plant configuration.

Refrigerant Source/Sink: these components represent the entrance and the exit of the power block, and are the connection points between it and the solar field. Input from the SF solution are set as conditions in the source, whereas the resulting HTF condition at the sink is passed as input to the SF, as explained in the description of the software connection.

Heat sink: as we said, the component was used when a detailed simulation of the precooler was not required or was carried out in an alternative way. When used, this component was simply set to grant a fixed outlet temperature.

3.3 CONNECTION BETWEEN THERMOFLEX AND EES

The independent simulations of the power block and the solar field, had to be interlaced in order to be able to exchange results and, alternatively solving one and feeding its output as input to the other, iteratively converge to the final solution. This interlink was done exploiting a feature that both software offer: to be executed and handled indirectly from Excel.

In the case of Thermoflex the connection with Excel is ELINK. ELINK is an add-in already programmed by the developers of the software, that offers a convenient way of performing parametric studies on Thermoflex files, managing the input parameters through an excel spreadsheet and displaying the output of the simulation either in the traditional way, as a flow chart, or as numerical values in the spreadsheet cells. Starting from a base case (the one already computed in the linked file), it is possible to set an arbitrary number of cases that differ in the inputs set. Visual Basic commands are available to launch the computation of a specific case or of a cases range, making it possible to integrate the power block solution in the macro supervising to the plant simulation.

More complicated is connecting EES with Excel. No add-in is currently available to attend to this task, so an interprocess communication method called Dynamic Data Exchange (DDE) had to be programmed in Visual Basic. The method establishes a communication channel between two different processes, allowing instructions to be sent from one to the other.

The VB code written opens EES at the beginning of the computation, loading the .ees file that has to be used in the simulation: once that the file has been loaded, input data is copied from the spreadsheet where the results of the Thermoflex computation are available to the clipboard, and pasted in a lookup table in the .ees file. The program will read the values and assign them to the appropriate variables. At the end of the computation, the table containing the

results of the solar field solution is again copied and pasted back to the Excel spreadsheet, where it can be read by ELINK and provided to Thermoflex for the following iteration.

The iteration process has to be stopped at a certain point, by establishing a convergence criterion. In our case, a relative tolerance on the difference between the outputs provided by a software and the inputs used in the previous iteration by the other was set. Once this tolerance is satisfied for each one of the variables (that is for the inlet and outlet temperatures, pressures and mass flows at the connection points), the computation is stopped and the simulation is considered converged.

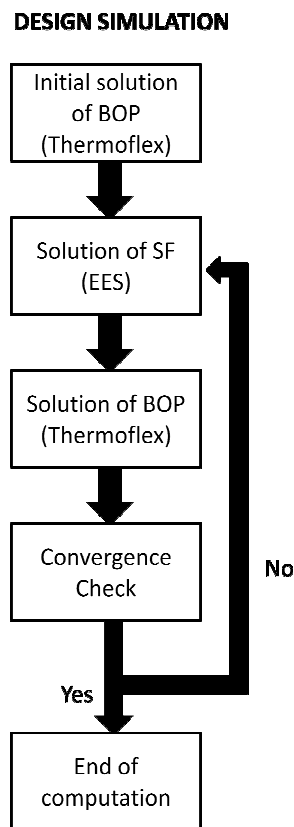


Fig. 3-18: design simulation flow chart

As it will be seen, during the off design simulation the power block was computed directly in Excel, simplifying the interaction with the solutions of

solar field, but losing the flexibility offered by the exposed methodology: a specific code had to be written in VBA for each cycle configuration considered. The opportunity to make use of a commercial software as Thermoflex presents the advantage of delegating the solution of the set of equation describing all the power block components, allowing the modeling of complex cycles layout. Moreover, the parametric solution handling that ELINK offers is perfect to carry out an optimization study like the one we intend to solve for the plant configuration design.

Some results also have to be exchanged between different .ees files: that is the case of design and off design simulation for an already dimensioned solar field. The information that needs to be passed is the values of diameters for the piping and the number of rows in the field. These data were saved in a .txt file at the end of each iteration during the design simulation. At the beginning of the off-design simulation then, the user has to select the .txt file in which the results have been saved: in this way the code will load all information regarding the SF intended to be used in the computation. Fig. 3-18 shows the flowcharts representing the computation logic in the design case.

The solution of the solar field is the process that occupies most part of the simulation time. Moreover, the changes in the inputs are normally very small, during the iterations to converge to the plant solution. A way to speed up the computation is to update the results every time EES converges: this way, when computing the following iteration, EES will consider the values calculated earlier as initial guess values, significantly reducing the time required to converge to the new solution

4 THERMODYNAMIC ANALYSIS OF CYCLE CONFIGURATIONS

A preliminary performance assessment was carried out on the potential configurations to be adopted for the thermodynamic cycle of the power plant. Among all the options investigated, the ones yielding the best results in terms of cycle efficiency have then been studied more in detail, introducing an off design description of components, and characterizing the plant performance not only in the design conditions, but also varying the DNI, thus obtaining a daily (and subsequently annual) performance profile. In order to limit the total computational time of the study, which covers an extremely large number of cases exploring a wide spectrum of operative parameters combinations, during this preliminary phase the following assumptions have been made:

- in all cases, the size of the SF was adjusted, accordingly with its inlet temperature, in order to guarantee a fix thermal input in the HTF, equal to 127 MW_{th}
- the nominal DNI value was set to be equal to $889,1 \frac{\text{W}}{\text{m}^2}$
- isentropic efficiencies of compressors and turbines are considered constant, and have been set respectively to $\eta_{compr} = 0.80$; $\eta_{turb} = 0.85$
- pressure losses were only considered in the SF, and were neglected in the heat exchangers
- regenerators assume a constant effectiveness equal to $\varepsilon = 90\%$
- the air side of the precooler is not computed, and it simply provides the desired Compressor Inlet Temperature (CIT)
- the minimum temperature of the cycle, that is the outlet temperature of the precooler, is set at 47°C .

Both SF thermal input and nominal DNI were set to be equal with the assumptions made in [30]. The high value assumed for the minimum temperature of the cycle, which limits the exploitation of the real gas effects discussed in chapter 2, is due to the choice of the location. As already mentioned, suitable sites for CSP technology are situated at low latitudes, where the ambient temperature remains high throughout the whole year.

Being that the heat rejection is performed using air as coolant, its temperature will limit how much the CO₂ can be cooled down in the precooler. Ambient temperature is assumed to be 32°C for the whole year.

A wide range of operative parameters has been explored: maximum temperature, maximum and minimum pressures, and eventually intermediate pressure levels or flow split ratios. Some limitations had to be considered, for maximum temperature and pressure: the mechanical resistance of the collectors has to be guaranteed. Based on the technical data provided by the collectors manufacturer [25] and on the resistance analysis carried out by Lambrughini and Serafini in their work [31], these limits were set to be 550°C for the maximum temperature and 100 bars for the maximum pressure seen by the collectors (that is, at the inlet of the SF). Higher and lower values of T_{max} and p_{max} were investigated as well, to understand the effect of these parameters on the performance of the cycles. An exergy analysis was finally carried out for each one of the cases, to identify the main sources of loss and understand where there can be a margin for improvement. The results obtained for each configuration studied are reported in the next paragraphs

4.1 SIMPLE REGENERATIVE CYCLE

This is the simplest configuration studied. It is based on a regenerator which allows the recovery of heat from the hot gases exiting the turbine, heating up the HTF at the high pressure side, before it enters the solar field. The cycle layout and T-s diagram are shown in Fig. 4-1.

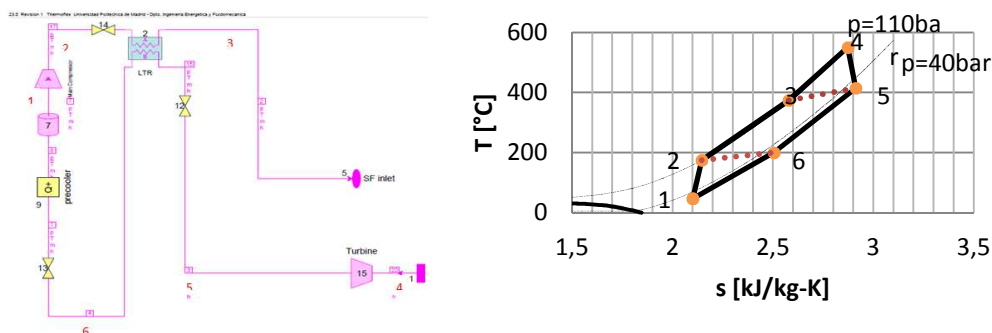


Fig. 4-1 : simple cycle T-s diagram and PB scheme

Fixing maximum temperature (outlet of the SF, point 4) and pressure (outlet of compressor, point 2), the performance of the cycle can be mapped varying the minimum pressure, or equivalently the pressure ratio β . Three values and respective combinations of maximum pressure and temperature were investigated, according to the exposed methodology. An example of the obtained result is shown in Fig. 4-2.

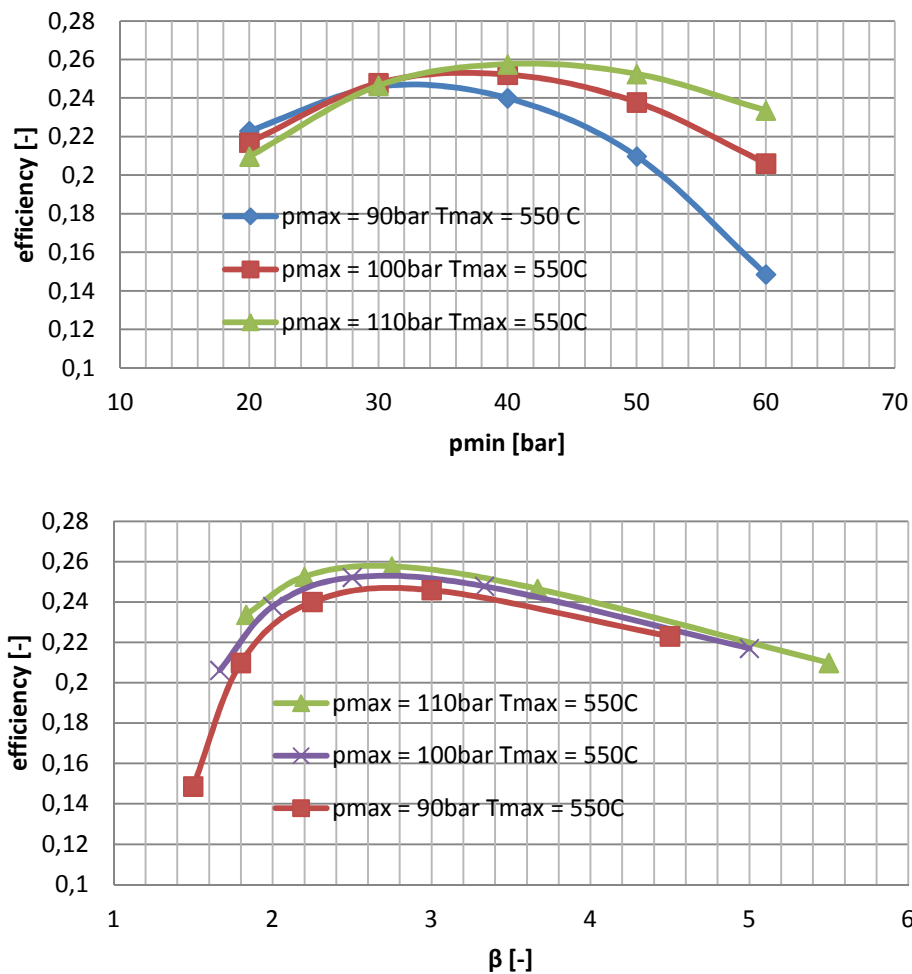


Fig. 4-2 : cycle efficiency as a function of p_{min} and β (T_{max} and p_{max} fixed)

It can be seen how for a certain value of p_{max} , an optimum value of p_{min} (inlet pressure in the compressor) yielding the maximum cycle efficiency can be identified. This value increases with p_{max} , maintaining the optimum beta close

to a constant value. The increase in p_{\max} also has a positive effect on the overall cycle efficiency.

Analogous results were obtained for the other two values of T_{\max} . An increase in the maximum temperature of the cycle always has the effect of increasing its efficiency, in agreement with what expected from Carnot's law. The efficiency curves at different T_{\max} are then simply moved to higher or lower values of η according to a higher or lower value of T_{\max} , but maintain the same trend as function of p_{\max} and p_{\min} . The corresponding graphs are not reported for sake of brevity.

It can be seen how, due to the limitation in maximum pressure, we do not observe an increase in efficiency when the p_{\min} approaches the critical value for CO_2 . One would expect this result because, in the region close to the critical point, CO_2 starts to behave strongly as a real gas. This implies a large increase in its density, and thus a major reduction in compression work, with the consequent positive effect on the cycle net work output. But the fact that the maximum pressure of the cycle is bounded to relatively low values by the limit imposed to ensure the mechanical integrity of the collectors, does not allow the full exploitation of this effect. Only at very low beta, when the efficiency is already drastically reducing, we can get to minimum pressure values close enough to the critical pressure. Increasing the maximum pressure of the cycle allows us to attain higher cycle β maintaining the minimum pressure close to the critical value, and it can be seen how this has a major positive impact on the cycle efficiency.

4.2 REGENERATIVE RECOMPRESSION CYCLE

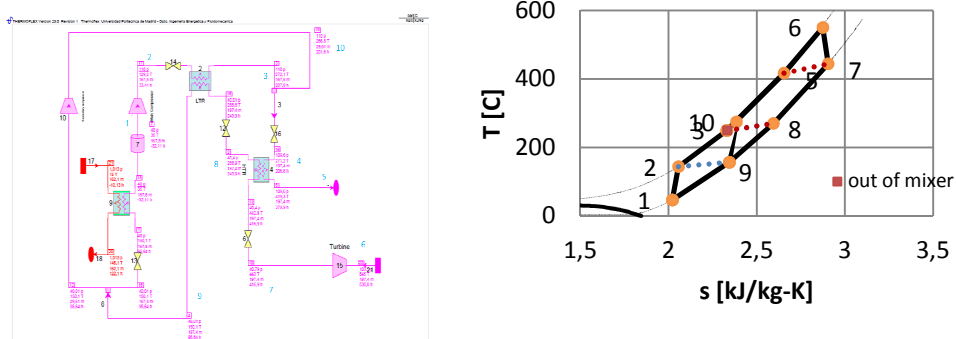


Fig. 4-3 : recompression cycle T-s diagram and PB scheme

The cycle scheme is shown in Fig. 4-3. In the recompression cycle, a fraction of the flow is spitted before the pre-cooler, and is directly recompressed in an auxiliary compressor. The main flow proceeds to be cooled down, and it is then compressed as well and heated up in a first regenerator (LTR, Low Temperature Regenerator). Then, the two flows are mixed again, and a second regeneration step is performed (HTR, High Temperature Regenerator), before entering the SF. The intention of this procedure is twofold: first of all, to reduce the amount of heat discharged in the pre-cooler; secondly, to balance the heat capacity of the two streams in the LTR. The latter becomes necessary when, due to a modification in the HTF behavior induced by the proximity to the critical point, the heat capacity of the same fluid is very different on the two sides of the regenerator. To characterize how much of the main flow is deviated to the secondary compression, the split factor parameter is defined, as:

$$\alpha = \frac{\dot{m}_{deviated}}{\dot{m}_{total}} \quad (4-1)$$

This configuration has been intensively studied in the case of nuclear power plants, because it manages to guarantee high efficiency at low maximum temperatures. To achieve this result the main compression is normally performed right above the critical point, and this causes the CO₂ to manifest a strong change in its specific heat in the high pressure / low temperature side of the LTR, as the flow is heated up. Because of this difference in the heat capacity of the two streams, even if the pinch point is maintained at low values, the average temperature difference is going to be very high. Thus, the exigency of

modulating the heat capacity of one of the streams in order to move closer the two temperature profiles, and reduce the irreversibility associated with the heat exchange.

Normally, the optimal value for the split factor in nuclear sCO₂ Brayton cycles is around 20-30% [47]. However, as it can be seen from Fig. 4-4, this is not the case in our plant.

The introduction of a flow split, represented by the increasing split factor, does not have a positive effect on the efficiency, which is always decreasing as the split becomes larger. The maximum efficiency is achieved at split factor zero, which corresponds to the case of simple regenerative cycle. The higher value of efficiencies with respect to what seen in the previous paragraph are then just due to the fact that instead of one regenerator here we have two, both with an effectiveness of 90%. A higher degree of heat recovery is then achieved, explaining the gain in cycle performance.

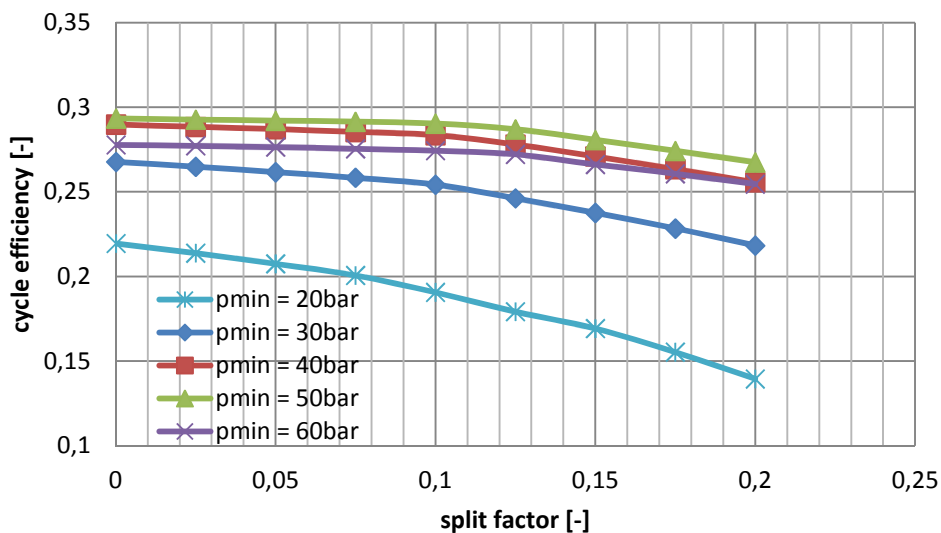


Fig. 4-4: recompression cycle efficiency as function of split factor for different minimum pressures (Tmax=550C pmax=100bar)

The reason why recompression does not improve the cycle efficiency (differently from what observed in the nuclear power plants) lies in the fact

that the need for a split comes up only when the LTR is largely unbalanced. This happens when we are compressing close to the critical conditions, and when the pressure ratio of the cycle is high, so that the two currents in the heat exchangers manifest a radically different nature. In our case though, because of the limitation in maximum pressure and quite high minimum temperature, the LTR is normally quite balanced, as can be seen from Fig. 4-5, which compares the T-Q diagram of the LTR when p_{\min} is close to the critical value and when it is not: it can be seen how when p_{\min} is equal to 70 bars an evident change in the LP stream heat capacity occurs as the fluid is heated up. The change though is not strong enough to drastically increase the temperature difference between the two flows, compared to the case at lower p_{\min} . Introducing a flow split helps to improve the quality of the regeneration, but the achievable irreversibility reduction is limited, as shown in Fig. 4-6, where the exergy efficiency of the LTR is plotted against the split factor.

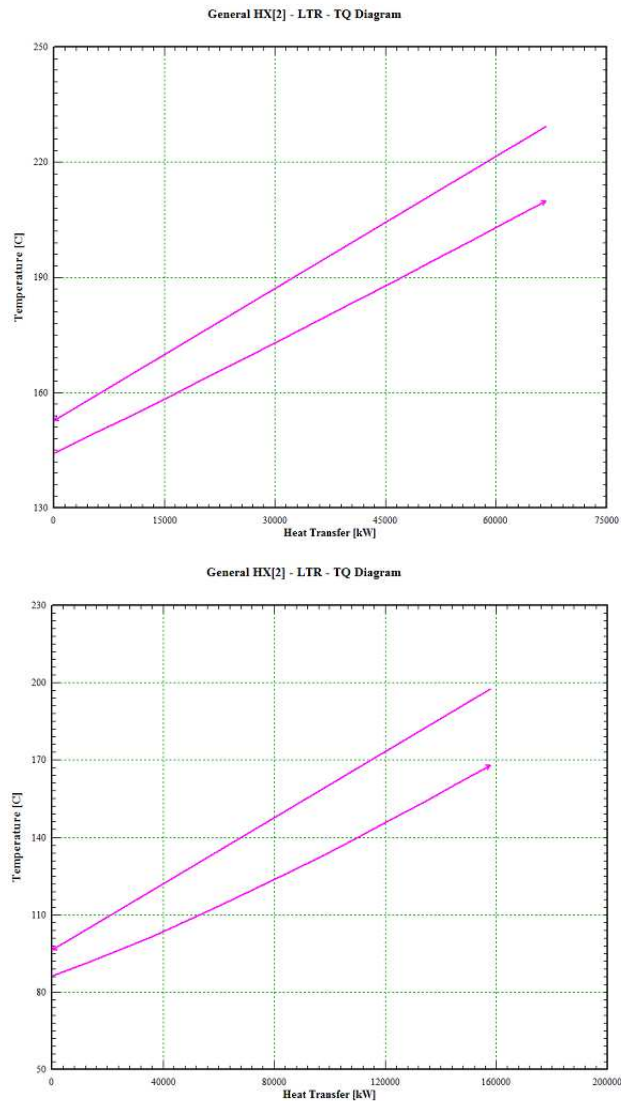


Fig. 4-5: regenerator T-Q diagrams ($p_{\min}=30$ bars case above, $p_{\min}=70$ bars case below)

It can be noted that, increasing the spitted fraction, the efficiency grows up to a maximum and then it decreases again. The maximum corresponds to the optimal balancing of the HX: passed that point, the pinch point will occur on the other side of the HX (LP exit), and further decreasing the heat capacity of the LP side stream will have a negative effect on the quality of the heat exchange.

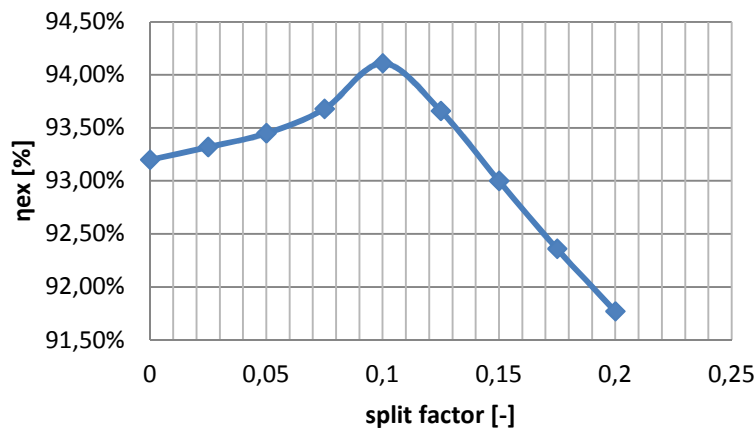


Fig. 4-6 : LTR exergy efficiency as a function of split factor
 ($p_{max}=110\text{bar}$; $p_{min}=40\text{bar}$; $T_{max}=550^{\circ}\text{C}$)

The overall effect of a flow split then is mainly a large increase in the compression power, as the inlet conditions in the auxiliary compressor are much less favorable, since the HTF temperature is higher and the isobars in the T-s diagram diverge (maintaining the pressure ratio constant, a higher T_{in} implies a higher compression work).

Furthermore, another negative effect on the cycle is detected as the split ratio increases: instead of decreasing, the heat rejected in the precooler increases. This effect is due to the higher inlet temperature of the flow entering the precooler, which overcomes the reduction in mass flow. The reason for the temperature increase is twofold. Firstly, in the HTR the hot LP stream sees a flow on the HP side at a higher inlet temperature. This is due to the increased fraction of flow that is directly recompressed, not participating in the heat rejection, and that rejoins the main flow at a high temperature, increasing in the mixing process the temperature of the total flow that is entering the HTR on the high pressure side. The low pressure stream is consequently cooled off less, and thus enters the LTR at a higher temperature. Secondly, also the decrease in mass flow on the HP LTR side contributes to a reduced (even if better performed) heat recovery from the hot gas. In turn, this causes a greater amount of energy to be discharged in the precooler.

The combination of these two effects explains the efficiency trend, and indicates that recompression is not favorable under our operating conditions.

4.3 REGENERATIVE DOUBLE EXPANSION CYCLE

In this configuration, the expansion is performed in two separate turbines: one positioned before the SF, and one right after it. This way, it is possible to relax the constraint of the cycle maximum pressure, since the pressure seen by the collectors is the intermediate level after the first expansion. The heat injection before entering the first turbine is granted by the regeneration process, during which the heat contained in the gas exiting the second turbine is exploited to heat the stream coming from the compressor up to the first turbine inlet temperature. This implies a lower TIT for the first turbine.

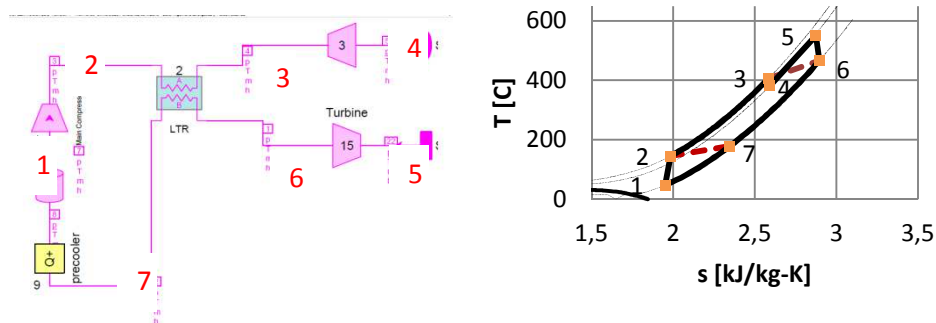


Fig. 4-7 : double expansion regenerative cycle T-s diagram and PB scheme

However, the intention is to take advantage of the reduction in compression work caused by the real gas behavior, and see whether the first expansion, even if strongly penalized by the low TIT, can provide a net output sufficient to outbalance the additional compressor consumption due to the higher beta. As in the other cases, the analysis covered a wide range of p_{max} , p_{min} and T_{max} . Furthermore, the intermediate level of expansion had to be set: that is, the outlet pressure of the first turbine and the maximum pressure in the solar field, and thus it has to respect the mechanical constraint.

Fig. 4-8 shows the results for the case of intermediate pressure equal to 100 bar. It can be seen how the temperature (as already discussed) moves the curves at higher values of efficiency, without changing substantially the dependence on the pressure. It is interesting to notice that the highest value of efficiency at low p_{min} values are obtained with the lowest p_{max} , implying that in

this region, where the real gas effect is not that strong, to increase the beta of the compression does not lead to any advantage in terms of work output from the first turbine. On the other hand, when the compressor inlet pressure approaches the critical values, higher maximum pressures yield higher efficiencies.

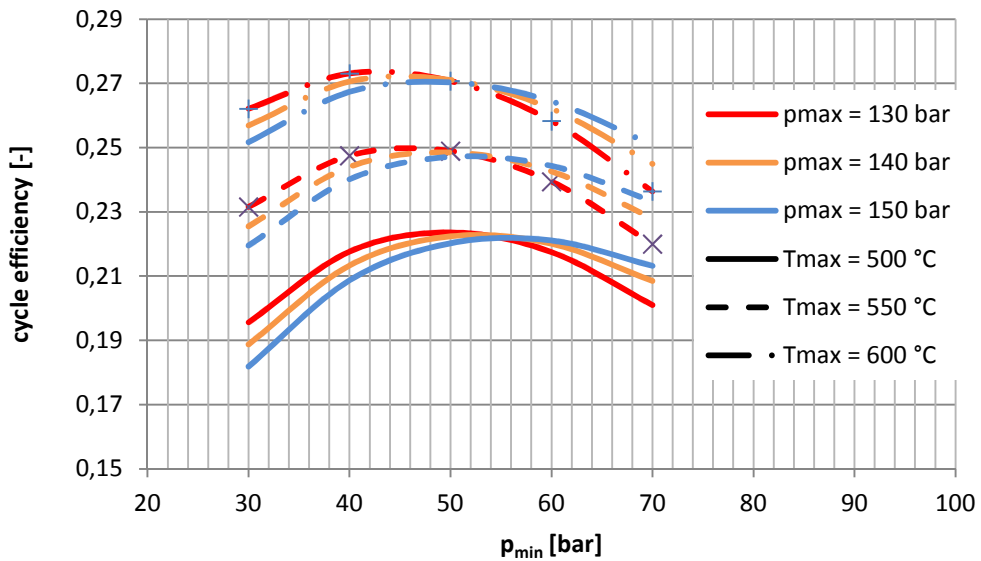


Fig. 4-8 : double expansion cycle efficiency as a function of p_{min} for different combinations of p_{max} and T_{max} (intermediate pressure=100bar)

The optimum p_{min} remains in the region of low pressures, still quite far from the critical value. Furthermore, the maximum efficiency value is very close to the one obtained in the case of the simple regenerative cycle.

Performing the exergy analysis of the cycle, we can get some insight on the causes of inefficiency. In Fig. 4-9 the result of the exergy analysis performed on the cycle maintaining the maximum and intermediate pressure and increasing the minimum pressure are summarized. It can be seen how the efficiency has a maximum in between the maximum and minimum values of p_{min} , and how even if the two extreme points share the same exergy efficiency, but the causes of irreversibility are completely different.

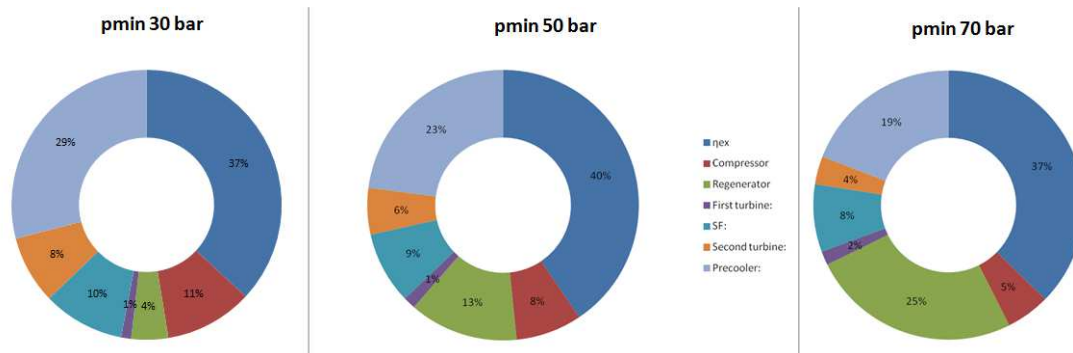


Fig. 4-9 : exergy analysis comparison between double expansion cycles at different p_{min}

As the minimum pressure increases, the irreversibility connected to the compression decreases, due to the decrease in the compression ratio and to the real gas effect affecting the HTF. A lower temperature at the compressor exit, also reduces the exit temperature of the LP side of the regenerator, and thus the quality of heat discharged in the precooler, as can be seen by the reduction in exergy destruction that takes place in that component. What increases substantially towards higher p_{min} is the irreversibility in the regenerator: the entity of the heat recovery is largely amplified by the fact that, while the exit temperature from the second turbine increases, the outlet temperature of the compressor reduces. Furthermore, the real gas behavior starts to affect the HTF at higher p_{min} , increasing the temperature differences under which the heat exchange takes place. To summarize, this last irreversibility becomes dominant, and explains why the efficiency starts to go down again. The two T-Q graphs in the case of $p_{min} = 30 \text{ bars}$ and $p_{min} = 70 \text{ bars}$ are shown in Fig. 4-10, and it is possible to observe how the temperature difference between the two flows at the exit of the cold side in the second case is higher of about 20-30 °C.

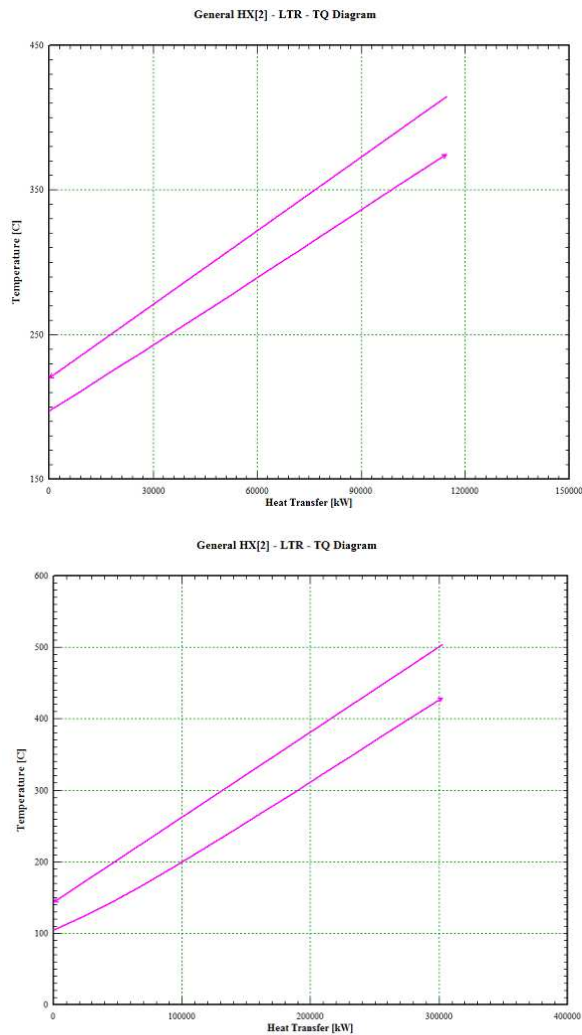


Fig. 4-10 : regenerator T-Q diagrams ($p_{min}=30\text{bar}$ case on the left, $p_{min}=70\text{bar}$ case on the right)

If we compare the performances of the regenerative double expansion cycle and regenerative simple cycle, we can see how, considering the mechanical constraints, the maximum obtainable efficiencies are extremely close. This would seem to indicate that the double expansion is not a considerable performance booster in our situation, and thus it won't be further considered.

4.4 REGENERATIVE RECOMPRESSION DOUBLE EXPANSION CYCLE

A possible way to mitigate the irreversibility observed in the regenerator in the double expansion cycle (main cause of irreversibility at high p_{min}), is to integrate it with the recompression. In this way, the benefits deriving from the CO₂ real gas behavior without being penalized by the regeneration process can be better exploited.

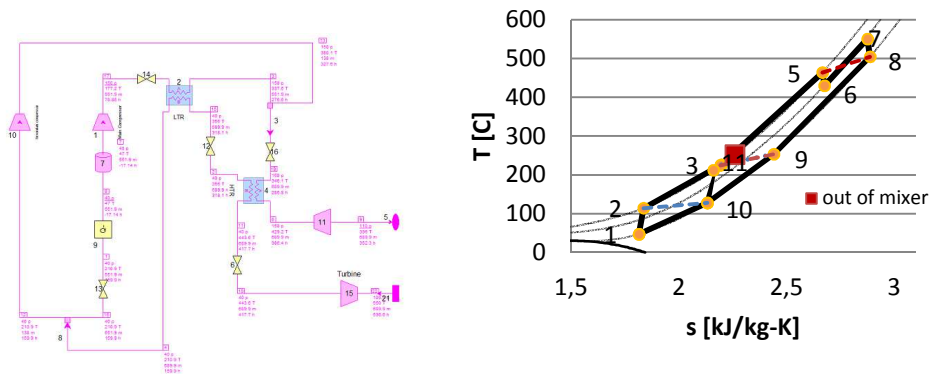


Fig. 4-11 : recompression double expansion regenerative cycle T-s diagram and PB scheme

The results calculated by the simulations are summarized in Fig. 4-12. The performance once again is evaluated at different split factors.

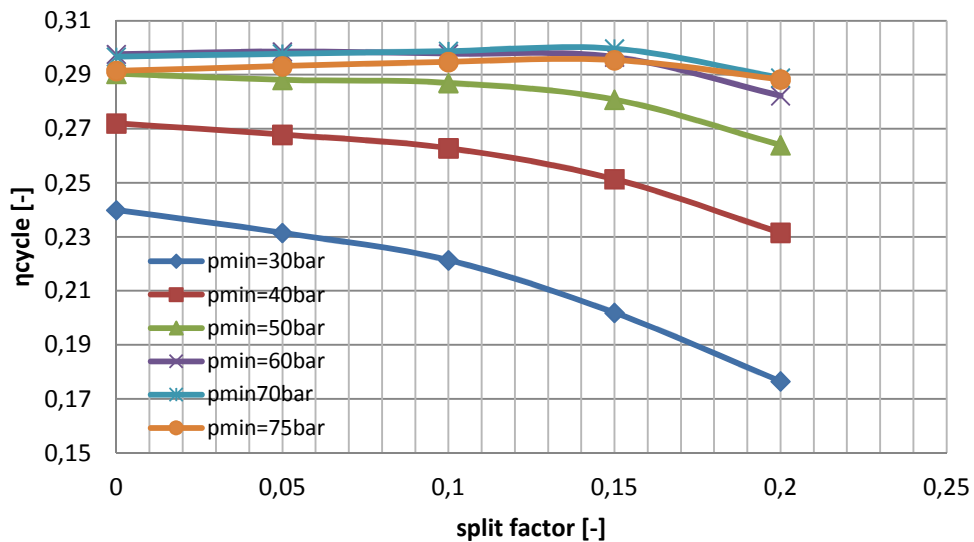


Fig. 4-12 : recompression double expansion cycle efficiency as function of split factor, for different minimum pressures ($p_{max}=150bar$; $T_{max}=550C$)

As a matter of fact, the introduction of the recompression does not have an evident positive impact on the efficiency. Differently from what seen for the pure recompression, for minimum pressures close to the critical value we do not observe a performance consistently decreasing as the split factor increases, but it is constant until it finally decreases at high split fractions. Comparing once again the exergy analysis evolution as the study parameter changes, we can understand how the causes of irreversibility readjust in the various cases.

The net effect of an increased flow split on the regeneration process is positive up to a certain value of split factor. After that point, for the same reasons explained in the discussion of the recompression configuration, the regenerator exergy efficiency starts to decrease: further lowering the thermal capacity of the HP side unbalances the heat exchanger. This (minor) positive effect is though compensated by two increasing irreversibilities. First of all, as we increase the secondary flow, an exergy destruction is introduced in the auxiliary compressor (that, as already discussed, behaves much more inefficiently than the main compressor). Secondly, as already observed, the heat rejection in the precooler goes up, even if the mass flow is being reduced. This as a consequence of the increased exit temperature of the LP stream in the LTR.

Even if the recompression is proved to be unsuitable for this application, it is interesting to compare the efficiency results at split factor zero with the results obtained in the previous paragraph for the regenerative double expansion cycle. If we get rid of the flow split, the two plant configurations are identical, with the exception that in this case we have two regenerators, whereas previously we had just one. Being that the efficacy is fixed to 90%, this in turn means a better degree of regeneration, under lower temperature differences.

In Fig. 4-13 it can be seen how the peak in efficiency, once the irreversibility occurring during the regeneration is mitigated, shifts to higher minimum pressure, and to substantially higher values.

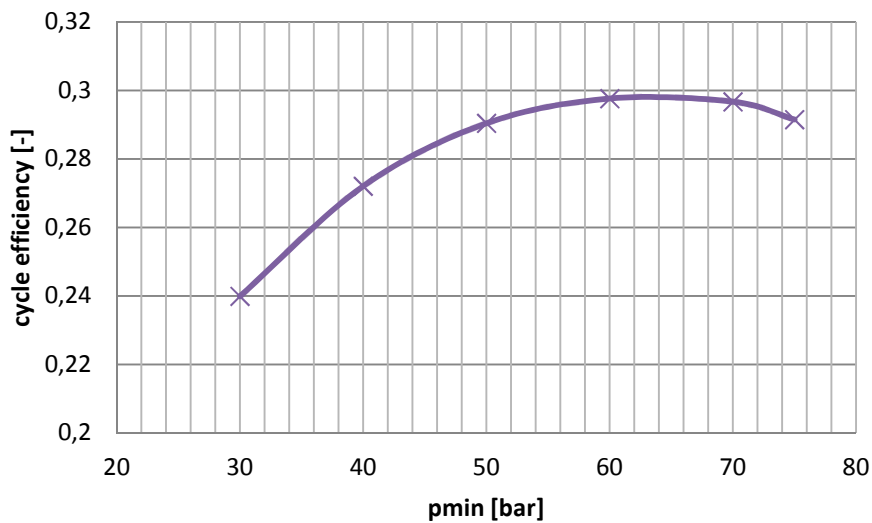


Fig. 4-13 : envelope of split factor 0 points from curves in Fig. 4-12 : recompression double expansion cycle efficiency as function of split factor, for different minimum pressures (pmax=150bar; Tmax=550C)

The reason why splitting the regeneration in two separate heat exchangers has such a strong influence on the overall performance becomes evident once we observe the detail of the T-Q diagrams in the LTR and HTR (Fig. 4-14). It can be seen how, even if the mass flow in both sides of the heat exchangers is the same in the two cases, the heat capacity of the HP side noticeably changes during the heating, as observed in the previous paragraphs. The majority of the heat exchange though takes place in the HTR under a pretty much constant temperature difference, as when the LP stream reaches a sufficiently high temperature, it starts behaving again like an idea gas, maintaining a constant specific heat. If at the end of the first part of the exchange (that is at the exit of the LTR), this temperature difference is much lower than in the case of a single HX, then the benefit will affect the whole HTR.

In conclusion, the introduction of the recompression circuit is proved to be ineffective, but an investment in a better regeneration system seems to be more advisable.

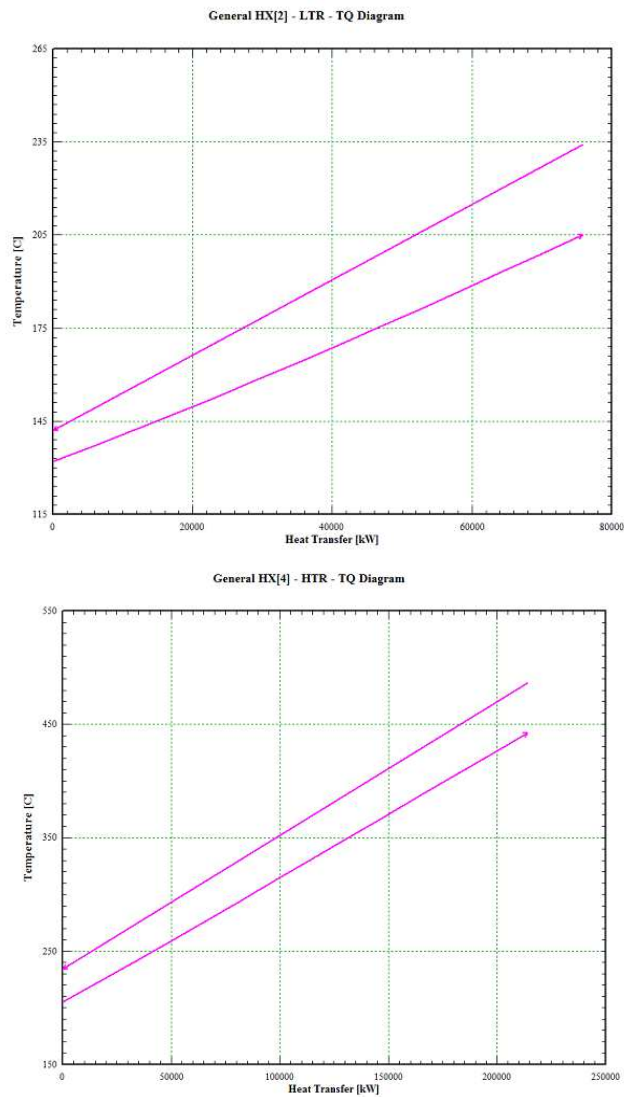


Fig. 4-14 : LTR (above) and HTR (below) T-Q diagrams (pmin=70bar; pint=110bar; pmax=140bar; Tmax=550C)

4.5 REGENERATIVE INTERREFRIGERATED CYCLE

With the introduction of the interrefrigeration, the compression process is split in two phases, and a second heat exchanger cools down to the minimum temperature the CO₂ after a first intermediate compression. This is normally done in Brayton cycles to reduce compression work and increase specific work

of the cycle: a colder fluid has a higher density, and thus requires less power to be compressed. Furthermore, in this case the effect will be enhanced by the proximity to Andrew's saturation curve. An image of the cycle T-s is presented in Fig. 4-15. The total enthalpy rise associated with the compression has been equally divided between the two compressors.

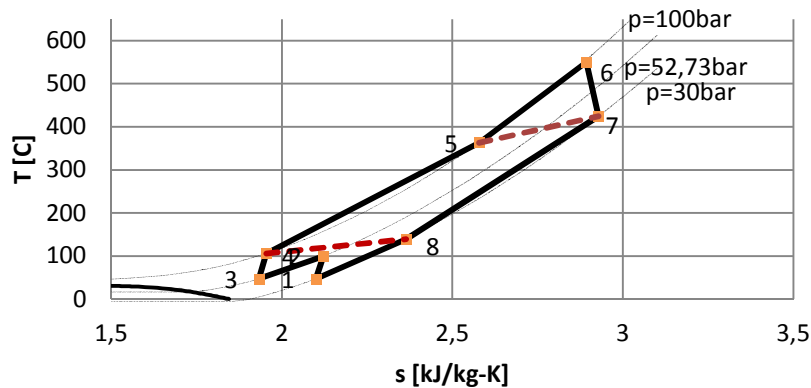


Fig. 4-15 : regenerative interrefrigerated cycle T-s diagram

The usual performance analysis is conducted, exploring various combinations of T_{max} , p_{max} and p_{min} . Fig. 4-16 shows the supremacy of the interrefrigerated cycle performance of the with respect to the simple cycle, once the thermodynamic constraints imposed by the collectors are respected ($p_{max}=100$, $T_{max}=550^{\circ}\text{C}$). The optimum value of p_{min} moves to lower pressures, or equivalently higher β , reflecting the substantial reduction in compression work of the intercooling. As one would expect, when beta reduces intercooling is not decisive, as the compression work is already very low, and the performance of the two cycles becomes very close.

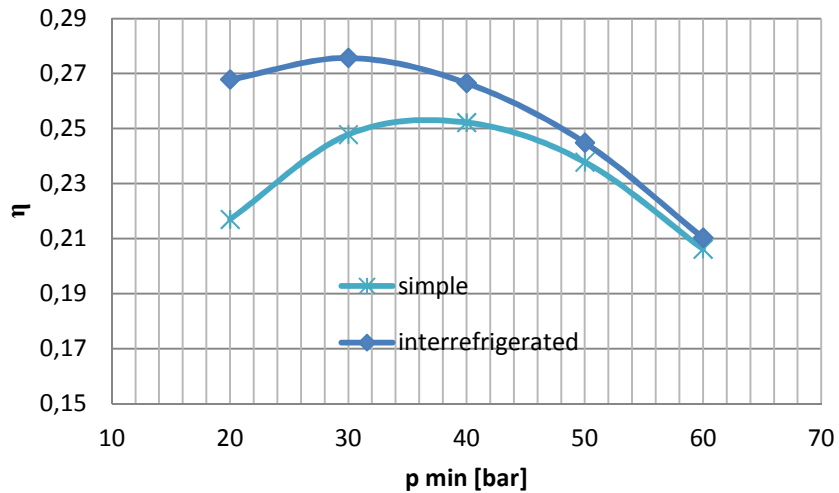


Fig. 4-16 : interrefrigerated vs. simple cycle performance comparison

Comparing the exergy analysis of the two cases at the same minimum pressure ($p_{min}=40\text{bars}$), it can be seen of the different irreversibility. While in the simple cycle most of the performance loss is connected to the heat rejection, when interrefrigeration is introduced the critical component becomes the regenerator. Once again the cause is the real gas effect in the first part of the heat exchange (due to the lower inlet temperature of the cold stream), which increases the average temperature difference between the two flows.

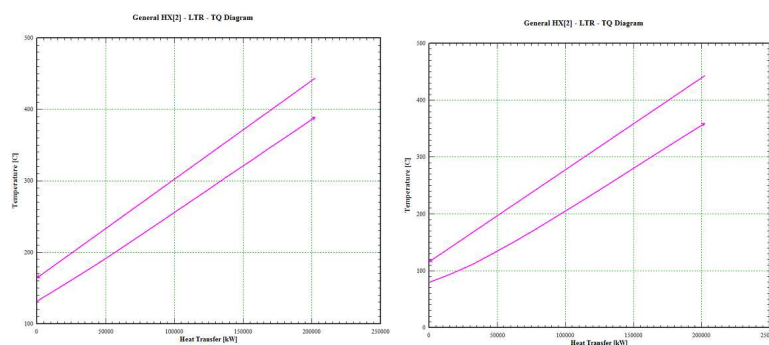


Fig. 4-17 : regenerator T-Q diagram comparison (simple cycle on the right, intercooled cycle on the left)

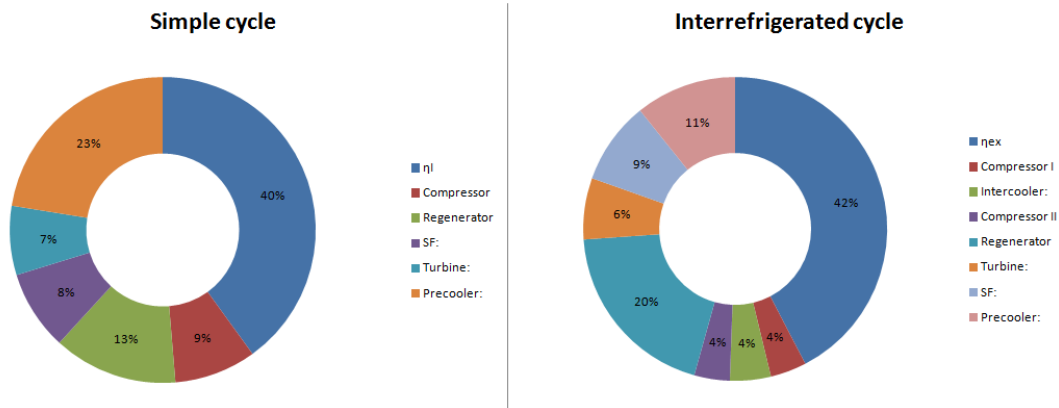


Fig. 4-18 : exergy analysis comparison between simple and intercooled cycles

Another point is that the interrefrigeration does not greatly reduce the overall irreversibility generation due to the compression process: this positive effect is limited (9% total efficiency loss in simple cycle, versus a 8% in intercooled). On the other hand, it has a major impact on the heat rejection process: the lower outlet temperature from the second compressor, causes a reduction of about 50°C in the precooler inlet temperature. Both precooling and interrefrigeration are thus performed on fluxes at low temperatures, leading to smaller total exergy destruction (23% in simple cycle, 15% in intercooled); in turn, this is the main efficiency gain induced by intercooling. At lower beta both the advantages in compression and heat rejection become less significant, and the unbalance induced in the regenerator prevails, explaining the similar performance achieved by simple cycle.

4.6 INTERREFRIGERATED DOUBLE EXPANSION

The addition of intercooling in the double expansion regenerative cycle strongly penalizes its performance. Fig. 4-19 shows the efficiency as a function of p_{min} in the two cases. When the beta of the cycle is very high the positive effect of intercooling on the compression specific work compensates the reduction in work output from the first turbine, caused by the lower inlet temperature induced by the intercooling. As the minimum pressure increases though, the negative effect on the TIT dominates, and the performance of the cycle drastically decreases.

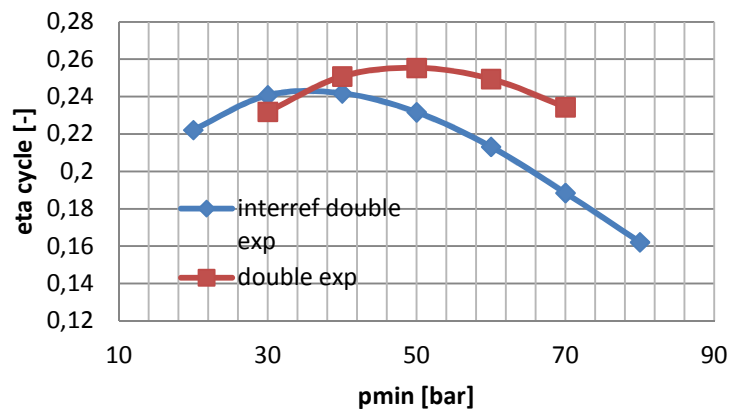


Fig. 4-19 : effect of Intercooling addition to double expansion cycle ($T_{max}=550C$; $p_{max}=135bar$)

The combination of unbalancing in the regenerator and reduction in the first turbine TIT as well as SF inlet temperature leads to unsatisfactory results for the combination of intercooling and double expansion.

4.7 INTERREFRIGERATED RECOMPRESSION

In order to moderate the performance loss consequence of the unbalancing in the regenerator when the compression is intercooled, the flow split exposed in the recompression cycles can be introduced. This way, the average temperature difference in the LTR can be minimized through a split factor optimization, and the positive effects of intercooling can be fully exploited. The cycle configuration and T-s diagram in this case are shown in Fig. 4-20.

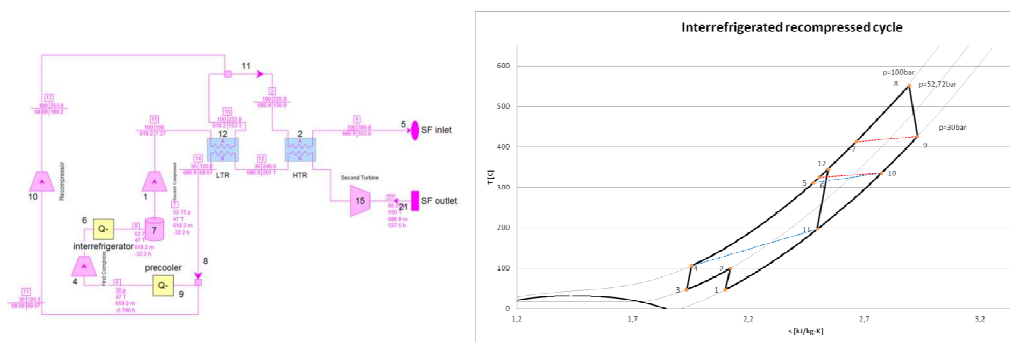


Fig. 4-20 : regenerative interrefrigerated recompressed cycle scheme and T-s diagram

The efficiency, as seen in the case of simple cycle with recompression, is much higher than in the case with just interrefrigeration, but the performance boost does not depend on the flow split: the optimum efficiency is obtained fixing a split between 0 and 10%, but the difference with the split zero case, which in turn is equivalent to interrefrigeration without recompression, is too little to justify the increased cycle complexity.

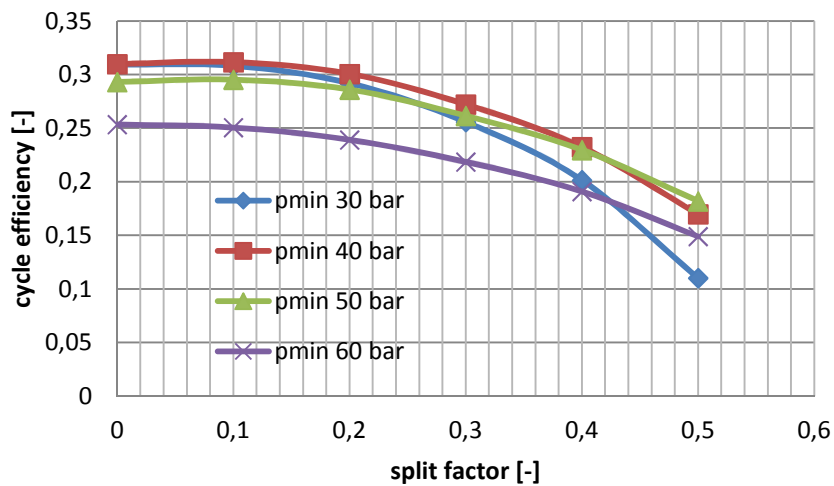


Fig. 4-21 : cycle efficiency as a function of split factor for different pmin values

It appears once again that the best investment is in the regeneration apparatus.

4.8 INTERREFRIGERATED DOUBLE EXPANSION RECOMPRESSION

The last configuration examined is a combination of all the features seen so far. The cycle presents a high degree of complexity, with a total of 5 turbomachines between compressors and turbines. Its performance would have to be drastically better than the others, to justify such a complexity.

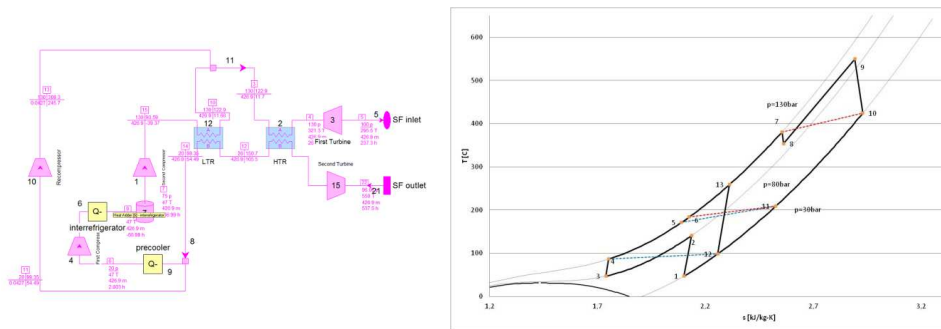


Fig. 4-22 : interrefrigerated double expansion cycle with recompression BOP scheme and T-s diagram

As can be seen from Fig. 4-23 this is not the case. Recompression finally becomes a useful feature, and a clear maximum can be identified for high values of flow split. The value of the maximum though is comparable with what obtained for the simple and interrefrigerated cycles when two heat exchangers are employed in the regeneration.

We can thus conclude that this configuration surely will not be competitive with the others in terms of final cost of electricity and annual performance since additional components imply additional cost and longer start up times.

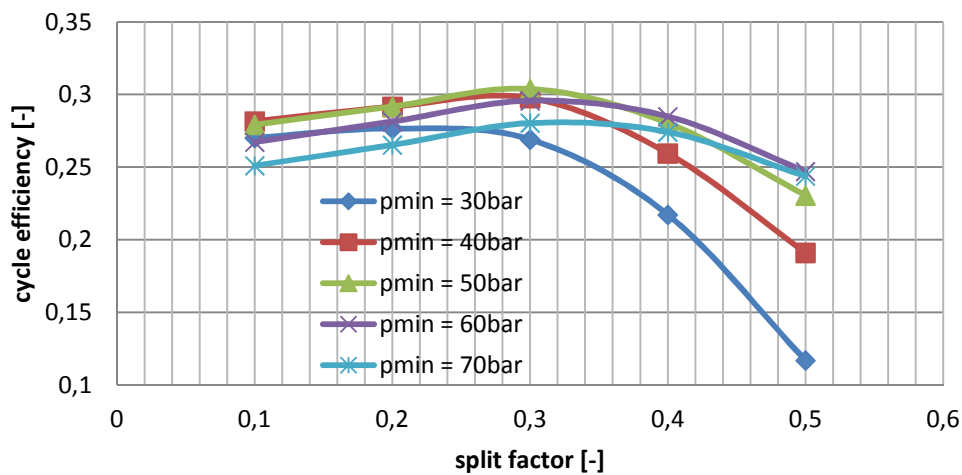


Fig. 4-23 : cycle efficiency as a function of split factor for different pmin values (pmax = 140bar ; Tmax = 550°C)

4.9 UA VALUE EFFECT ON SIMPLE AND INTERREFRIGERATED CYCLES

A difference has been observed in the efficiency value between base configuration and configuration with the addition of the recompression loop at split factor 0, both in the case of simple and interrefrigerated cycles. This is due to the fact that even if effectively the resulting plant scheme is the same, the regeneration process is carried out in the first case in a single regenerator, in the second case in two. Being the effectiveness of heat exchanger fixed, this causes the global UA value allocated to regeneration to be different.

Since the effect of the regenerators UA has a major impact on the performance of the cycles, a parametric study was performed in order to attain a general idea on the trade-off between increasing the surface of the regenerator, thus its cost, and improving the global efficiency of the plant. A complete analysis would have to investigate the combination of the two effects on the final energy cost, taking into account pressure losses in the heat exchangers, and determining the optimal surface of the regenerator by minimizing the LCOE. Since our analysis does not cover the economical aspect of the energy production though, the final UA selected to proceed with the off-design simulations was determined by setting a new value of nominal efficacy that ensures a reasonable performance improvement limiting at the same time the UA to values close to what observed in the case of the complex plant configurations studied in this chapter.

Fig. 4-24 : simple cycle efficiency as a function of regenerator UA ($p_{\max}=100\text{bar}$; $T_{\max}=550^{\circ}\text{C}$; $p_{\min}=30\text{bar}$) and Fig. 4-25 : intercooled cycle efficiency as a function of regenerator UA ($p_{\max}=100\text{bar}$; $T_{\max}=550^{\circ}\text{C}$; $p_{\min}=30\text{bar}$) show the values of cycle efficiency in the case of respectively simple and interrefrigerated cycles, as a function of the effective UA value of the regenerator. As a comparison, both the optimal efficiency determined assuming an efficacy of 90%, and the efficiency corresponding to the cycle with the addition of recompression at split 0, are plotted as well.

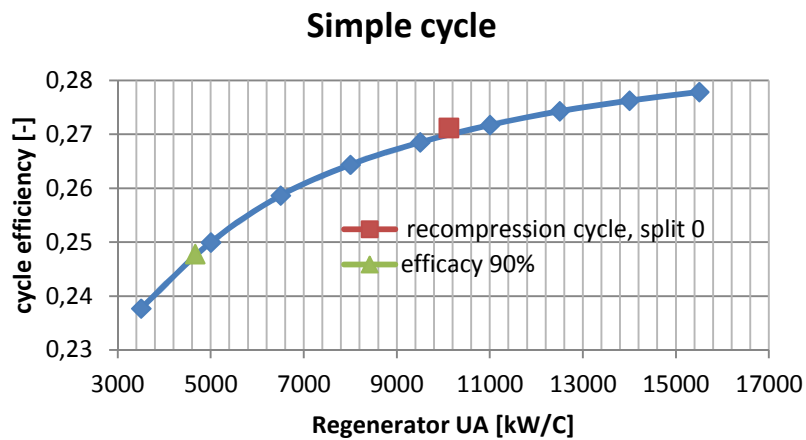


Fig. 4-24 : simple cycle efficiency as a function of regenerator UA ($p_{max}=100\text{bar}$; $T_{max}=550^{\circ}\text{C}$; $p_{min}=30\text{bar}$)

The graphs clearly show how, in both cases, a substantial improvement in the performance can be achieved by increasing the surface of the regenerator, or equivalently the quality of the heat recovery. As expected, the greater efficiency values observed in the recompression cycles are justified by an increase in the effective UA of the regeneration, and the corresponding points lay on the curve. It can also be seen how setting the efficacy to 90% leads to very small final values of UA.

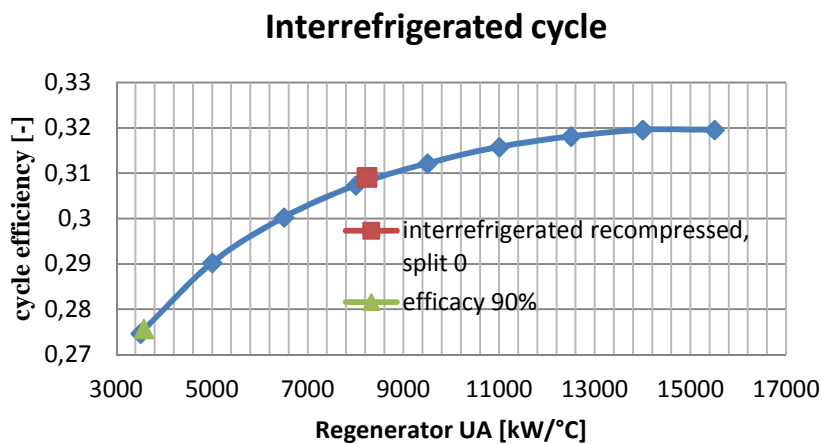


Fig. 4-25 : intercooled cycle efficiency as a function of regenerator UA ($p_{max}=100\text{bar}$; $T_{max}=550^{\circ}\text{C}$; $p_{min}=30\text{bar}$)

The curves also allow us to compare the performance of the two cycle configurations fixing the size of the regenerator. Interrefrigeration always adds three to four points to the efficiency of the cycle. Increasing the UA at first amplify the difference between the two; when its value starts to be very large though, a further increase does not affect the interrefrigerated cycle, whereas the simple cycle still manifests margin for improvement. The efficiency difference then follows a parabolic profile, as it is shown in Fig. 4-26.

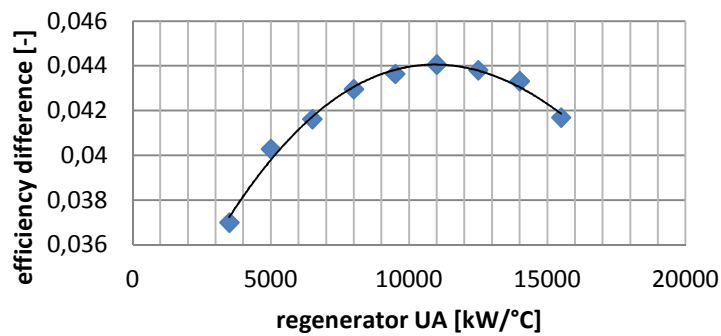


Fig. 4-26: efficiency difference between intercooled and simple cycles as a function of regenerator UA

4.10 CONCLUSIONS

The analysis carried out indicates how interrefrigerated cycle, once the efficacy of the regenerator is increased with respect to the initial value of 90%, can attain a performance over 30%, maintaining a relatively simple cycle scheme with limited number of components. Compared to the simple cycle, the efficiency gain provided by interrefrigeration can reach up to 4.4 percentage points, fixing the size of the regenerator. The additional cost represented by a second compressor then should be balanced by the increased annual production of electricity.

More complicated cycle schemes were investigated as well showing limited increase in efficiency compared to simple and interrefrigerated cycles, because of the mechanical constraints for the values of maximum pressure and temperature,. A summary of the obtained results is shown in Fig. 4-27.

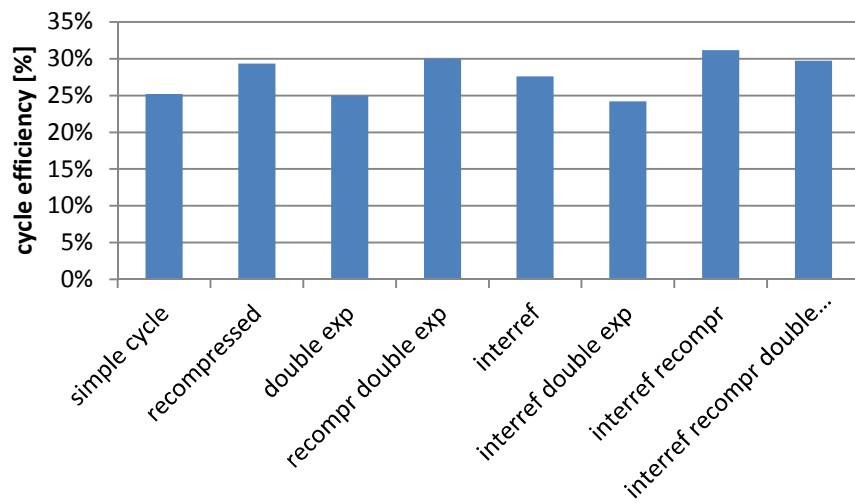


Fig. 4-27: comparison between maximum efficiencies at $T_{\max}=500^{\circ}\text{C}$ and $p_{\max}=100\text{bar}$ with different cycle configurations

Simple and interrefrigerated cycles were thus analyzed in detail, and their annual performance was characterized. In the next chapter the methodology adopted in doing so is explained.

5 OFF DESIGN STUDY

Once the optimal cycle configuration has been determined through the thermodynamic analysis, a characterization of the performance of the plant in off design conditions is necessary. The value of DNI and its incidence angle on the solar field is going to be strongly variable throughout the day and the year. Furthermore, weather conditions will affect the actual DNI in an unpredictable way. For these reasons, the plant will often work in off design conditions. To obtain the plant yearly energy yield thus, it is necessary to proceed with the detailed dimensioning of each component, and with the description of its off-design operations. The simulation of their functioning will then be integrated in a single code. The overall simulation of the power block was implemented in Excel, characterizing the components either by means of polynomial expressions describing their functioning as a function of specific parameter (turbomachines), or directly implementing their characteristic equations in Excel and internally determining their off design performance (heat exchangers). A decision had to be made on the regulation of the plant: the choice was to keep constant the rotation speed of the turbomachines, simplifying their coupling with the generator, and adapt the pressure level of the cycle accordingly, in order to achieve the matching between turbine and compressors. The change in internal pressure of the system though implies the need for a CO₂ buffer, in which part of the HTF will be stocked as the pressure goes down, in order to maintain the specific volume in the piping constant.

The off design of the solar field was once again simulated in EES. The interaction between power block and SF is still in the form of a Dynamic Data Exchange: inlet temperature and pressure in the solar field are used to compute plant mass flow, as well as pressure drop in the solar field. These two values are then used as input to the power block solver. It will determine the inlet pressure of the turbine in order to match, with the calculated mass flow, the pressure conditions in the solar field and the ones in the power block (turbine inlet, last regenerator HP outlet). The calculation will then be iterated until convergence is reached.

A description of how the off design of each plant component was simulated is presented in the following paragraphs.

5.1 SOLAR FIELD

The code developed for the design of the solar field could easily be modified in order to work with a fixed geometry. The information regarding number of rows and piping diameters is taken from the results obtained with EES in the design phase and fed to the off design code as a lookup table. The logic behind the computation remains the same: the mass flowing in the rows is adapted to guarantee the desired outlet temperature. The equations to set the thermal input in the HTF as well as its velocity in the piping are removed, and these parameters will just result from geometry, effective DNI and ambient temperature.

In order to proceed with the annual simulation for the power plant then, the starting point is to characterize the meteorological conditions of the construction site, day by day. To this purpose, the National Solar Radiation Data Base elaborated by NREL was employed [42]. For a specific location, the database provides an hourly value of DNI, to which can also be associated a certain position of the sun in the sky, by means of geometric calculations taking into account the geographical coordinates of the place and the hour of the day. Two angles are used to define the position of the sun: azimuth and zenith. Azimuth is the angle existing between the vector connecting the position of the observer and the geographical north, and the projection of the vector pointing the Sun on the plane of the horizon. Zenith is the angle between the normal to the plane of the horizon and the vector pointing the Sun.

The Sun coordinates are used to calculate the relative position of the Sun with respect to the collectors, and thus the value of effective DNI (EDNI), which is obtained as:

$$EDNI = DNI \cdot K(\varphi) \cdot \eta_{shadowing} \quad (5-1)$$

where $K(\varphi)$ and $\eta_{shadowing}$ are two parameters that represent the effects depending on Sun position, that contribute to the final dampening of the initial value of DNI. These effects will be now briefly described.

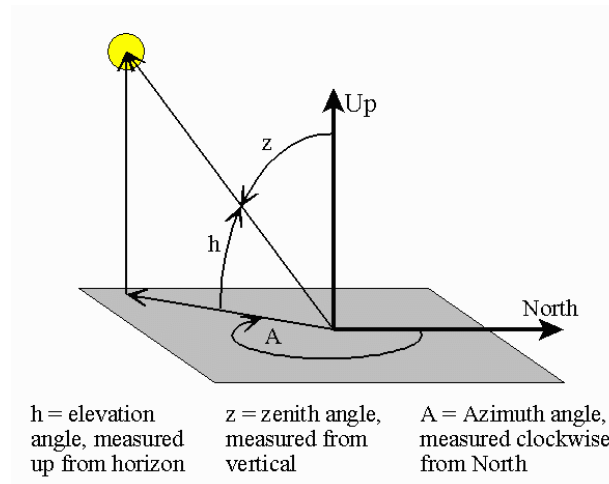


Fig. 5-1 : coordinate system to which the position of the sun is referred [43]

If we consider the angle between the normal to the aperture plane and the incoming rays, defined as *incidence angle*, it is possible to elaborate a function on the basis of experimental results (typically provided by the collector constructor), depending on the incidence angle and including its effect on the following factors:

- 1) cosine effect
- 2) tail end losses
- 3) absorber support shading
- 4) dependency of optical property on incidence angle

The cosine effect simply consists in considering only the perpendicular component of the DNI vector, by multiplying it for the cosine of the incidence angle and projecting it on the normal to the aperture plane.

Tail end losses consider the reduction in aperture area caused by the inclination of the sun rays: the portion of radiation hitting the mirrors in the terminal part of the collector will not be reflected on the receiver, leading to an apparent reduction in its total length, as can be seen in Fig. 5-2.

The last two effects consider the shading caused on the reflecting surface by the absorber tube, and the fact that parameters like mirror reflectivity, coating absorptivity, etc., may not be isotropic in space: different direction of the sun

rays may thus induce changes in the optical parameters, and consequently modify the nominal optical efficiency [eq. (3-34)].

l_φ = loss of useful collector length
 l = collector length
 φ = incidence angle
 f = focal distance

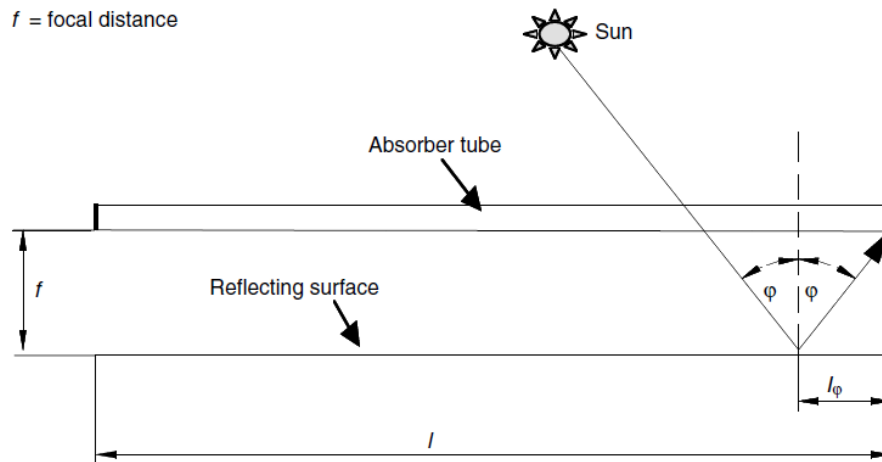


Fig. 5-2 : end losses in parabolic trough collector [12]

The resulting function that sums up the influence of the incidence angle on the effective DNI in the case of ET100 collector is:

$$K(\varphi)_{ET100} = \cos(\varphi) - 5.251 \cdot 10^{-4} \varphi - 2.8596 \cdot 10^{-5} \varphi^2 \quad (5-2)$$

where φ indicates the incident angle [44].

Another effect that has to be taken in account is the shading between adjacent rows. This will only occur with very low solar altitudes (zenith close to 90°), that is at sunrise and sunset. The relevant parameters affecting the entity of the shading are aperture width of the collectors and spacing between rows:

$$\eta_{shadowing} = \frac{W_{eff}}{W} = \min \left[\max \left(0; \frac{L_{spacing}}{W} \cdot \frac{\cos(\varphi)}{\cos(z)} \right); 1 \right] \quad (5-3)$$

where W is the aperture width, W_{eff} the effective aperture width, $L_{spacing}$ is the distance between adjacent rows and z is the azimuth angle [45].

Mapping of the off design performance of the plants was done considering this final value as the variable of the study, and developing polynomial expressions

that describe the dependency of interest parameters as a function of effective DNI. Starting from the meteorological database described earlier then, it is possible to get to an hourly value of EDNI, depending both on the actual DNI and on the position of the sun, and consequently calculate a daily production profile.

5.2 TURBINE

5.2.1 TURBINE DESIGN

To carry out the detailed design of the turbine, a code programmed in the '70s by professor Ennio Macchi at Politecnico di Milano was employed: AXTUR [32]. The software makes use of the loss model developed by Craig & Cox for axial turbines [33], and given the desired operative parameters of the turbomachine, as well as the nature of the working fluid, performs an optimization on the geometry of the turbine in order to maximize its efficiency. The final output of the computation provides the user with all the information about the geometry of each row of the machine, from the number of blades to the geometry of the channels, as well as its overall performance, including efficiency and degree of reaction. The number of stages has to be an input as well, with a maximum of three stages.

Expansion ratio, mass flow, inlet temperature and pressure were taken from the solution of the optimum case carried out during the thermodynamic analysis. As an example, the sizing of the turbine in the case of simple cycle is described below. Single stage and two stage solutions were compared, observing a minimum variation in the overall performance of the machine. The comparison between the two options is summed up in Table 5-1.

Table 5-1 : performance comparison between single and two stages turbine ($T_{in}=550^{\circ}\text{C}$, $p_{in}=94,93$ bar, $p_{out}=40$ bar, nominal mass flow=680,2 kg/s, rotation speed=10000 rpm)

	η_{global}	stage degree of reaction	stage loading factor
Single Stage	88,316	0,519	1,999
Two stages	88,636	0,456/0,578	1,311/1,62

The rotation speed, fixed for both machines at 10000 rpm, was selected on the basis of an optimization of the turbine efficiency, taking also in account that, since turbine and compressor will be coupled on the same shaft in order to avoid the need for a gearbox, the selection for one will affect the performance of the other as well. In our case though, the optimum velocity for the turbine has proven to be ideal also in the dimensioning of the compressor, as will be shown in the next paragraph. The efficiency of the single stage turbine as a function of its rotation speed is shown in Fig. 5-3.

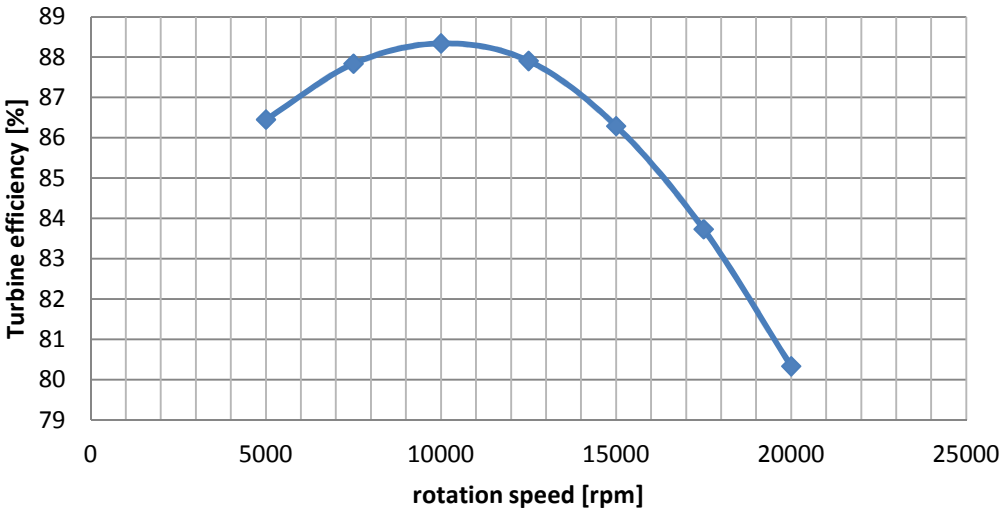


Fig. 5-3: global efficiency of single stage turbine as a function of its rotation speed ($T_{in}=550^{\circ}C$, $p_{in}=94,47$ bar, $p_{out}=40$ bar, nominal mass flow=680,2 kg/s)

It was thus decided to opt for a single stage machine, implying lower costs and start up times, with only a minor reduction in its global efficiency. Compared with the conservative efficiency value assumed for turbines in the preliminary study phase (85%), the actual dimensioned turbine achieves a better performance. An example of AXTUR output is shown in Fig. 5-4: it can be seen how for each stage a table is available for both stator and rotor, listing their geometrical description, inlet and outlet velocities from the row, and a complete description of the velocity triangles in the machine. Total admission was always selected.

stadio no.1										
<i>eta gl</i>	88,207%									
<i>etats</i>	88,207%	<i>nc.p.adm</i> 88,200%						<i>kis</i> 2,37241		
<i>etafi</i>	88,207%							<i>r*</i> 0,41654		
<i>etalf</i>	90,398%							<i>gda</i> 100%		
<i>zet</i>	<i>coef</i>	<i>lift</i>		<i>prcf</i>	<i>sec</i>	<i>ann</i>	<i>traf</i>	<i>e.cin.</i>	0,02423	
0,0688	0,97111	12,08	<i>s</i>	0,01787	0,00676	0,01259	0	<i>disk</i>	0,00061	
0,0486	0,96877	12,49	<i>r</i>	0,01608	0,00577	0	0,034	<i>scav</i>	0	
<i>loss coeff. -></i>				<i>s</i>	0,03305	0,01251	0,02328	<i>blp</i>	0	
<i>(l=0,00000)</i>				<i>r</i>	0,03582	0,01285	0	<i>leakg</i>	0	
DIMENSIONI:										
	<i>pale</i>	<i>[zwei]</i>	<i>bas</i>	<i>corda</i>	<i>cmim</i>	<i>cev</i>	<i>passo</i>	<i>sp.te</i>		
<i>s</i>	43	0,4789	0,02662	0,06127	0,0091	0,0091	0,0428	0,0005		
<i>r</i>	43	0,6005	0,03704	0,06548	0,01036	0,01036	0,0434	0,00052		
	<i>rmed</i>	<i>hin</i>	<i>hev</i>	<i>tipcl</i>	<i>flhub</i>	<i>fltip</i>	<i>hhd</i>	<i>cl.s-r</i>	0,0027	
<i>s</i>	0,29583	0,10218	0,10218	0	0	0	0,1727	<i>cl.r-s</i>	0,0296	
<i>r</i>	0,29583	0,10518	0,14803	0,001	-30,009	30,009	0,2502	<i>cl.d-h</i>	0,0033	
TRIANGOLI VELOCITA':										
	<i>win</i>	<i>[mach]</i>	<i>wex</i>	<i>[mach]</i>	<i>u</i>	<i>angoli</i>	<i>ingr</i>	<i>mt-ex</i>	<i>fl-ex</i>	
<i>s</i>	53	0,1218	386,9	0,9295	340,8		90	12,271	12,231	
<i>r</i>	90,1	0,2164	343	0,8543	340,8		65,514	13,811	13,721	
	<i>alfa1</i>		<i>beta1</i>		<i>beta2</i>		<i>alfa2</i>		<i>lta</i>	
	12,231		65,514		13,721		95,298		100,765	
	<i>w1</i>		<i>w1</i>		<i>w2</i>		<i>v2</i>		<i>u1</i>	
	0,73709		0,17159		0,65351		0,1557		0,64924	
	<i>va1</i>		<i>vt1</i>		<i>va2</i>		<i>vt2</i>		<i>u2</i>	
	0,15615		0,72036		0,15501		-0,0144		0,64924	
									<i>vel. adm. con sqrt(2*dhis)</i>	
									524,873	

Fig. 5-4 : example of AXTUR output table

In Fig. 5-5 the meridian section of the single stage turbine dimensioned for the simple cycle can be observed. It can be noticed how the machine, compared to a vapor turbine, is extremely compact, and will imply lower costs for the manufacturing. Furthermore, the thermal inertia of the turbine will be much lower, as will be its start up time.

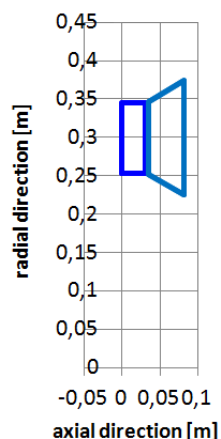


Fig. 5-5: meridian section of single stage turbine

5.2.2 TURBINE OFF DESIGN

Starting from AXTUR's output, a new code was developed in order predict the performance of the dimensioned turbine in off design conditions. To do so, the same loss model adopted by AXTUR had to be implemented in VBA.

5.2.2.1 CRAIG&COX LOSS MODEL

Craig & Cox loss model has been developed on the basis of an extensive experimental campaign, to obtain correlations describing the effect of each parameter contributing to the overall efficiency loss in a radial turbine. First of all the loss are divided into two groups: the first group includes the effects that cause the work transferred from the gas to the turbine blades to be less than what expected from the change in tangential momentum of the fluid (fluid-dynamic effects, friction, etc.); the second group includes all the other phenomena that reduce the actual work per unit total mass flow with respect to what obtained on the surface of the blades (leakage, windage, etc.). All the loss causes are assumed to be independent one from the other, so that the correlations describing them can be developed independently, and the global effect on the performance can be calculated as a combination of their effects.

<i>Group 1</i>	<i>Group 2</i>
Guide profile loss.	Guide gland leakage loss.
Runner profile loss.	Balance hole loss.
Guide secondary loss.	Rotor tip leakage loss.
Runner secondary loss.	Lacing wire loss.

Fig. 5-6 : loss sources in axial turbine [33]

Conceptually, the overall efficiency can be then obtained according to the following expression:

$$\eta_{turbine} = \frac{\text{Work done in blading} - \text{group 2 losses}}{\text{Work done in blading} + \text{group 1 losses}} \quad (5-4)$$

The denominator of the expression is equivalent to the ideal work without fluid dynamic dissipative effects, and can thus be calculated as the isentropic enthalpy variation across the turbine.

The loss sources belonging to group 1 can be expressed as a fraction of the kinetic energy of the fluid in the stage:

$$\text{Group 1 losses} = (X_p + X_s + X_a)_s \frac{C_1^2}{2} + \left(X_p + X_s + X_a \frac{C_2^2}{W_2^2} \right)_r \frac{W_2^2}{2} \quad (5-5)$$

where: X_p , X_s and X_a are the loss coefficients corresponding respectively to profile losses, secondary losses and annulus losses; C_1 is the absolute velocity at the outlet of the stator; C_2 and W_2 are respectively the absolute and relative velocity at the outlet of the rotor. Profile losses include the fluid dynamic effects between the flow and the surface of the blades; secondary losses are connected with fluid dynamic effects on the walls at the root and tip of the blades; finally, annulus losses depend on the effect of casing geometry on the flow.

The velocity to be used to calculate the losses is the one relative to the surface interested by the interaction with the flow, so the absolute velocity in the case of the stator (C_1), the relative velocity in the case of the rotor (W_2). Annulus losses in the rotor make an exception, because the casing is always at rest.

Each one of the coefficients listed above is in turn composed of different elements, which try to isolate the effect of a single phenomena or parameter. In the case of profile loss, for example, we have to consider the following components contributing to the global loss:

- 1) Reynolds number
- 2) aspect ratio
- 3) blade angles and passage geometry
- 4) pitch to backbone length ratio
- 5) Mach number
- 6) incidence

Each one of these elements contributes to the total profile loss, which can be calculated, once the single factors have been obtained from specific correlations, as a combination of them.

Group 2 losses are not directly connected with the solution of the flow dynamic in the stages, and can be added once the problem has already been solved, as a decrement of the obtained efficiency. They can be considered in the form of correlations giving a $\Delta\eta$ depending on the specific effect, and the final efficiency of the turbine can be calculated as:

$$\eta_{turbine} = \eta_{t,group\ 1} - \sum_{Group\ 2} \Delta\eta \quad (5-6)$$

The first term in the expression indicates the efficiency obtained for the turbine including only loss sources from group 1. To actually calculate this term, one has to integrate group 1 losses in the solution of the flow through the turbine stages, that is in the identification of the velocity triangles at the inlet and the outlet of every row. To that end, two coefficients are defined in AXTUR, and consistently in the off design code, as a combination of the loss coefficients relative to group 1 elements. The first coefficient, Z, allows the calculation of the actual velocity at the exit of the considered stage, reducing it with respect to the isentropic case (no losses). Real velocity can then be calculated as:

$$v_{real} = v_{isentropic} \sqrt{1 - Z^2} \quad (5-7)$$

An additional effect related to group 1 losses, is the reduction of the throat area in the blade channels: this reduction is caused by the growth of the boundary layer along the blades. The effective throat area seen by the flow then, which is used in the computation of the isentropic velocity, will then be expressed as:

$$A_{throat} = A_{geometric} \cdot \zeta \quad (5-8)$$

Where ζ is the coefficient representing the described reduction effect.

Including these two coefficients (Z and ζ) in the flow solution, allows taking into account group 1 losses. The velocity triangles obtained in this way will

permit the calculation of the actual work done on the blades by the flow, through Euler's equation:

$$w_{eul,group\ 1} = C_{1t}U_1 - C_{2t}U_2 \quad (5-9)$$

where the subscript t indicates the tangential component of the absolute velocity, whereas U indicates the peripheral speed of the rotor. This work can be divided by the isentropic enthalpy difference across the turbine, obtaining the efficiency considering only to the effect of group 1 losses:

$$\eta_{t,group\ 1} = \frac{w_{eul,group\ 1}}{\Delta h_{is}} \quad (5-10)$$

Through equation (5-6) finally, it is possible to subtract the group 2 efficiency losses and recalculate the real Eulerian work specific to the total mass flow as:

$$w_{eul} = \eta_{turbine} \cdot \Delta h_{is} \quad (5-11)$$

To accomplish the solution of the flow, the information about the losses is not sufficient: additional correlations are required in order to predict flow angles, which are necessary in the definition of the velocity triangles. Many different authors have developed such correlations, covering a wide spectrum of flow conditions. For subsonic flows, Ainley correlations have been used [34]: they predict the exit flow angle as a function of the isentropic Mach number.

5.2.2.2 OFF DESIGN CODE COMPUTATIONAL LOGIC

The computational structure of the code is summed up in Fig. 5-7. The program gathers the information about the machine geometry from the AXTUR output. Inlet values of temperature, pressure and mass flow are set by the user, as well as the rotation speed of the machine. From here, the code proceeds with the solution of the first stage row, in order to determine its outlet condition which will in turn be used for the solution of the following row.

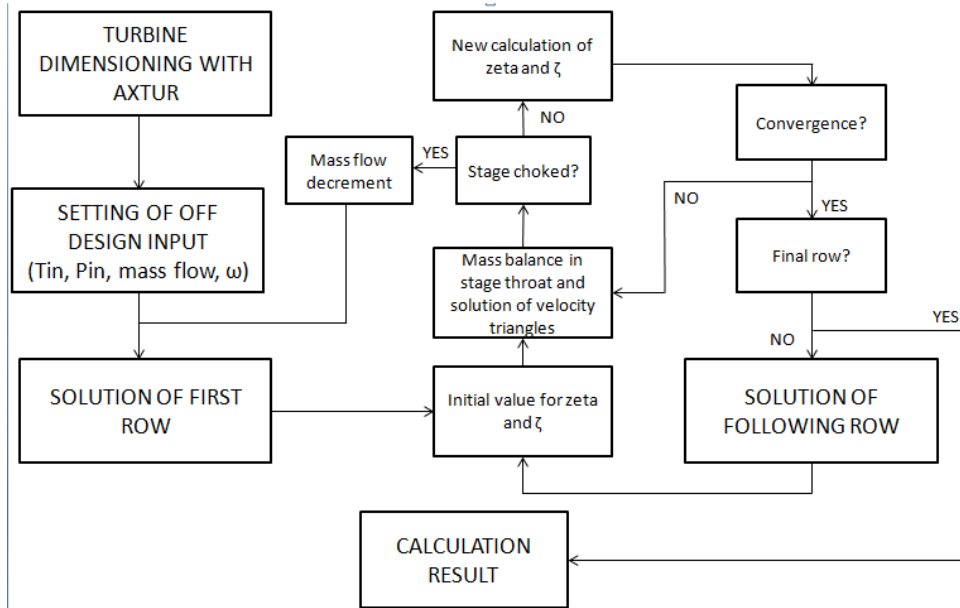


Fig. 5-7 : off design code flow chart

The solution of a row does not change in its structure between stators and rotors, but the reference frame used for velocities is always the one relative to the blades (W for the rotor and V for the stator). The key equation to be solved is the mass balance in the throat of the blades channel. The advantage of performing the calculation in the channel throat is that the flow is perpendicular to the section in this point, and no angles have to be considered. Considering the conservation of total temperature (again, relative to the appropriate reference frame), and the throat area reduction due to the boundary layer [eq.(5-8)], the isentropic speed can be obtained, and consequently the actual speed [eq.(5-7)] and flow angles (Ainley correlations).

$$\left\{ \begin{array}{l} v_{isentropic,throat} = Ma_{is} \cdot c_{sound,throat}(T_{0in}, p_{0in}) = \frac{\dot{m}}{\zeta \cdot A_{geom} \cdot \rho_{is,throat}(Ma_{is})} \\ \text{flow exit angles} = f(Ma_{is}) \\ zeta, \zeta = f(\text{geometry}, \text{flow angles}, Ma_{is}) \end{array} \right. \quad (5-12)$$

Iteration has to be performed on the problem, because the value of Z and ζ depend on the outlet condition as well. Once the solution converges, the code moves to the following row, and starts over until it reaches the exit of the turbine.

If the mass flow that is imposed for a certain machine at a specific inlet total condition is too elevated, the turbine might incur into choking. To determine the exact value of the mass flow that induces the choke, it is necessary, starting from a choked functioning point, to gradually lower the inlet flow down to the point where the machine works just below its choking condition. The solution obtained will indicate the mass flow value corresponding to choking, at the selected inlet temperature, pressure and rotation speed. Choking can occur in either one of the stages of the turbine: the calculation with the decremented mass flow though, will always have to start over with the first stage, because the reduction in mass flow will also affect the rows preceding the one in which the choke occurred. In turn this will change the inlet condition of the choked row.

Fixing inlet conditions (T_0 , p_0), and increasing gradually the mass flow, an off design map of the turbine can be plotted, indicating overall efficiency and expansion ratio as a function of the flow. In Fig. 5-8 the described curve is shown at three different rotation speeds.

The value of efficiency reaches a peak corresponding to the design condition, and then decreases towards the choking point, where the curves stop. When the mass flow is decreased substantially, efficiency drops up to the point where the flow speed is so low compared to the peripheral speed that the turbine starts behaving as a compressor, increasing the enthalpy of the working fluid (negative efficiency region).

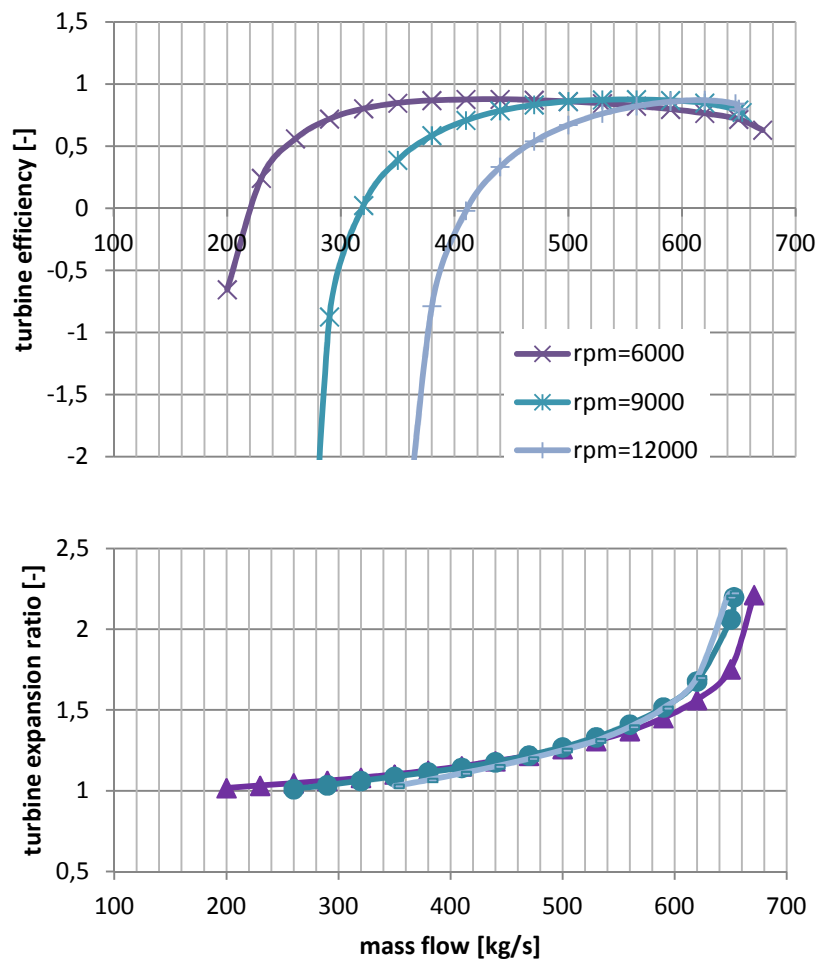


Fig. 5-8 : efficiency and expansion ratio as a function of mass flow ($T_{in} = 550 \text{ }^\circ\text{C}$, $p_{in} = 100 \text{ bar}$, $m_{nom}=600\text{kg/s}$)

To compare the turbine performance curves it is more convenient to define a dimensionless mass flow:

$$\dot{m}_{adimensional} = \frac{\dot{m} \sqrt{R_{gas} T_{oin}}}{D^2 p_{oin}} \quad (5-13)$$

Being that geometry and working fluid of the turbine are fixed, the corresponding variables can be omitted, and the resulting expression, equivalent to its dimensionless form even if not strictly dimensionless, is in the form of:

$$\dot{m}_c = \frac{\dot{m}\sqrt{T_{0in}}}{p_{0in}} \quad (5-14)$$

Once efficiency and expansion ratio of the turbine are mapped with respect to this corrected mass flow, it can be seen how all curves of the same turbine collapse in a single one (Fig. 5-10). These curves can then be used to predict the performance of the turbine, if its rotation speed is fixed, at an arbitrary combination of mass flow and inlet conditions.

These final dimensionless curves are implemented, in the form of polynomial expressions, in the Visual Basic code simulating the functioning of the power block.

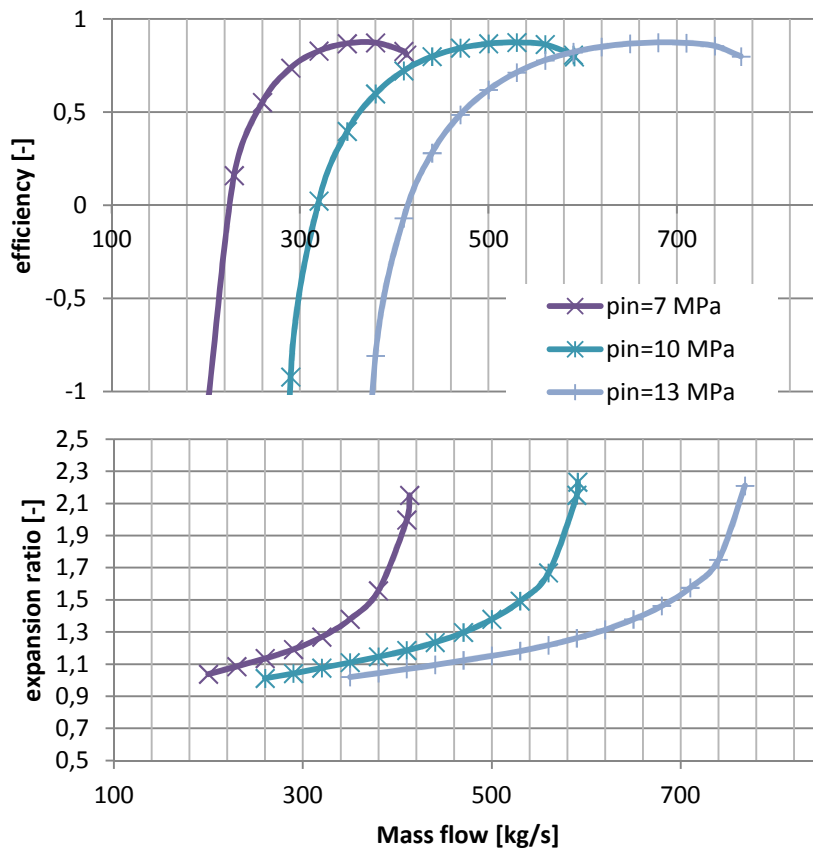


Fig. 5-9: dimensional curves for turbine at different inlet pressures ($T_{in}=550\text{ }^{\circ}\text{C}$)

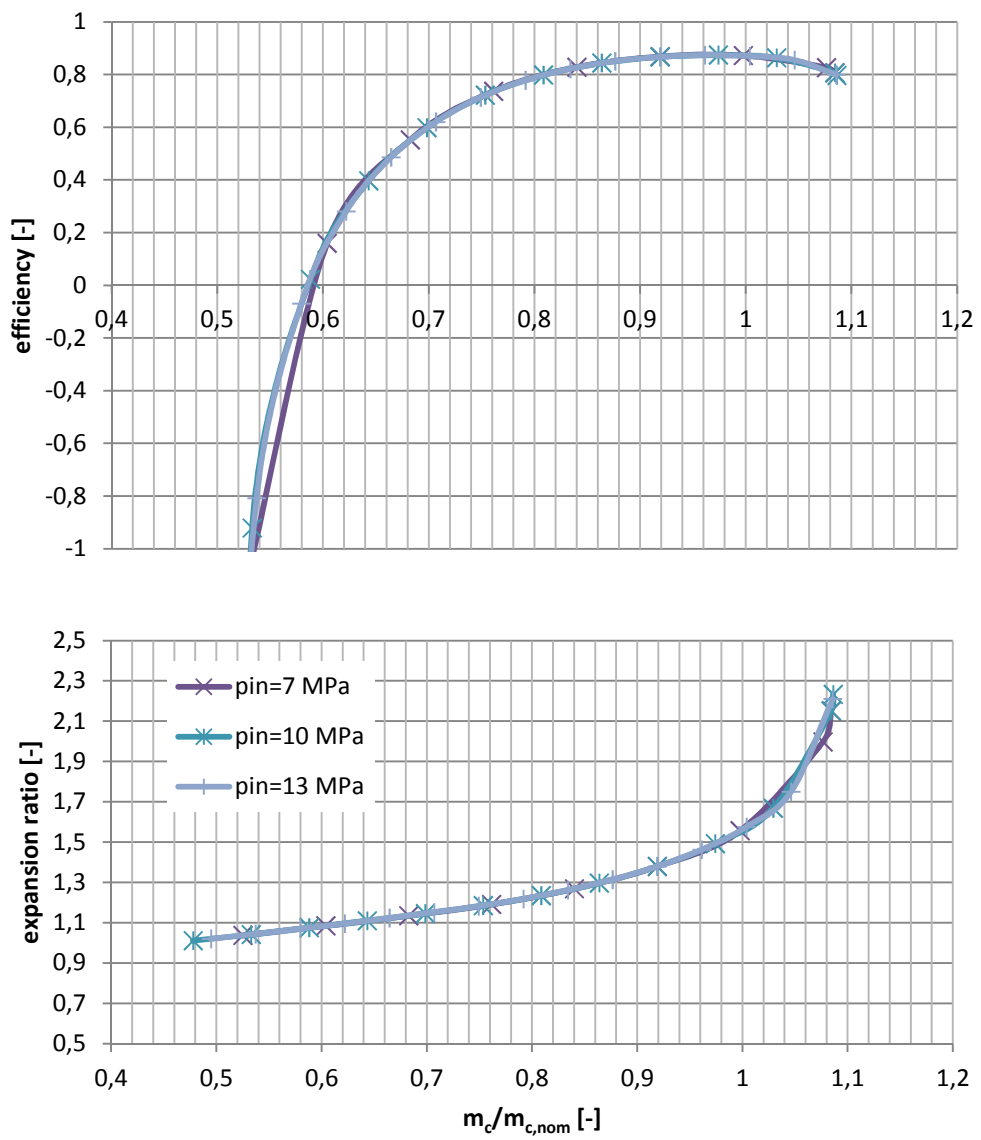


Fig. 5-10 : dimensionless form of curves from Fig. 5-9. The corrected mass flow is standardized on the nominal value

5.3 COMPRESSOR

The dimensioning and off design characterization of the compressor is complicated by the fact that the working fluid cannot be treated as an idea gas, as it has been done for the turbine. Moreover, very little information is available in literature on the modeling of sCO₂ large compressors for power plants applications.

A first estimate of compressor type, size and design efficiency, can be attained consulting Baljé charts (Fig. 5-11). In these charts, maximum achievable performance is mapped as a function of two dimensionless parameters, specific diameter and specific speed, defined as:

$$D_s = \frac{D \cdot H_{is}^{1/4}}{\sqrt{\dot{V}_{in}}} \quad (5-15)$$

$$N_s = \frac{N \sqrt{\dot{V}_{in}}}{H_{is}^{3/4}} \quad (5-16)$$

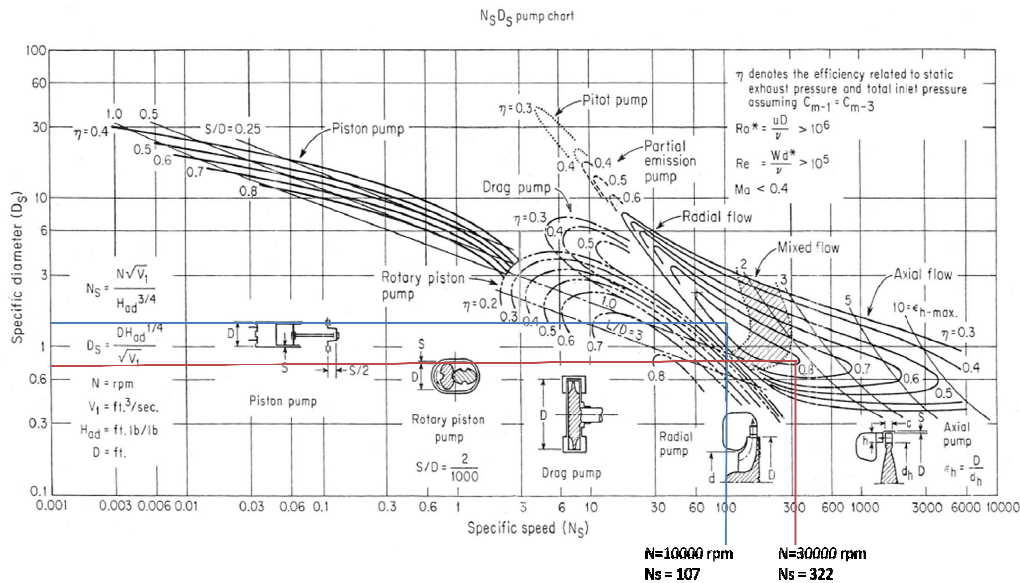


Fig. 5-11 : Baljé chart for compressors, and example of specific speed vs specific diameter matching. Blue and red lines represent the dimensioning of the simple cycle compressor at two different rotation speed (respectively 10000 rpm and 30000 rpm) [35]

Once the desired design conditions are known (volumetric flow and isentropic enthalpy change), fixing a rotation speed allows us to enter the graph, and select the specific diameter that yields the maximum efficiency. Depending on the region in which the resulting point is situated, the typology of machine will be determined.

Two possible alternatives are represented on the chart in Fig. 5-11, for the compressor in the simple cycle optimal case. With a rotation speed of 10000 rpm, it can be seen how we obtain an optimal value of efficiency of about 85%, and a corresponding specific diameter of 1.5, leading to an actual diameter of 0.675 m and a rotor tip speed of 353 m/s. The machine is a radial compressor. Increasing the rotation speed would change the compressor typology, and reduce its size, as well as its nominal performance. We also have to consider that compressor and turbine will be coupled on the same shaft, and the rotation speed will have to be the same. The value of 10000 rpm for the rotation speed, determined during the design phase of the turbine is found then suitable also for the compressors. Analogous calculations can be done considering the nominal functioning point in the case of the other cycle configurations, always leading to a value for the nominal efficiency and machine diameter.

Once the design characteristic of the compressor has been determined, its off design performance must be evaluated somehow. The most interesting work on the topic has been carried out by Sandia National Laboratory [36]. In their facilities, they have been testing a small prototype of radial compressor working with CO₂ close to the critical point. The turbomachine is integrated in a compression test loop, which allows changing its working condition in order to collect experimental data on its performance at different operation points.

A simulation code analogous to what seen for the turbine has also been developed by Sandia, implementing a combination of two loss models for radial compressors [37-38]. The code was provided with a property database to take into account the real gas behavior of the fluid. The predicted performance curves obtained from the simulation have then been compared with experimental data from the compression loop, to validate the model: the

agreement between the two is remarkably good, as it can be seen from Fig. 5-12.

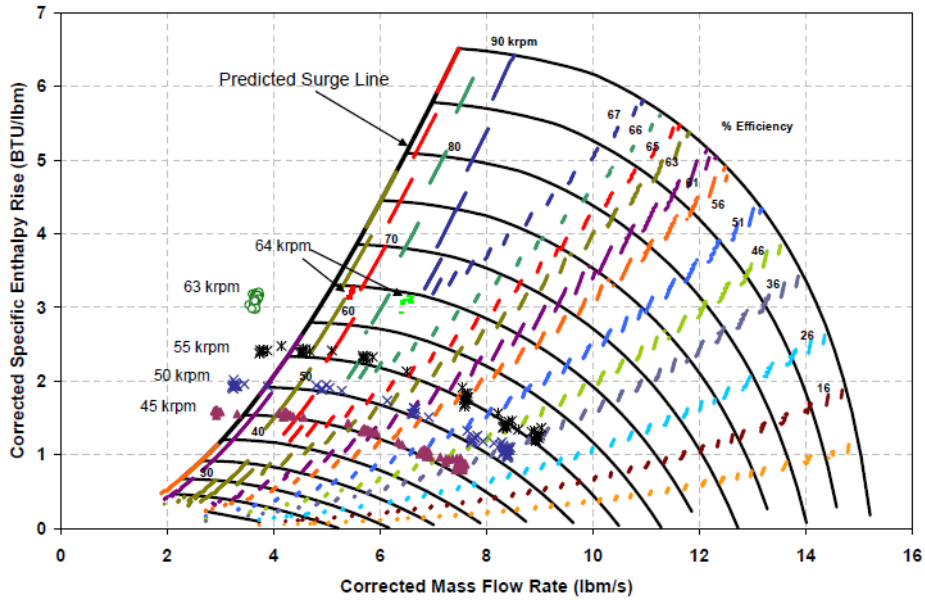


Fig. 5-12 : predicted compressor performance map and measured functioning points (Sandia) [36]

On the basis of these experimental results, J. Dyreby et al. [39] have elaborated a semi-empiric curve to describe the functioning of the compressor through the definition of dimensionless parameters, in order to obtain general curves that could be used, similarly to what seen for the turbine, to predict the performance of the compressor in an arbitrary functioning point. The three variables employed are dimensionless forms of respectively mass flow, compressor head and efficiency. They are named modified flow coefficient, ideal head coefficient and modified efficiency, and defined as:

$$\phi^* = \frac{\dot{m}}{\rho_{in} U_c D_c^2} \left(\frac{N}{N_{design}} \right)^{1/5} \quad (5-17)$$

$$\psi^* = \frac{\Delta h_{is}}{U_c^2} \left(\frac{N_{design}}{N} \right)^{(20\phi^*)^3} \quad (5-18)$$

$$\eta^* = \eta \left(\frac{N_{design}}{N} \right)^{(20\phi^*)^5} \quad (5-19)$$

If the exposed non-dimensioning is applied to the performance map shown in Fig. 5-12, a single curve is obtained, summing up all the functioning points. The agreement between this new dimensionless curve and the experimental data is not as good as what reported from Sandia, especially in the high flow coefficient region. We will though see how the compressor of the cycles under study will work during their off design always in a narrow neighborhood of the design flow coefficient, due to the variation of the pressure level of the cycles. The disagreement between prediction and experimental result when the compressor is far from the design point thus will not be a problem.

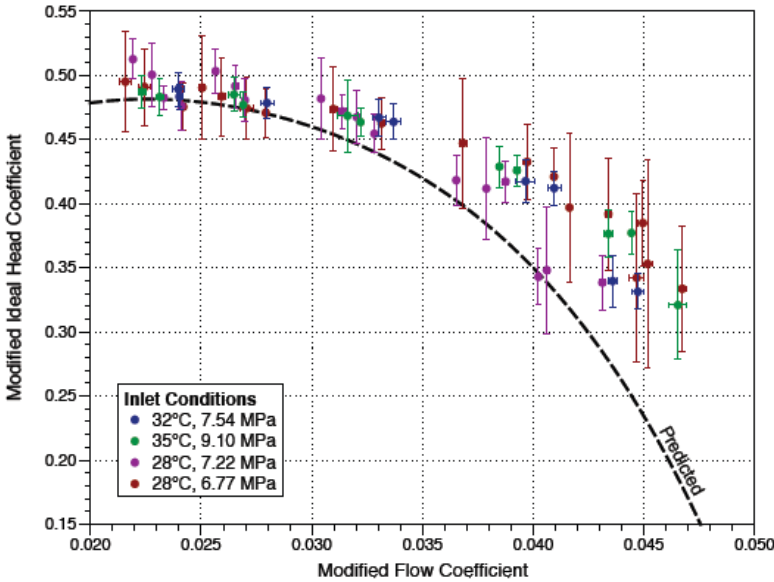


Fig. 5-13 : dimensionless performance curve of compressor versus experimental points from Sandia facility [39]

The size of the compressor in Sandia test facility is hardly comparable with what would be employed in a power plant with the nominal power of the current study, but the machine typology is the same. The non dimensional functions relative to its performance have then been re-standardized on the values deriving from the design dimensioning carried out with Baljé, to obtain an approximate off design characteristic. As already pointed out, the compressor operating point will remain close to the nominal value also when

mass flow is largely reduced, due to the change in compressor inlet pressure that adapts the fluid density, maintaining the volumetric flow close to a constant value. Fig. 5-14 shows the dimensional curves representing the performance of the compressor defined for the simple cycle, keeping constant the inlet conditions (40bar 47°C) and varying the mass flow.

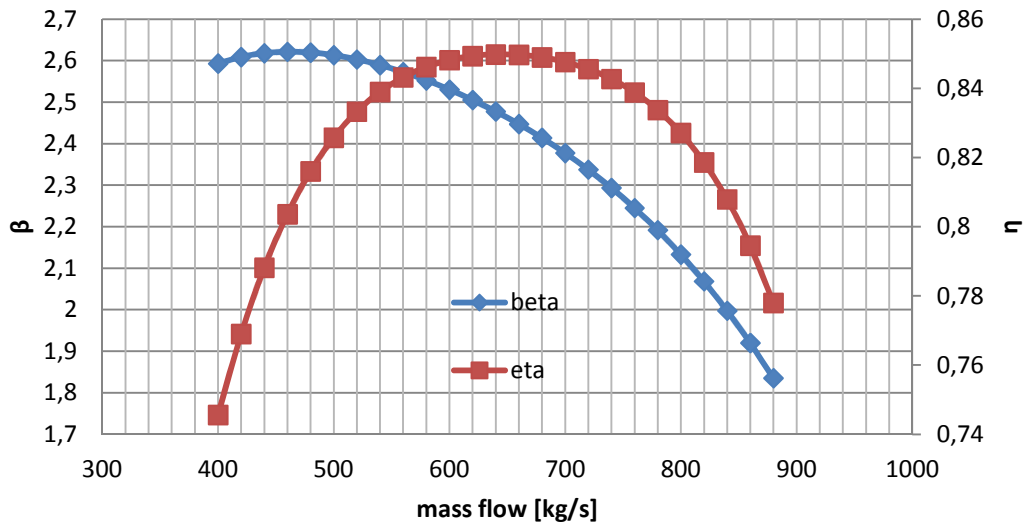


Fig. 5-14 : dimensional performance curves for simple cycle compressor ($T_{in} = 47\text{ }^{\circ}\text{C}$, $p_{in} = 40\text{ bar}$)

5.4 HEAT EXCHANGERS

The off design simulation of the heat exchangers is based, both for regenerators and precooler, on the matching of the value of UA deriving from the temperature profiles, with the predicted value obtained scaling up or down the design UA with the mass flow, according to the expression:

$$UA_{off} = UA_{design} \cdot \left(\frac{\dot{m}_{off}}{\dot{m}_{design}} \right)^n \quad (5-20)$$

The reason behind this operation is that, being the geometry of the heat exchanger fixed, the UA value will only depend on the change in overall heat transfer coefficient U . Its value will depend on the combination of internal and external convection film coefficients, which represent the main component of

the total thermal resistance. For internal forced convection, the Nusselt number, which in turn will determine the film coefficient, depends on the Reynolds number elevated to a certain exponent. An example of such correlations was already described in chapter 3, and was employed in the solution of the cross sectional heat transfer problem in the collector [eq. (3-11)]. That correlation presents though a complicated dependency on the Reynolds number, that is present both directly and indirectly, affecting the value of the friction factor as well. Another typical correlation employed to calculate the Nusselt number in the case of internal flow in circular section tubes is the Dittus-Boelter equation [49], where the Reynolds's exponent is 0.8:

$$Nu = 0.023Re^{0.8}Pr^{-2/3} \quad (5-21)$$

As for external convection, a correlation for the average Nusselt number in the case of cross flow on cylindrical tube is due to Hilpert [49]:

$$\overline{Nu} = CRe^mPr^n \left(\frac{Pr}{Pr_s}\right)^{1/4} \quad (5-22)$$

where the exponent depends on the value of Reynolds as listed in Table 5-2.

Table 5-2 : m coefficient value as a function of Re for Hilpert's correlation

Re	m
0.4-4	0,385
4-40	0,466
40-40.000	0,618
40.000-400.000	0,805

The dependency of the Nusselt number on the Reynolds, can be transferred, considering fixed geometry and assuming that the viscosity does not change drastically, on the mass flow. The exponent for the mass flow ratio in eq. (5-19) was set to be 0.7, in virtue of what seen for the Reynolds in the two Nusselt correlation discussed.

Temperature profiles in the regenerators have to be determined contextually with the solution of the power block, because they affect the temperature and pressure values in its points. Knowing the mass flow on the two sides and one

of the inlet temperatures (the one of the flow coming from the turbine), we are left with a degree of freedom that has to be saturated by guessing one of the other temperatures, and checking that energy balance [eq. (5-23)] and UA value constraint [eq. (5-26)] are both respected.

$$\dot{m}_{cold}(h_{out} - h_{in})_{cold} = \dot{m}_{hot}(h_{in} - h_{out})_{hot} \quad (5-23)$$

On the other hand, once the regenerator has been solved, the precooler CO₂ side will already be completely determined, being the minimum temperature of CO₂ kept constant during the plant functioning, and being its inlet temperature in the precooler already determined solving the regenerator. Only the air side thus will have to be solved, adapting the air flow in order to balance the UA, again respecting the heat balance.

The calculation of the actual UA value of the heat exchangers, when temperature profiles are determined, is carried out discretizing the heat exchange in segments, small enough that the thermal capacity of the flow can be assumed to be constant in the interval. With respect to the small segment, the UA value can be then calculated by means of the logarithmic mean temperature difference:

$$LMTD = \frac{(T_{in,hot} - T_{out,cold}) - (T_{out,hot} - T_{in,cold})}{\ln\left(\frac{(T_{in,hot} - T_{out,cold})}{(T_{out,hot} - T_{in,cold})}\right)} \quad (5-24)$$

$$UA_{segment} = \frac{Q_{segment}}{LMTD_{segment}} \quad (5-25)$$

$$UA_{tot} = \sum_i UA_{segment,i} \quad (5-26)$$

As for pressure drops, the methodology adapted replicates Thermoflex heat exchanger off design simulation. With respect to the nominal condition, a resistance factor is defined as:

$$\mu = \frac{\Delta p_{nom}}{v_{avg,nom} \dot{m}_{nom}^2} \quad (5-27)$$

This factor is kept constant in all functioning conditions, allowing the determination of the overall pressure drop on a side of the HX as:

$$\Delta p_{side} = \sum_i (\mu_{side} \cdot v_{in} \cdot \dot{m}^2)_{segment,i} \quad (5-28)$$

Nominal pressure losses are set to 0.3 bars in both regenerators side, and to 1 bar in the precooler and intercooler CO₂ side. As for their air side, the pressure loss is set to 150 kPa.

5.5 POWER BLOCK SECTION

All the components described are integrated in Excel to simulate the power block. Each point of the cycle is characterized with its values of temperature and pressure, and is connected with the previous and following points by means of the components equations. Inlet and outlet of turbomachines are related by the compression/expansion ratio and the efficiency of the machine, both calculated from polynomial functions elaborated on the basis of the off design study described in the previous paragraphs. As for the heat exchangers, the equations seen in paragraph 5.4 are directly implemented in Excel.

Maximum and minimum temperatures are kept constant for all the values of solar radiation, as well as ambient temperature. The only variable based on which the off design study has to be carried out then, is the value of effective DNI (EDNI), that is the DNI already corrected to take into account the effect of the incidence angle, as well as shadowing and end losses. A variation in EDNI will affect the mass flow that the SF can provide, at the target outlet temperature. The effect of a mass flow change will in turn cause the pressure levels of the plant to slide towards new values, according to the off design performance maps of the turbomachines (which work at constant rotation speed) until an equilibrium is reached in which pressure drops in components, and expansion and compression in turbomachines, are matched to attain a coherent pressure profile.

The only variable on which the code is free to act in order to achieve the pressure matching is the turbine inlet pressure, that is the pressure of the first point in the power block open circuit. In addition to this, one value of

temperature will have to be set for the high pressure outlet of each regenerator to respect the constraint on the UA value, as exposed in the previous paragraph. By changing these variables, and respecting all the thermodynamic boundaries, the unique solution of the power block off design functioning can be identified.

es						DNI	400	Solve		
	T [C]	p [Mpa]	h [kJ/kg]	s [kJ/kgK]	rho [kg/m3]	deltap EES [bar]	1,95421			Inputs passed to EES:
4	550	4,619698	1047,7711	3,037552	29,5355043	deltap VBA [bar]	1,954210005	FIXED		48,15118983 [bar]
5	442,25845	1,984925	924,85591	3,037552	14,68589454	diff	2,41142E-09	INDEP. VAR		424,3311881 [C]
5	457,42514	1,984925	942,24118	3,061599	14,37493236			SF OUTPUT		
6	165,03459	1,9654871	625,96061	2,513577	24,35208638			SF INPUTS		
1	47	1,9296115	509,28434	2,206859	34,65632939			OBJ & BOUND		
2	120,79346	4,8348502	565,67527	2,206859	71,68324834	Changing var	4,619697983		boundaries:	
2	137,56542	4,8348502	583,93783	2,252259	67,67119676		4,6491669			press
3	424,33119	4,815118	900,2184	2,835286	36,56386963		4,6191669			temp
									convergence check:	0,48%
										0,49%
mdot	288,6									

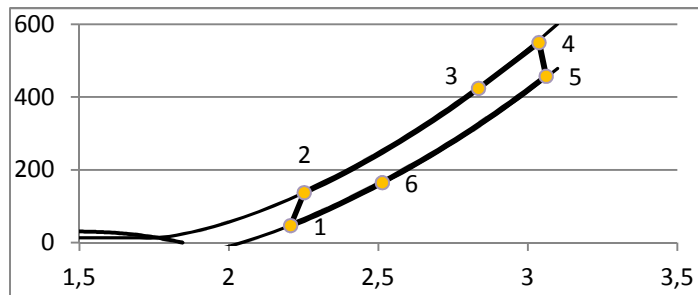


Fig. 5-15 : PB off-design Excel solution sheet and corresponding cycle T-s

The solution of the power block balance is done using Excel add-in Solver. Mass flow and pressure drop across the solar field are taken from the solution of the SF off design performed in EES: imposing the mass flow, the Solver changes the value of turbine inlet pressure until it attains a pressure difference between the two points representing inlet and outlet of the SF in the power block simulation equal to what obtained from the EES simulation. In doing so, a constraint is imposed on the regenerator UA, which has to match its off-design value, determined from eq. **Errore. L'origine riferimento non è stata trovata.** according to CO₂ mass flow. The constraint is fulfilled by the Solver adapting the regenerator HP side outlet temperature. Once the Solver converges to a solution, a new SF inlet condition, different from what considered at the previous iteration, will be determined: EES will then compute the off design of the field with the updated inputs, yielding new values of mass flow and SF pressure drop. The iteration is

continued until the relative difference between the pressure and the temperature values in the two simulations at the connection points between power block and solar field is lower than a specified tolerance.

Once the thermodynamic state of CO₂ is determined in each point of the plant, it is possible to proceed with the solution of the air side of the heat exchangers performing the heat rejection. The air mass flow is obtained once again using Excel Solver, in order to respect both off design UA constraint and energy balance in the heat exchangers. To the value of air mass flow is directly associated a value of pressure drop, calculated using eq. **Errore. L'origine riferimento non è stata trovata.**, which can be used to compute the power consumption of the corresponding blower.

The off design of the plant was solved in a range of EDNI covering the expected working condition during the annual functioning, obtaining a map showing how its parameters of interest change as a function of the irradiance. The mapping of the performance of the cycles varying the effective DNI allowed the development of polynomial functions that describe the off design of the power plant as a function of the EDNI value. Combining these functions with the hourly DNI database finally led to an annual energy production profile, and to the assessment of the yearly energy yield associated with the plant configuration.

The results of the mapping are discussed in the next chapter.

6 ANNUAL RESULTS DISCUSSION

6.1 PERFORMANCE INDEXES

The parameters employed in the mapping of the off design to fully characterize the performance of the plant are the solar field efficiency and power block efficiency, which product yields the global efficiency of the plant.

The solar field efficiency is defined as the net thermal input in the HTF across the SF over the total energy radiating on the collectors in the form of EDNI:

$$\eta_{SF} = \frac{\dot{Q}_{in\ HTF,net}}{EDNI \cdot A_{SF,tot}} = \frac{\dot{m}(h_{out\ SF} - h_{in\ SF})_{HTF}}{EDNI \cdot N_{collectors} \cdot W_{collector} \cdot L_{collector}} \quad (6-1)$$

Power block efficiency is calculated taking into account the auxiliary consumption caused by the blowers that move the cooling air in the heat exchangers employed for the heat rejection:

$$\eta_{PB} = \frac{\dot{P}_{turbine} - \sum \dot{P}_{compressors} - \sum \dot{P}_{blowers}}{\dot{Q}_{in\ HTF,net}} \quad (6-2)$$

The product of solar field efficiency and power block efficiency yields the global efficiency of the plant, with respect to the EDNI:

$$\eta_{global} = \eta_{SF} \cdot \eta_{PB} \quad (6-3)$$

$$\dot{W}_{out} = EDNI \cdot A_{SF} \cdot \eta_{global} \quad (6-4)$$

Referring to the actual DNI, we can express the power output dividing the efficiency of the plant in three distinct terms, representing respectively the optical efficiency, thermal efficiency in the solar field and piping system, and electric conversion efficiency:

$$\dot{W}_{out} = DNI \cdot A_{SF} \cdot \eta_{optical} \cdot \eta_{thermal} \cdot \eta_{PB} \quad (6-5)$$

where:

$$\eta_{optical} = \frac{\dot{Q}_{inc, coll}}{DNI \cdot A_{SF}} = \eta_{opt\ nom, coll} \cdot K(\varphi) \cdot \eta_{shadowing} \cdot \eta_{fouling} \quad (6-6)$$

$$\eta_{thermal} = \frac{\dot{Q}_{in,HTF}}{\dot{Q}_{inc,coll}} \quad (6-7)$$

In the calculation of the optical efficiency, a corrective factor was introduced, to take into account fouling caused on the reflectors surface during the annual functioning of the plant by dust and weather conditions. The fouling factor was set to 0.94. The nominal collector optical efficiency was determined in chapter 3 [eq. (3-34)].

The product of optical efficiency, thermal efficiency and power block efficiency yields the solar-to-electric efficiency of the power plant

$$\eta_{StE} = \eta_{optical} \cdot \eta_{thermal} \cdot \eta_{PB} \quad (6-8)$$

The efficiency definition introduced can be extended and referred to the annual energy production. For each hour, the power term in MW is directly associable with the corresponding energy production in MWh, since both plant performance and irradiance are assumed constant throughout the whole hour. It is important to remember that the plant will be functioning only in those hours during which the value of EDNI is greater than the lower limit established during the performance mapping.

$$\begin{aligned} W_{year} &= \\ &= \sum_{year} (DNI \cdot A_{SF} \cdot \eta_{optical} \cdot \eta_{thermal} \cdot \eta_{PB})_{if \ EDNI > EDNI_{min}} = \\ &= DNI_{TOT} \cdot A_{SF} \cdot \eta_{opt,year} \cdot \eta_{th,year} \cdot \eta_{el,year} = DNI_{TOT} \cdot A_{SF} \cdot \eta_{overall} \end{aligned} \quad (6-9)$$

where DNI_{TOT} represents the sum of all hourly values of DNI in the hours of the year that respect the limit in minimum EDNI, and $\eta_{overall}$ is the product of optical, thermal and electric yearly efficiencies.

6.2 SIMPLE CYCLE VS INTERCOOLED CYCLE

Solar field efficiency, net electric efficiency and global efficiency profiles as a function of EDNI for simple and intercooled cycles are compared in Fig. 6-1 : off design performance of simple and intercooled cycles as a function of effective DNI.

As expected from the parametric results carried out in chapter 3 on the performance of the collectors, the efficiency of the solar field decreases with intensity of the radiation, as a consequence of the increasing relevance of heat losses. Furthermore, the off design of the regenerator causes the inlet temperature of the HTF in the solar field to increase, thus increasing the average temperature of CO₂ and the thermal losses. Eventually, the radiation will be so low that in the point at higher temperature of the collector the heat gain of the HTF will be balanced by the heat loss to the environment. This condition is defined as collector *stagnation*, and sets a maximum achievable temperature associated with the specific irradiance condition. If the irradiance is further lowered, the collector will not be able to fulfill the temperature requirement, as stagnation will occur at lower temperatures. The functioning of the plant was then limited at a minimum EDNI value, equal to 220 W/m², that prevents the stagnation from occurring in the SF.

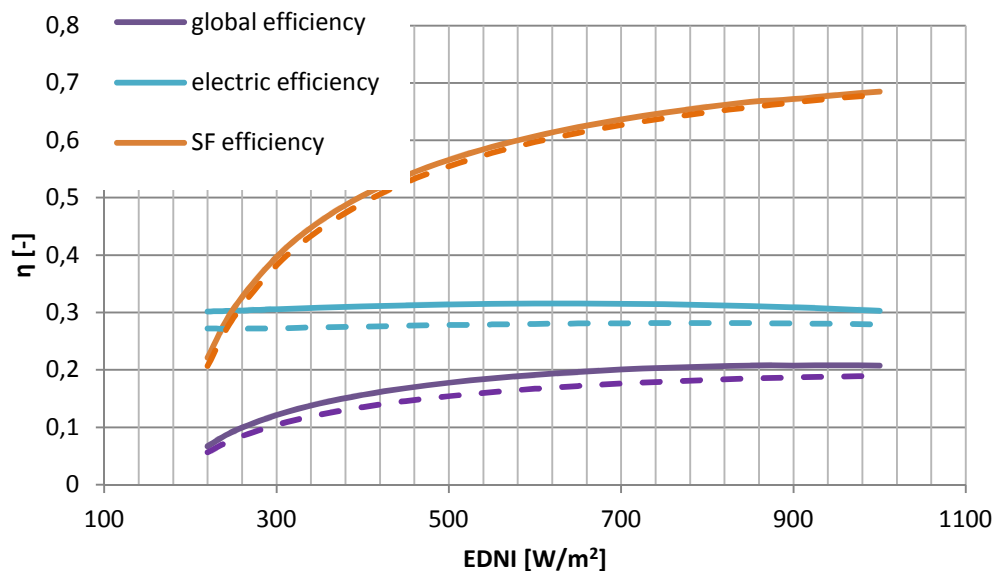


Fig. 6-1 : off design performance of simple and intercooled cycles as a function of effective DNI

The slightly higher values of SF efficiency in the case of intercooled cycle depend on the lower inlet temperature at the SF inlet that the HTF has in this configuration, which in turn leads to lower thermal losses both in collectors and piping.

The net electric efficiency, both in the case of simple and intercooled cycles, does not vary substantially throughout the EDNI spectrum analyzed. The regulation adopted for the turbomachines at constant rotation speed requires a total inlet pressure variation, in order to adapt their performance to the different mass flows induced by the changing EDNI. The cycle will then shift to lower pressures as the EDNI and the mass flow decrease, limiting the changes in volumetric flow. The cycle will though maintain the same shape: maximum and minimum temperatures are kept constant, and the pressure ratio β resulting from the matching of the turbomachines taking into account also the pressure losses slightly changes, leading to minor variations in cycle gross efficiency. The β profile is minimally increasing with the EDNI, as a consequence of higher pressure losses both in solar field and heat exchangers, as well as the interaction between the off design performance curves of the turbomachines. Fig. 6-2 shows for the simple cycle the described trend, as well as the turbine inlet pressure in the various cases, representative of the shift in the cycle pressure level.

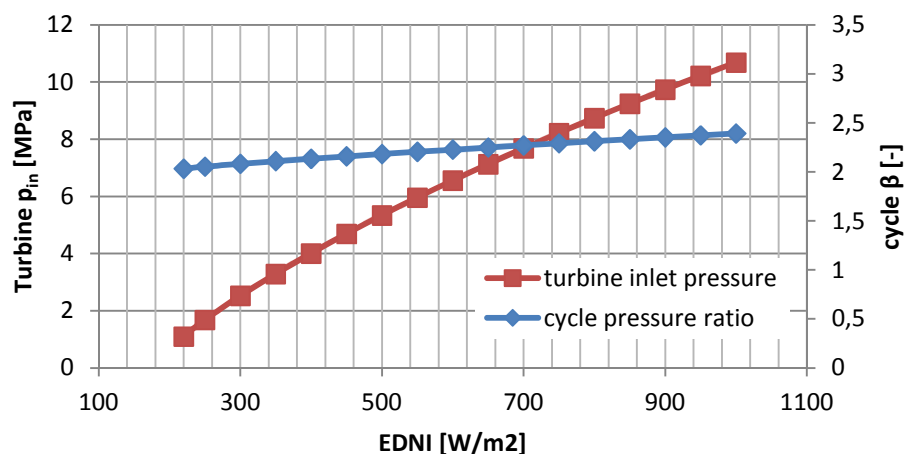


Fig. 6-2 : turbine inlet temperature and cycle pressure ratio as a function of EDNI in the case of simple cycle

The efficiency of the turbomachines also affects the performance of the cycles. In the case of simple cycle, turbomachines perform in off design maintaining the inlet value of corrected mass flow very close to the design value, thus operating at a constant efficiency, as shown in Fig. 6-3.

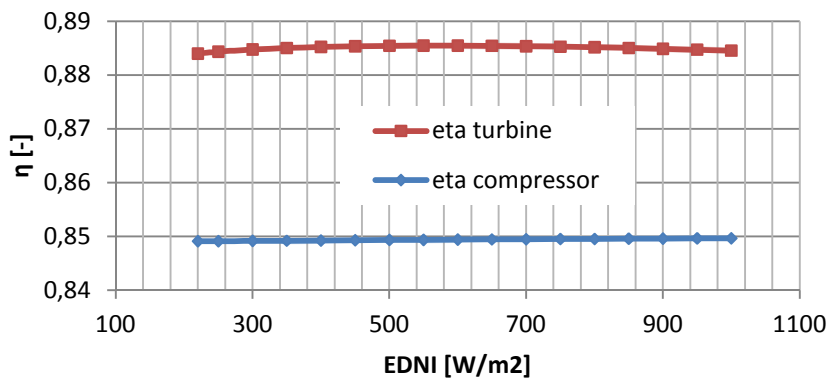


Fig. 6-3 : global efficiency of simple cycle turbine and compressor as a function of EDNI

As for the intercooled cycle, the situation is more complicated: the matching between three turbomachines instead of just two, makes so that both compressors and turbine are negatively affected as the EDNI reduces (Fig. 6-4). These variations contribute to make the electric efficiency more variable during the off design, reason for which the variation in net electric efficiency is higher for intercooled cycle, as can be seen in Fig. 6-5.

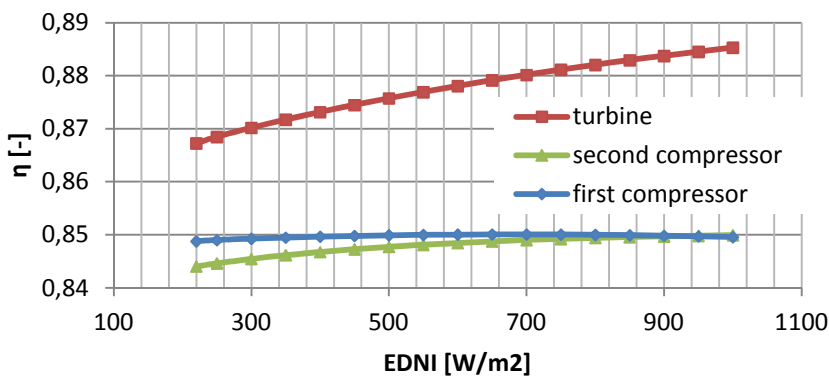


Fig. 6-4 : efficiency of intercooled cycle turbine and compressors as a function of EDNI

Net electric efficiency presents a maximum in both configurations, caused by the contrasting effects of the cycle β , increasing with the EDNI and having a positive effect on the gross efficiency of the cycle, and the power consumption in the auxiliary blowers, that largely increases as the HTF (and thus coolant air) mass flow increases. As shown in Fig. 6-5 the maximum is set at lower value of EDNI for the intercooled cycle, due to the higher auxiliary consumptions deriving from the additional intercooler.

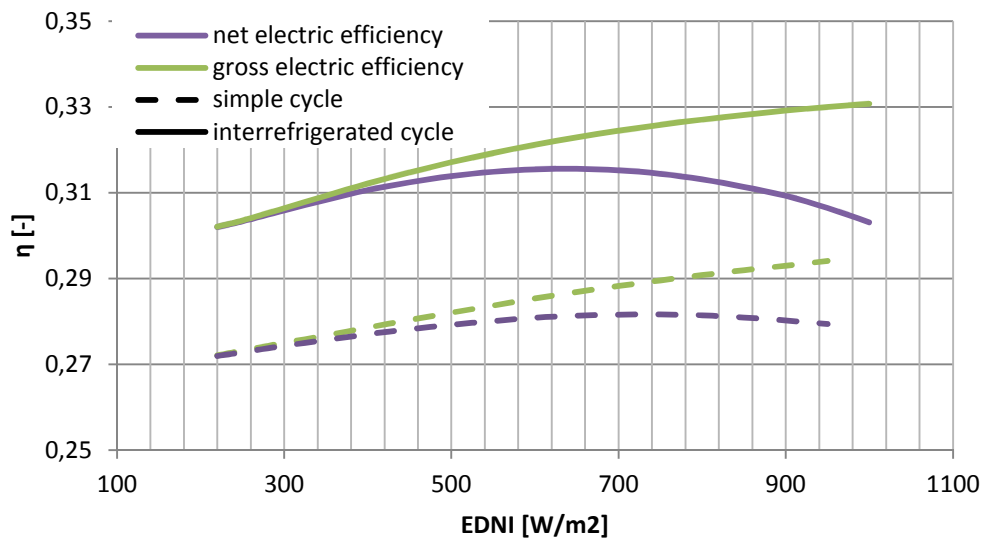


Fig. 6-5 : gross and net electric efficiency of simple and interrefrigerated cycles as a function of EDNI

The monthly production profile for intercooled and simple cycles during a characteristic year is shown in Fig. 6-6. It can be seen how the energy output in the case of intercooled cycle is always greater than for simple cycle, with an increase in energy production that remains between 11 and 12% in each month of the year. The percent difference is lower during the summer, and tends to increase in months during which the irradiance is low. This as a consequence of the difference in net electric efficiency between the two cycles, which is smaller at high EDNI values, and tends to increase as the EDNI decreases (Fig. 6-5).

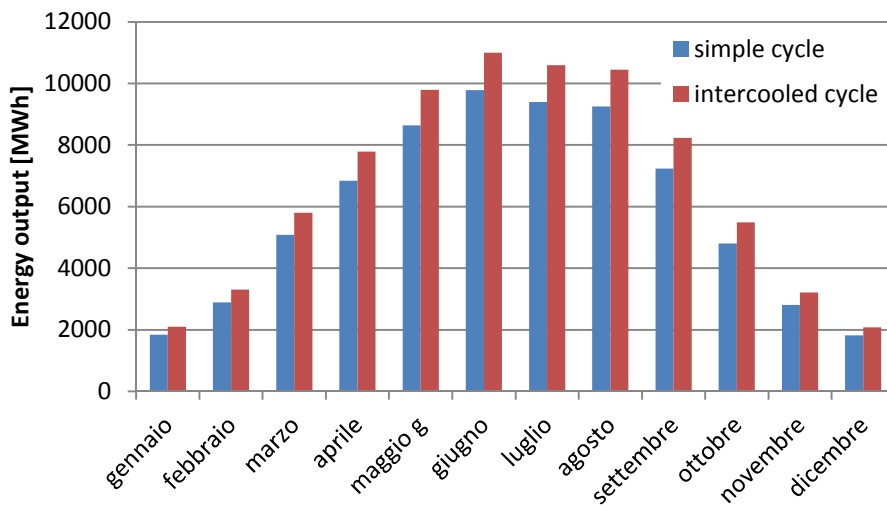


Fig. 6-6 : monthly energy production for simple and intercooled cycles

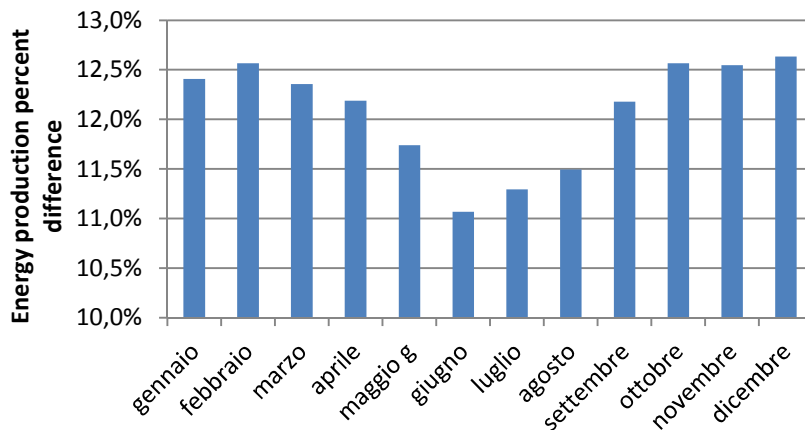


Fig. 6-7 : energy production percent difference between simple and intercooled cycles

Fig. 6-8 shows the hourly power output profiles respectively in a winter and summer characteristic day. First of all it can be noticed the difference in the shape of the hourly irradiance, which is narrower in winter, reflecting a later sunrise and earlier sunset with respect to summer. Secondly, taking a look at the value of EDNI, we can see how in winter it tends to be much lower than the DNI, presenting a local minimum in the central hours of the day due to the effect of the incidence angle. The electric power profile follows the same trend of the EDNI, leading to a substantial decrease in the energy output during the winter period.

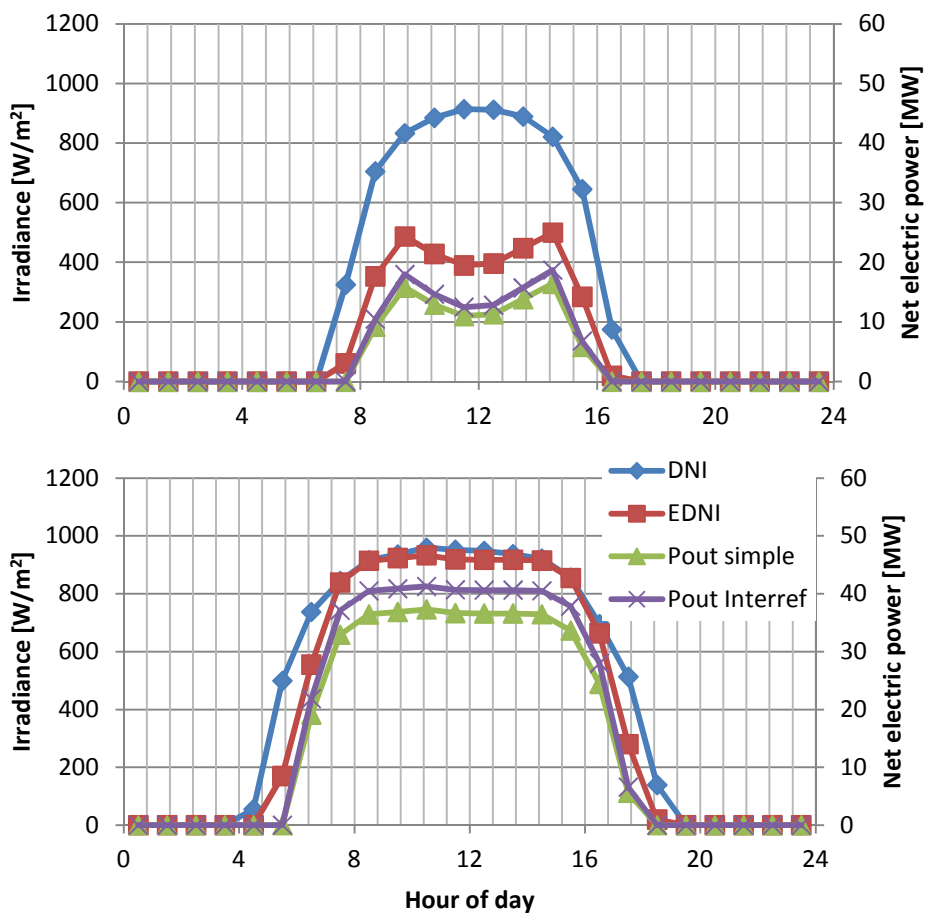


Fig. 6-8 : irradiance and power output profiles for a winter (above) and summer (below) characteristic day

The overall annual results for the two direct plants, as well as the reference performance of the indirect plant described in chapter 1, are summed up in Table 6-1.

Table 6-1 : annual simulation results for intercooled and simple cycles

	DNI_{TOT} [MW/m ²]	A_{SF} [m ²]	$\eta_{opt,year}$ [%]	$\eta_{th,year}$ [%]	$\eta_{el,year}$ [%]	$\eta_{overall}$ [%]	W_{year} [GWh]
simple	2.47	212504	60.83	73.50	28.01	12.52	70.366
intercooled	2.47	212504	60.83	74.71	31.26	14.21	79.829
reference	2.58	235899	52.75	91.46	33,27	16.05	97.818

Being the size of the solar field the same in the two direct plant configurations, the total energy annually radiating on the fields will be the same. Optical efficiency only depends on the performance of the collector and the construction site, so it is equal as well in the two cases. The difference in thermal efficiency is, as already mentioned, a consequence of the slightly different SF inlet temperature, lower in the case of intercooled cycle. The difference in annual performance is then mainly due to the two electric efficiencies, leading to a higher yearly energy yield in the case of intercooled cycle.

Comparing the results with the reference case, we can see how the performance indexes of the reference indirect plant are consistently higher than for the two direct plants studied, with the only exception of the optical efficiency. This last difference though is only determined by the assumptions made for the collectors optical performance in the current work, and should not be given too much importance. What is interesting is the dramatic difference in the overall thermal efficiency of the solar field. The substantially higher temperatures induced in the SF of the direct plants by the regeneration process and the setting of a higher T_{\max} for the cycles, imply heat losses in the solar field largely exceeding what seen for the reference case. Furthermore, the efficiency of the Rankine cycle employed in the reference plant, including also the additional consumption of the auxiliaries that in the indirect plant have to circulate the HTF in the SF, results higher than the efficiencies attained by the Brayton cycle configurations considered. The relatively high value of T_{\min} considered in the study in order to perform a dry heat rejection, combined with the limitation in maximum pressure imposed by the collectors mechanical resistance, make so that the $s\text{CO}_2$ Brayton cycles studied do not attain conversion efficiencies higher than what achieved by traditional Rankine cycles. As a consequence, the overall annual efficiency of the reference plant is higher, and the difference would raise even more if the assumptions made for the optical parameters of the collectors were set to be the same, thus eliminating the unjustified advantage attained by the direct plants in the annual optical efficiency.

Ways to improve the overall performance of the direct cycles must then be identified. A decrease in the T_{\min} of the Brayton cycles would certainly have a

positive effect on the power block efficiency, allowing the full exploitation of the real gas effect and raising the electric performance of the plants. In order to attain this temperature reduction, alternative solutions for the heat rejection could be considered. In particular, a good choice could be to switch to hybrid water-air cooling systems, in order to lower the minimum temperature of the Brayton cycles and limit at the same time the need for coolant water, normally not easily available in sites at high annual DNI values. An increase in the maximum pressure of the cycle would also increase its efficiency, and could be attained improving the mechanical resistance limit of the collectors' receivers, employing better materials for the absorber tube and optimizing its thickness.

As for the low SF thermal efficiency of the direct plants, employing better materials for the piping insulation could help reducing the total surfaces and in turn the losses in the piping system. Furthermore, lowering the degree of regeneration of the cycles, and thus the HTF inlet and average temperatures in the SF, might in turn have positive effects on the overall efficiency, if the reduction in power block efficiency is outbalanced by a corresponding gain in thermal efficiency.

In the next paragraph, an additional intervention that could lead to an improvement in the performance of the direct plants is investigated: the effect of a higher cycle T_{max} .

6.3 INTERCOOLED CYCLES AT HIGHER T_{MAX}

In order to investigate the potential benefit of an increase in the maximum temperature limit, the annual performance of the intercooled cycle was assessed increasing its maximum temperatures to 600°C and 650°C. The methodology followed during the study reflects what seen so far. Firstly, the thermodynamic optimum for the two cases was established, fixing maximum pressure and temperature and observing the variation in cycle efficiency as function of p_{min} . The optimal minimum pressure reveals to be independent from the T_{max} , remaining on the value of 30 bars. Then, the components of the two cycles were dimensioned, and their off design functioning was

characterized in agreement with what seen in chapter 5. The results of the off design performance mapping is shown in Fig. 6-9, for the three intercooled cycles at different T_{max} .

It can be seen how, as expected, an increase in the maximum temperature of the cycle implies higher electric efficiencies. The gain in electric conversion though is balanced by a decrease in the solar field efficiency, caused by the higher average temperature of the HTF in the collectors, and thus in thermal losses. Another effect of the higher temperatures in the solar field is an increase in the stagnation EDNI. This reduces the irradiance spectrum in which the power plant can function, consequently lowering the total annual operating hours.

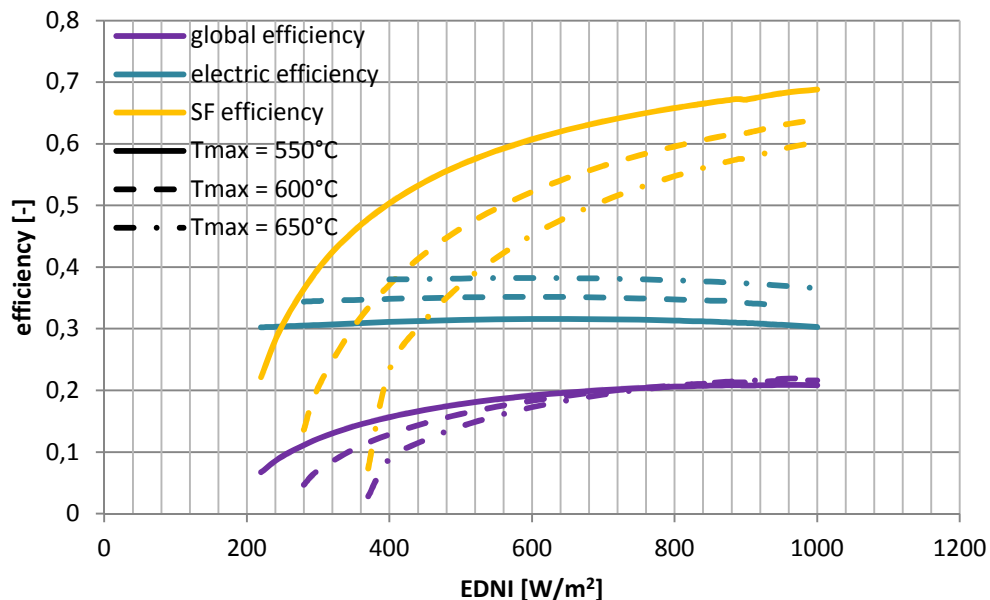


Fig. 6-9: off design performance intercooled cycles at different T_{max} as a function of effective DNI

The overall effect of the temperature raise can be observed in the global efficiency. If at high EDNI the plants with higher T_{max} attain a slightly better performance, as the EDNI decreases the increase in T_{max} has a negative effect on the global efficiency, due to the rapid reduction in SF performance. At low irradiance values then, high temperature plants will suffer both from a more limited functioning and a worse global efficiency.

The solar-to-electric efficiency profiles in winter and summer characteristic days are shown in Fig. 6-10. It can be observed the reduced functioning time for the cycle at T_{max} 650°C in the winter day: the plant loses one hour in the morning and one in the evening. Furthermore, in low effective irradiance days, the overall performance of the high temperature plants is consistently lower compared to the base case at 550°C. On the other hand, when the irradiance is higher, both high temperature plants can perform slightly better than the base case, as can be seen in the case of summer characteristic day.

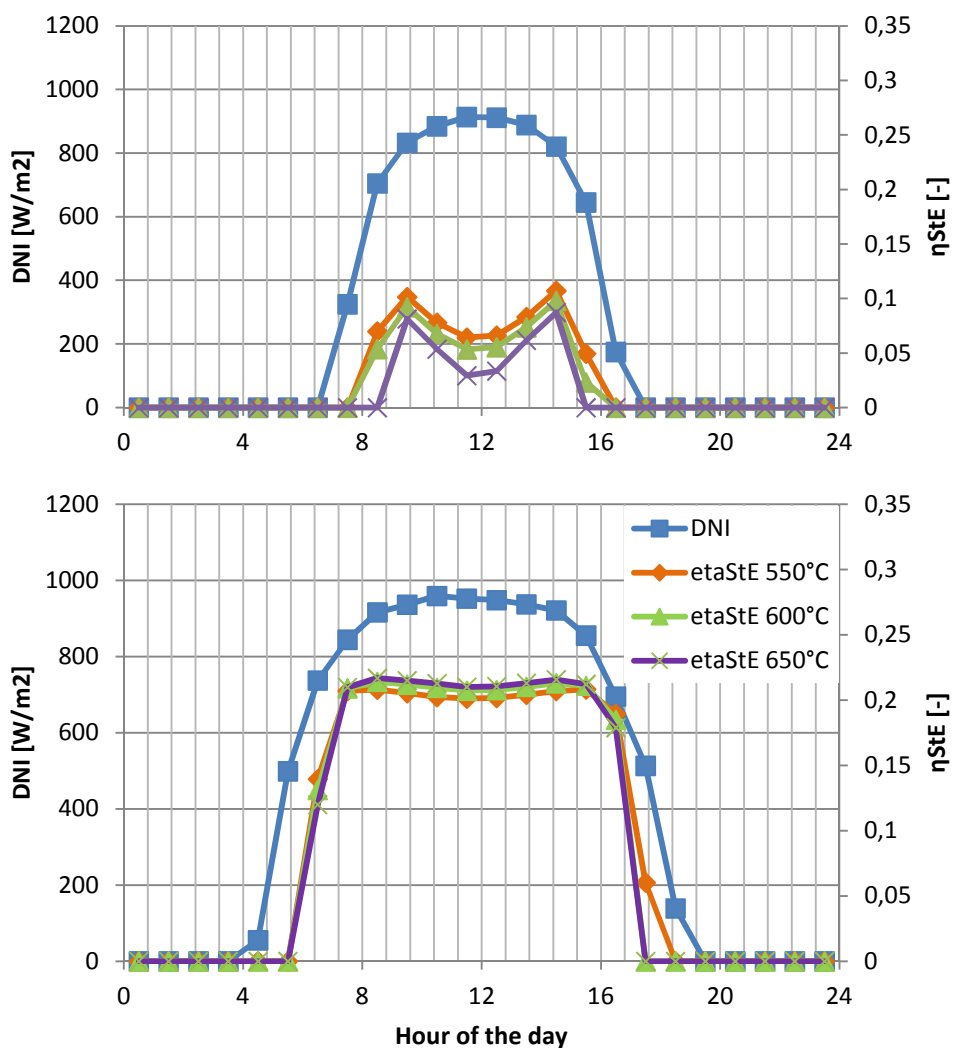


Fig. 6-10 : solar-to-electric efficiency of intercooled cycles at different T_{max} in winter (above) and summer (below) characteristic days

This reflects on the monthly solar-to-electric efficiency profile, shown in Fig. 6-11. During low irradiance months the low temperature plant performs much better than the other two. The performance though tends to even out as we move towards summer, up to the point where high temperature plants achieve a better monthly overall efficiency. The annual balance though remains in favor of the base plant at 550°C, as can be seen from Table 6-2.

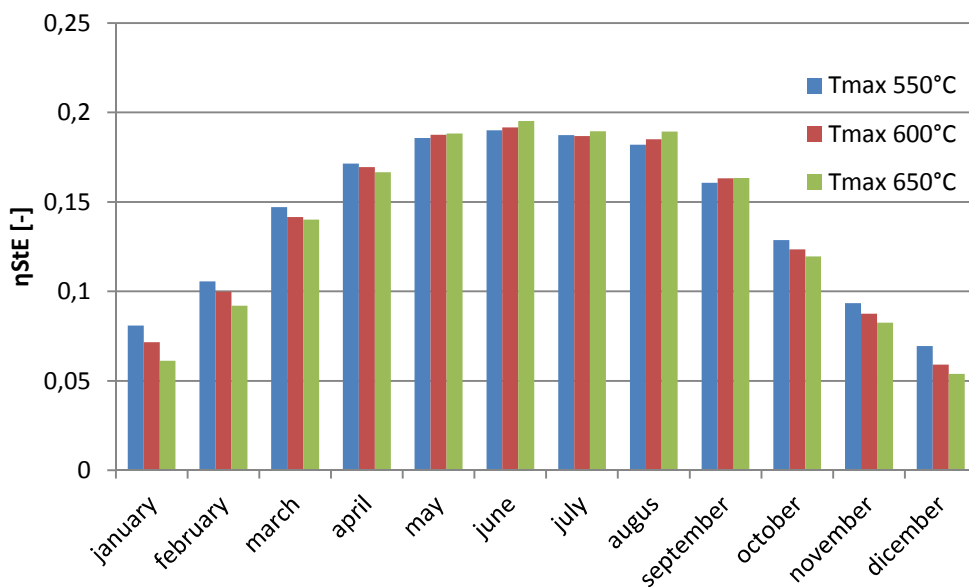


Fig. 6-11 : montly solar-to-electric efficiency of intercooled cycles at different Tmax

In conclusion, increasing the maximum temperature of the intercooled cycle does not seem to have a positive impact on the annual performance of the plant, without an intervention on the solar field in order to increase its thermal efficiency.

Table 6-2: annual performance of intercooled cycles at different Tmax

T_{max} [°C]	DNI_{TOT} [MW/m ²]	A_{SF} [m ²]	$\eta_{opt,year}$ [%]	$\eta_{th,year}$ [%]	$\eta_{el,year}$ [%]	$\eta_{overall}$ [%]	W_{year} [GWh]
550	2.47	212504	60.83	74.71	31.26	14.21	79.829
600	2.47	226070	60.83	65.76	34.86	13.95	81.383
650	2.47	248675	60.83	60.03	37.86	13.83	83.973

7 CONCLUSIONS

In the current work, the implementation of direct sCO₂ Brayton cycles coupled with a parabolic trough solar field was investigated. The study carried out introduces many new elements compared with what done so far in literature. First of all an innovative computational methodology based on the interaction between different softwares in order to simulate the functioning of the power plant is proposed. Accordingly, a thorough analysis covering a wide spectrum of possible Brayton cycle configurations is done. The analysis compares the different configurations, in order to assess which one is the most suitable for the application. The best options were then analyzed in detail, and characterized in their off design and annual performance. In doing so, a new instrument to better describe the turbine off-design functioning was developed.

The thermodynamic study was carried out through the interaction, programmed in Visual Basic in the form of a Dynamic Data Exchange, between two softwares: Thermoflex, employed for the power block, and Engineering Equation Solver, used to program the solar field simulation. A wide range of operative parameters was explored, assessing the performance of the cycles at various combinations of maximum pressure and temperature, and cycle pressure ratio, and identifying the optimal solution in each case. In the case of recompression and double expansion, the influence of split ratio and intermediate pressure level was also considered.

The results indicate that complex cycle configurations do not substantially improve the optimal thermal to electric conversion performance of the plant, once the limits in maximum pressure and temperature set by the structural resistance of the collectors are imposed. The solutions selected for the detailed study were then the simple regenerative cycle and the regenerative intercooled cycle, thanks to their good performances and plant simplicity. The efficiencies of the optimal solutions of the two cycles were mapped as a function of the regenerator UA, observing a strong influence of the latter on the performance of the cycles. The size of the regenerator was then fixed at an equal value for both, imposing a reasonable value for the temperatures pinch point, set to 20 °C.

To proceed with the annual simulations, the components of the plants had to be dimensioned, and their off design performance established. Turbine design was carried out in detail using an optimization code (AXTUR), and determining its geometry and design performance. The same code was then modified in order to work with a fixed geometry, developing a new code that allows the prediction of the dimensioned turbines off-design performance, in an arbitrary functioning point. Compressors were dimensioned resorting to Baljé diagram, and then characterized in their off design by means of semi-empirical curves developed on the basis of experimental results obtained by Sandia Laboratory in their compression loop. The functioning of the components was finally integrated in a Visual Basic code run in Excel, simulating the off design of the plant at various effective DNI values. The calculation of the EDNI was performed, starting from the value of DNI, time of the day and location, on the basis of optical considerations including the effect of the incidence angle and the shadowing between adjacent rows.

Mapping the performance parameters of the plant in a wide spectrum of EDNI values allowed the definition of polynomial functions describing the off design of the plant. Associating these functions with a database provided by NREL and characterizing hourly the irradiance condition for the selected construction site (Daggett, CA), it was possible to assess the yearly energy yield for simple and intercooled cycles. Energy production profiles have been characterized for the two plants in summer and winter characteristic days, demonstrating the consistent superiority of the intercooled cycle on the simple cycle. The results were then analyzed dividing the overall efficiency in its constitutive terms, each describing a specific performance aspect of the plant. A comparison with a reference indirect plant representing the technology state of the art was also introduced. The main difference between the two direct configurations is given by the electric efficiency of the cycles, higher for the intercooled cycle, which in both cases does not change dramatically even at irradiance conditions far from the design point. The introduction of intercooling in the direct plant power section, considering a fixed size of the solar field, guarantees an improvement in the annual energy yield with respect to the simple cycle configuration of about 12.8%, against the additional cost for a second compressor.

The comparison with the reference indirect plant showed how the overall performances of both direct cycles are strongly penalized by the high average temperatures in the solar field, which cause heat losses to be dramatically higher with respect to the indirect plant. Solar field thermal efficiency of direct cycles is almost twenty percentage points less than the indirect cycle, with values of 73.5% and 74.7% for simple and intercooled plants respectively, against 91.5% for the reference plant. In addition to this great deficit, the power block electric efficiency of the two direct cycles results lower as well compared with what attained by the Rankine cycle in the reference plant, even if the maximum temperature reached by the two Brayton cycles is more than 150°C higher. The main reason for this is the high T_{\min} considered in the study, which limits the real gas effects and does not allow the full exploitation of the advantages of supercritical gas cycles.

In order to improve its electric efficiency, the performance of the intercooled cycle was explored as its maximum temperature is increased above 550°C. Two new plants were dimensioned, setting their T_{\max} to 600°C and 650°C. The results show how, even if the electric efficiency of the power section increases up to 38% as the maximum temperature is raised, the additional thermal losses caused by an increase in the average temperature of the HTF across the solar field outbalance the advantages obtained in the thermal to electric energy conversion.

The comparison with the reference plant indicates how, in order to make direct sCO₂ Brayton cycles a competitive option, some improvements have to be introduced. A great positive effect on the overall efficiency could come from the reduction of the cycles T_{\min} , which would have to main consequences:

- the real gas effect at the inlet of the compressor would be intensified, leading to greater advantages in terms of compression specific work reduction, and thus in higher electric efficiency
- the outlet temperature from the compressor would be reduced as well, and consequently the inlet temperature in the solar field. This would lower the average temperature in the field, and improve its thermal efficiency

A feasible way to attain the temperature reduction would be to change the heat rejection system, and switch to a air-water hybrid system.

Future works might also consider the employment of solar tower instead of linear collectors, more suitable for high temperature applications in virtue of their compactness, which allows for high thermal fluxes on limited surfaces, greatly reducing heat losses. This way, both an improvement of the power block efficiency by means of a T_{\max} increase, and a higher solar field efficiency could be attained, with major positive effects on the overall conversion efficiency.

An economical analysis, in order to assess the final cost of energy and thus the economic benefit deriving from the adoption of a gas cycle, would also be recommended for future work. In that perspective, the impact of a storage system on the performance of the plant, which was not considered in this work, could be integrated, having a general positive effect on the performance of the plant and the final cost of energy.

With the listed additions, a comparison between traditional technology and direct systems with an improved performance could be carried out moneywise, attaining a better evaluation of the advantages that the adoption of supercritical CO₂ Brayton cycles in CSP plants could guarantee.

8 REFERENCES

[1] Intercontinental Panel on Climate Change (IPCC), *Fifth Assessment Report*, Cambridge University Press, 2013

[2] United States Environmental Protection Agency, EPA website, <http://www.epa.gov/>

[3] W. Stine, M. Geyer, *Power from the Sun*, John Wiley and Sons, Inc., 1986

[4] J. Houghton, *The Physics of the atmosphere*, CUP Archive, 1977

[5] <http://www.desertec.org/>

[6] <http://www.torresolenergy.com/>

[7] <http://solargis.info/doc/free-solar-radiation-maps-DNI>

[8]

http://www.abengoasolar.com/web/en/nuestras_plantas/plantas_en_construccion/estados_unidos/

[9] Fraunhofer Institute for Solar Energy Systems, *Levelized Cost of Electricity: Renewable Energy Technologies*, November 2013

[10] <http://www.nrel.gov/docs/fy13osti/56731.pdf>

[11] <http://www.reuk.co.uk/>

[12] F. Kreith, D. Goswami, *Handbook of Energy Efficiency and Renewable Energy*, CRC Press, 2007

[13] <http://www.theenergylibrary.com/node/460>.

[14] <http://www.novatecsolar.com/56-1-PE-2.html>

[15] <http://ivanpahsolar.com/about>

[16] C. Turci, *Supercritical CO₂ for Application in Concentrating Solar Power Systems*, NREL, 2009

- [17] K. Stern, *High temperature properties and decomposition of inorganic salts*, NSRDS, 1969
- [18] L. Ge, L. Moretti, F. Pettit, P. Singh, *Corrosion of Chromia and Alumina Forming Iron Alloys in Molten Na-K Nitrate Salt at 550 and 650C*, MRS Fall Meeting&Exhibit, 2013
- [19] D. Kruger et al., *Experiences with DSG at the Kanchanaburi Solar Thermal Power Plant*, SolarPACES 2012, 11.-14- Sept. 2012, Marrakesch, Marokko
- [20] A. Rovira et al., *Optimization of Brayton cycle for low to moderate grade thermal energy sources*, Energy, 2013
- [21] G. Angelino, *Real gas effects in carbon dioxide cycles*, ASME, 1969
- [22] E. Feherer, *The supercritical thermodynamic power cycle*, Energy Conversion vol.8, pp 85-90, 1968
- [23] R. Forristal, *Heat Transfer Analysis and Modeling of a Parabolic Trough Solar Receiver implemented in Engineering Equation Solver*, NREL, 2003
- [24]] F. Kreith, D. Goswami, *Energy Conversion*, CRC Press, 2008
- [25] http://www.archimedesolarenergy.com/it_prodotti.htm
- [26] J. Muñoz et al., *The New Technology of Gas Cooled Trough Collectors*, SolarPaces 2011
- [27] M. Binotti et al., *An analytical approach treating three-dimensional geometrical effects of parabolic trough collectors*, NREL, 2012
- [28] K. Riffelmann, *Performance enhancement of parabolic trough collectors by solar flux measurement in the focal region*, Solar Energy, 2006
- [29] A. Robbiati, *Sviluppo di un codice di calcolo per l'ottimizzazione di un impianto solare termodinamico con fluido termovettore gassoso*, Master Thesis, Politecnico di Milano, 2013
- [30] L. Coco, J. Muñoz, J. Martinez-Val, *Innovations on direct steam generation in linear Fresnel collectors*, SolarPACES, 2013

- [31] S. Lambrughi, A. Serafino, *Utilizzo dell'anidride carbonica in sistemi solari a concentrazione lineare*, Master Thesis, Politecnico di Milano, 2011
- [32] E. Macchi, A. Perdichizzi, *Efficiency prediction for axial flow turbines operating with non conventional fluids*, ASME, 1977
- [33] H. Craig, H. Cox, *Performance estimation of axial flow turbines*, SAGE, 1970
- [34] Ainley, DC, and Mathieson, *A Method of Performance Estimation for Axial-Flow Turbines*, British Aeronautical Research Council, R&M2974, 1951
- [35] <http://www.barber-nichols.com/>
- [36] A. Stevens et al., *Operation and Analysis of a supercritical CO₂ Brayton Cycle*, SANDIA, 2010
- [37] W. Jiang, J. Khan, R. Dougal, *Dynamic centrifugal compressor model for system simulation*, Journal of Power Sources, 2006
- [38] D. Japkise, *Centrifugal compressor design and performance*, Concepts ETI Inc., 1996
- [39] J. Dyreby et al., *Modeling off design and part load performance of supercritical carbon dioxide power cycles*, ASME Turbo Expo, 2013
- [40] www.industrial-solar.de
- [41] newenergydirection.com
- [42] http://rredc.nrel.gov/solar/old_data/nsrdb/1991-2005/tmy3/
- [43] www.esrl.noaa.gov
- [44] M. J. Montes Pita, *Analisis y Propuestas de sistemas solares de alta exergia que emplean agua como fluido calorifero*, Universidad Politecnica de Madrid, Master Thesis
- [45] A. Giostri, M. Binotti et al., *Comparison of two linear collectors in solar thermal plants: parabolic trough VS Fresnel*, ASME 5th International Conference on Energy Sustainability, 2011

- [46] J.E. Cha et al, *Development of a Supercritical CO₂ Brayton Energy Conversion System coupled with a Sodium Cooled fast reactor*, Nuclear Engineering and Technology, 2009
- [47] B. Kelly, D. Kearney, *Parabolic Trough Solar System Piping Model*, NREL, 2004
- [48] UNI EN 10216, part 2
- [49] F. P. Incropera, *Fundamentals of Heat and Mass Transfer 7th edition*, John Wiley & Sons, 2007
- [50] <http://yearbook.enerdata.net/#energy-consumption-data.html>